Thermodynamics-based Design of Wide Band Gap Semiconductor Catalysts

Doctoral Thesis

for

The Award of The Doctoral Degree

of The Faculty of Mathematics and Natural Sciences

of the University of Cologne

Submitted by

Seulgi Ji

Incheon, Republic of Korea

Accepted in 2025

Acknowledgements

First of all, I believe this thesis could not have been written without the support and help of many people. Looking back on my PhD journey, my heart is filled with gratitude. There are so many people I want to thank, and I truly appreciate all of your encouragement and support.

I would like to express my sincere gratitude to **Prof. Dr. Dr. (*h.c.*) Sanjay Mathur** for his kind support. Thank you for giving me the opportunity to pursue my PhD in Cologne and for supporting me to continue my research in his group. I cannot imagine what my time in Cologne would have been without the guidance and encouragement I have received from you. I specially thank you for encouraging me to do experiments to verify my theoretical studies.

I am deeply grateful to **Prof. Dr. Heechae Choi** for always believing in me and guiding me to apply thermodynamics theory to various research projects and many problems solving. Before coming to Germany, I could not have imagined myself reading physical chemistry books and doing research like this. Thank you for encouraging me not to give up whenever I faced difficulties.

I would also like to thank **Prof. Dr. Klas Lindfors** for kindly serving as my second examiner, and **Prof. Dr. Elmar Behrmann** for taking the role of my chair. My sincere thanks also go to **Dr. Thomas Fischer** for being the minutes taker of my defense.

My heartfelt thanks to **Prof. Dr. Min Kim**, who has always supported me from Korea. Knowing that I had a professor back home who believed in me gave me great strength.

I am also very grateful to my collaborators for the CeO_2 paper, especially, **Dr. Sung Beom Cho, Dr. Hyunseok Ko, and Dong Won Jeon**. I would also like to thank **Dr. Minyeong Je**, who helped me a lot when I first started DFT calculations by sharing skills, knowledge, and valuable tips. I am truly grateful for your support.

I would especially like to thank **Dr. Niusha Heshmati** and **Sumiya Iqbal**, my "yo girls," for always comforting me whenever I was too negative and for reminding me that only good things will come. I will miss you so much, and I am very happy that we survived! I am also thankful to **Dr. Andreas Lichtenberg** and **Dr. Chijioke Kingsley Amadi**, my dear friends—I will miss our lunch breaks, coffees, and especially the frozen cappuccinos.

I would also like to thank the *Thurstea* group: **Nurgül Tosun, Jessica Kirchhartz, Dirk Pullem,** and **Billy Fauzi**. Special thanks to Jessica for always bringing various nice teas—our weekly tea times were one of the happiest moments of my week.

And many thanks to **Naina Goyal**, **Simon Diel, Jessica Kirchhartz, Dr. Andreas Lichtenberg, Tom Jonas Schneider** and **Billy Fauzi** for their assistance with my TiO_2 work in performing PEC measurement, XRD analysis, and SEM characterization. My gratitude also goes to **Riya Sharma**.

Of course, I am grateful to all other members of the group for making me feel a sense of belonging, **Dr. Touraj Karimpour, Dr. Shaista Ilyas, Dr. Anja Sutorius, Dr. Veronika Brune, Benedict Witulski, Ziyaad Aytuna, David Patrun, René Weißing, Ruth Adam, Moritz Steiner, Hyeonkwon Lee, Lukas Rryci, Angelika Freulein,** and **Kelly Brinkmann.**

As well as all my friends, especially **Soomin Han**, my closest and best friend, who has been like a sister to me. Without her, my time in Germany would have been much harder. (And **Sébastien Clemen**! Thank you so much for encouraging me to come to Germany to study Chemistry!) **Eunsaem Cho**, **Sung Beom Jo,** thank you for always treating me whenever I visited Korea and for sincerely wishing me the best. **Dr. Aude Geistodt-Kiener**, **Mara Moon, Yizhou Liu, Dr. Yongdeok Kwon, Woojin Kim, Kyunghye Park, Jaewon Kwak, Junseok Yang, David Dmonte,** and **Otgonbayer Erdene-Ochir** I am grateful for the laughter and for giving me moments to rest my mind while living abroad.

I would like to express my deepest gratitude to my family. I know that many of them have already supported me, especially thankful to my grandpa, **Oksoo Choi,** my aunts, **Hyeseung Ji, Okhee Ji, Insuk Choi,** my uncle, **Hunkoo Choi,** my cousins, **Yoonmi Jeong, Aery Choi, Jinhyeok Lee, Yury Choi, Isla**, and **Ayn** for their encouragement throughout this journey.

Last but not least, to my beloved parents, Doyoung Ji and Mikyong Choi, I dedicate this thesis to my parents, who have always supported me quietly from afar. Without their love and encouragement, I could not have come this far. I do not know how I could ever repay their endless devotion. I love you, and I am deeply grateful! 사랑하는 엄마 아빠, 진심으로 감사합니다!

Abstract

Thermodynamics is capable of giving accurate predictions of phase stabilities of materials and rate-determining steps in chemical reactions. Numerous studies based on thermodynamic principles, especially when combined with computational methods, have made significant contributions to materials development. In particular, the currently adopted thermodynamics-based theoretical models have successfully elucidated surface chemical reactions and catalytic phenomena on metallic materials. However, as modern energy conversion technologies involve electrochemical and photochemical reactions of complicated nanostructured materials, conventional *ab initio* thermodynamics approach showed unreliable predictions and low feasibilities originating from the limitations of conventional atomic scale modeling and first principles calculation methods.

In this regard, my PhD research has focused on advancing a theoretical model for enhanced understanding of surface reaction mechanisms in semiconductors and complex materials by combining quantum mechanics *ab initio* calculations and Fermi-Dirac statistics and by considering vibrational entropy terms for certain catalytic reactions having a narrow temperature window. With the consideration of the electron chemical potential (Fermi level) in the computation of adsorption energies for catalytic reaction intermediates on wide band gap semiconductor surfaces, catalytic phenomena in (complex) nanomaterials could be well explained with much improved accuracy and precision.

This work presents how the new theoretical model can advance the understanding of catalytic and photoelectrochemical reactions in wide band gap semiconductors with complex nanostructures using two model systems: cerium dioxide (CeO_2) for the complex reaction of methane oxidation, and titanium dioxide (TiO_2) for the widely studied reaction of photocatalytic water splitting. To verify the reliability of the theoretical model, experimental studies were performed for water oxidation on TiO_2 photoanodes. TiO_2 thin films with varied grain sizes were prepared by the chemical vapor deposition (CVD) of $[Ti(O^iPr)_4]$ precursors under kinetic control, leading to distinct photoelectrochemical catalytic activities.

By considering both surface reaction kinetics and the hole transport efficiency in adsorption energy calculations, this study demonstrates the applicability of theoretical model in bridging theoretical predictions with experimental PEC results. Overall, this work expands the new theoretical framework from electrochemical catalysis to photoelectrochemical catalysis, providing new insights and theoretical strategies for rationally designing the semiconductor catalysts.

List of Contents

Chapter 1

Introduction

1.1 Catalysis

Catalysts are vital for modern chemistry and technology, playing a crucial role in various industrial fields. Particularly, catalysts have greatly improved reaction efficiency and led to technological advancements in the production of commodity chemicals, pharmaceuticals, and consumer goods.[1] Representative examples include the Haber-Bosch process employing Fe-based catalysts for ammonia synthesis in agriculture,[2] zeolite catalysts for fluid catalytic cracking in the petrochemical industry.[3] Also, in pharmaceutical synthesis, Pd-catalyzed cross-coupling reactions.[4] Electrocatalysts for water electrolysis and CO_2 reduction, which underpin emerging technologies such as green hydrogen production and carbon-neutral fuels.[5] Accordingly, the industrial catalyst market is also growing rapidly as the demand for efficient, sustainable, and cost-effective catalysts increases. In addition, catalysts significantly contribute to addressing environmental issues by converting harmful greenhouse gases such as CO_2 and CH_4 into less harmful or more useful products.

The term "Catalysis", derived from the Greek word, καταλυση – meaning "dissolution" and "loosening" – was coined by a Swedish chemist, Jöns Jakob Berzelius, in 1835.[6] He described catalysis as a new force inducing chemical reactions in both inorganic and organic substances, which is different in nature from conventional chemical affinity. This force acts to facilitate the reaction without themselves participating as a component of the reactants. After a few decades, the German chemist Wilhelm Ostwald defined "the kinetic definition of catalysis", describing "catalysis is the process of accelerating of a slow-running chemical reaction by a foreign material without consuming the catalysts.".[7] Today, the International Union of Pure and Applied Chemistry (IUPAC) defines a catalyst as "a substance that participates in a particular chemical reaction and thereby increases its rate but without a net change in its quantity in the system after the reaction.".[8]

Catalysts increase the rate of a chemical reaction by altering the energy landscape of the reaction. This phenomenon can be quantitatively described by the Arrhenius equation. The Arrhenius equation shows how the reaction rate constant (k) change depending on the activation energy and temperature, which is given by,[9,10]

$$k = A \exp(-\frac{E_a}{RT}) \tag{1.1}$$

where A, R, and T in Eq (1.1) are the pre-exponential factor, the gas constant, and T is the absolute temperature, respectively. E_a in Eq (1.1) represents the activation energy, the minimum energy that reactants must overcome for the reaction to occur. In Figure 1.1, there are two reaction pathways: one without a catalyst and one with a catalyst, where the corresponding activation energies are denoted as E_{a_1} for the uncatalyzed reaction and E_{a_2} for the catalyzed reaction. Catalysts increase the reaction rate and therefore promote the reactivity by providing an alternative reaction pathway with a lower activation energy ($E_{a_1} > E_{a_2}$).

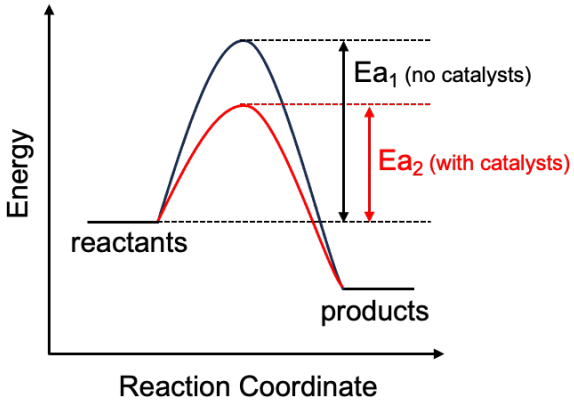

Figure 1.1 A schematic energy diagram of a chemical reaction with and without a catalyst, illustrating the role of catalysis in lowering the activation energy (E_a).[9]

According to the physical nature, catalysis is classified into three categories:[11]

(1) Homogeneous catalysis: Catalysts are in the same phase as the reactants (typically, the liquid phase). Due to strong interactions between the catalysts and reactants, homogeneous catalysts exhibit high reactivity and selectivity even under mild reaction conditions. However, the separation of the catalysts from the products is difficult, costly, and energy-consuming, complicating their recovery and reuse. Transition-metal complexes such as Wilkinson's catalyst ($RhCl(PPh_3)_3$) for alkene hydrogenation,[12] and asymmetric organocatalysts, such as the proline-catalyzed reactions awarded the Nobel Prize in Chemistry in 2021, are the representative examples.[13]

(2) Heterogeneous catalysis: Catalysts are in a different phase from the reactants, typically a catalyst is in a solid phase, and reactants are in liquid or gaseous phases. Accordingly, catalysts are relatively easy to separate from the product mixture, leading to improved purity

and cost-effectiveness.[14] Heterogeneous catalysts are often used under harsh reaction conditions, such as high temperatures and pressures, which are common in bulk chemical production. However, heterogeneous catalysts have lower selectivity and are less beneficial in terms of reaction rate compared to homogeneous catalysts because the reactants must be diffused, adsorbed, and desorbed on the surface. Based on the chemical components, heterogeneous catalysts are categorized into three types: metal catalysts, metal oxide catalysts, and zeolites. A well-known example is nickel, which is widely used for hydrogen production via steam reforming.[15]

(3) Biocatalysis: Biocatalysis utilizes biological molecules, predominantly enzymes, to promote chemical transformations. These catalysts exhibit high selectivity and operate efficiently under relatively mild reaction conditions, making them environmentally friendly.[16] Beyond their natural role in metabolism, enzymes are widely employed in industry, ranging from pharmaceuticals to detergents, food processing, and biofuel production. However, enzymes often suffer from limited stability outside their natural environments and require high production costs. Recent advances in protein engineering, directed evolution, and enzyme immobilization have significantly improved their stability and broadened their applicability. Representative examples of enzymatic reactions are lipase-catalyzed esterification[17] and alcohol dehydrogenase-mediated asymmetric reduction of ketones.[18]

Among them, heterogeneous catalysis is the most widely used in industrial fields due to the following advantages:[19]

i) The ease of catalyst separation is advantageous for repeated use and continuous process application
ii) High durability and stability under high temperature and high-pressure conditions
iii) The catalytic selectivity and activity can be improved by controlling the catalyst structure
iv) The reaction mechanisms on solid surfaces are actively studied, supported by both experimental and theoretical investigations.

Therefore, this thesis will focus on an integrated theory-experiment approach in heterogeneous catalysis.

1.2 Scientific Background and Motivations

In heterogeneous catalysis, metal catalysts, especially noble metals, were the most widely used catalysts due to their high activity and selectivity. For example, Humphry Davy observed in the early 1800s that platinum and palladium increased the combustibility of a gaseous mixture of coal gas (mainly CH_4, H_2, and CO) and air.[20] In the Haber-Bosch process, a promoted iron catalyst, obtained by reducing iron oxides, was successfully used to synthesize ammonia, making the first large-scale industrial success.[2] The overall reaction can be represented as follows:

$$N_2\,(g) + 3H_2\,(g) \rightleftarrows 2NH_3\,(g)$$

The catalyst contained structural promoters, such as calcium oxide (CaO), to improve stability, and electronic promoters, including potassium oxide (K_2O) and aluminium oxide (Al_2O_3), to enhance nitrogen activation and prevent sintering, thereby maintaining a high surface area of iron. Additionally, cobalt-based catalysts are utilized to convert a mixture of carbon monoxide and hydrogen into liquid hydrocarbons through the Fischer-Tropsch process.[21] This process can be written by the following reaction:

$$(2n+1)\,H_2 + n\,CO \rightarrow C_nH_{(2n+2)} + n\,H_2O$$

However, noble metal catalysts have limitations in industrial use due to their scarcity and high cost.[22] Transition metals are abundant and inexpensive, but they exhibit lower selectivity and activity, and are vulnerable to oxidation and corrosion. To overcome the limitations of metal catalysts, transition metal oxides such as titanium dioxide (TiO_2),[23,24] tin dioxide (SnO_2),[25] and iron oxides (Fe_2O_3)[26] have emerged as alternative catalysts.

Metal oxide-based catalysts have distinct advantages over metal catalysts.[27] Metal oxides have excellent redox properties, and the oxidation states of the metal center can be relatively easily controlled. Secondly, metal oxides exhibit various crystal structures, morphologies, and surface facets due to their inherent structural flexibility. Thirdly, their electronic structures can be readily modified by the introduction of structural defects such as oxygen vacancies to improve the surface reactivity. Lastly, metal oxides band gaps can be tuned allowing them to be highly active in light-driven and electrochemical reactions. Due to these properties, metal oxides are being actively studied in various applications such as photoelectrochemistry, energy conversion, and environmental catalysts.[28]

However, in recent years, it has become evident that single-component catalysts alone are often insufficient to effectively control complex reaction pathways or to simultaneously achieve the high selectivity and reactivity required for sustainable energy conversion. As environmental problems have become increasingly severe, new chemical reactions such as carbon dioxide reduction reaction (CO_2RR) and nitrogen reduction reaction (NRR) have gained significant attention to produce sustainable energies with less greenhouse gas emission.[29] These reactions proceed through multiple reaction steps involving various intermediates, and therefore controlling catalytic selectivity is crucial for directing a specific reaction pathway.

In addition, due to the depletion of natural resources, there is an urgent need for alternative materials to replace traditional materials such as precious metals with earth-abundant materials. Consequently, the development of heterogeneous catalysts with high efficiency, reactivity, and selectivity is driven by the increasing demand for reducing greenhouse gases, efficient energy conversion, and cost-effective process intensification. Accordingly, recent research increasingly focuses on heterojunction structures combining different materials such as metals, metal oxides, or bimetallic/alloy-based catalyst designs to enhance the catalytic activity. These multicomponent catalysts can address the drawbacks of single-phase catalysts and exhibit improved performance even under complex reaction conditions.

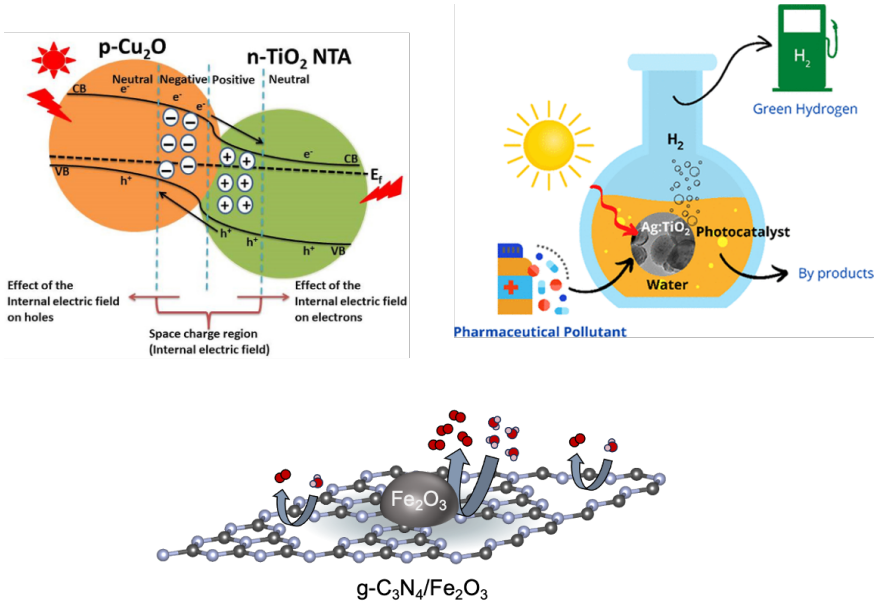

Figure 1.2 Examples of heterojunction structure catalysts: a p-n heterojunction photoanode of Cu_2O on TiO_2, Ag-deposited TiO_2 photocatalyst, Fe_2O_3-deposited g-C_3N_4 photocatalyst.[30–32]

For example, Aguirre et al. reported that the efficiency of CO_2 reduction on the p-type semiconductor Cu_2O can be improved by forming a p-n heterojunction with the n-type

semiconductor TiO_2, thereby suppressing photocorrosion.[30] Similarly, Ag-deposited TiO_2 has been reported to exhibit enhanced photocatalytic activity.[31] In another example, combining g-C_3N_4 with Fe_2O_3 improved hole carrier transport by Fermi level pinning.[32]

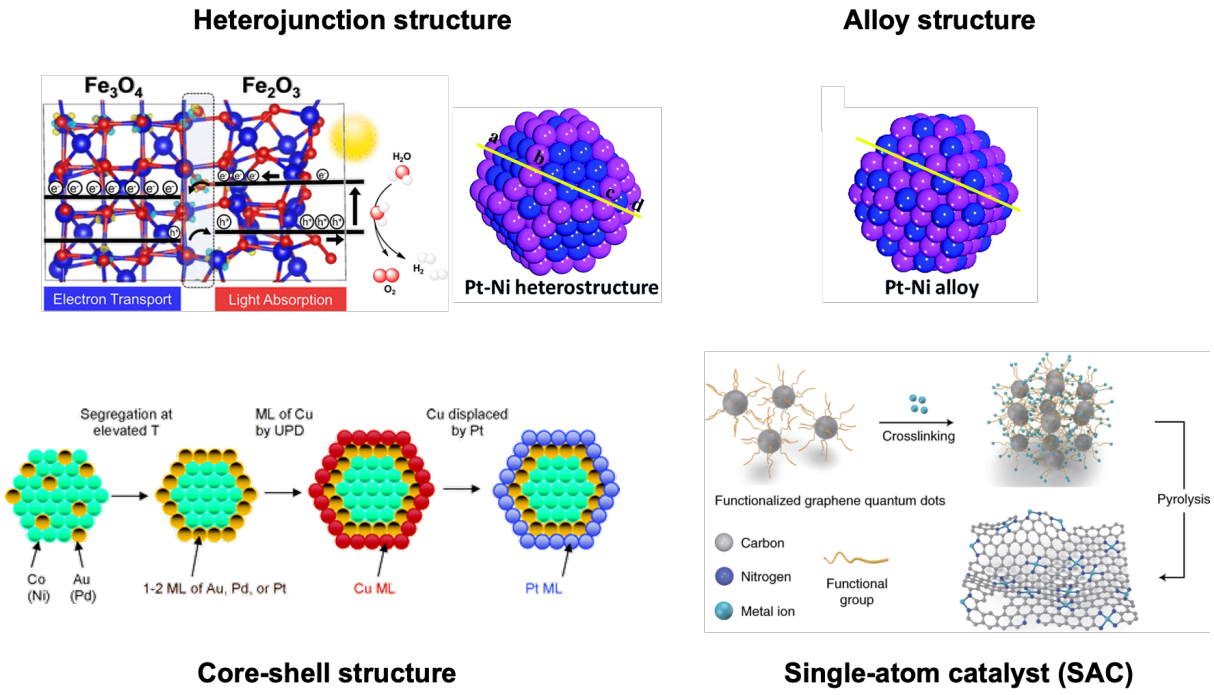

Figure 1.3 Examples of heterogeneous catalysts: heterojunction structures, alloy structure, core-shell structure, and single-atom catalyst, respectively.[33–36]

Heterogeneous catalysts can be classified into several types based on the structural design. Representative examples include heterojunction catalysts, core-shell structure catalysts, alloy catalysts, and single-atom catalysts.

- A heterojunction structure refers to an interface formed between two or more materials with different electronic properties, where a built-in electric field is formed due to their band alignment.[37–39] They exhibit unique electronic properties and charge transfer mechanisms, thereby suppressing charge recombination by charge separation and transfer mechanisms, which is especially beneficial for photocatalytic reactions.[37]
- An alloy structure is a homogeneous mixture of two or more metal elements at the atomic scale. It is effective in controlling catalytic activity and selectivity in heterogeneous catalysis because the electronic structure and geometric structure can be precisely modified.[40]
- A core-shell structure consists of catalytically active nanoparticles of a core material encapsulated by an outer shell of a different material. This structure serves to protect the

core nanoparticles from problems such as sintering, corrosion, or poisoning, therefore improving catalyst stability and durability.[41]

- A single-atom catalyst (SAC) consists of isolated metal atoms dispersed on a solid support, typically stabilized by coordination with surface atoms such as oxygen, nitrogen, or carbon. SACs can maximize the metal utilization and control the local coordination environment of single-atom metal centers; therefore, it is beneficial for developing efficient and low-cost heterogeneous catalysts.[42]

However, with the increasing structural complexity of multicomponent structures and interface designs, understanding catalytic phenomena using only the classical theories becomes more challenging. Thus, more sophisticated and advanced strategies of catalyst design are highly required for the precise interpretation and prediction of reaction mechanisms.

1.3 Scientific Objectives

The Gibbs free energy, which represents the maximum non-expansion work at constant pressure and temperature, serves as a fundamental thermodynamic parameter for evaluating energy changes and the spontaneity of chemical reactions. Particularly, when combined with parameters derived from density functional theory (DFT) calculations, it gains enhanced predictive power in understanding surface reactions.

Since the introduction of the Computational hydrogen electrode (CHE) framework by Nørskov et al.,[43] the theoretical understanding of electrochemical catalytic mechanisms on metal catalysts has seen significant advancements. The CHE approach provides a conceptual link between DFT-calculated adsorption energies and experimentally measurable electrode potentials by referencing all reactions to the equilibrium $H^+ + e^- \rightleftarrows H_2$, thereby circumventing the explicit treatment of solvated protons and electrons.

However, catalytic phenomena in wide band gap semiconductors cannot be fully captured within the widely adopted CHE framework, as the method underestimates or overlooks the fact that the Fermi level of semiconductors can be easily changed by various factors such as adsorption, oxygen vacancy formation, and doping.[38] These alterations, in turn, affect the adsorption energy and thereby the overall catalytic activity. In addition, with the growing demand for advanced catalysts for various applications such as photocatalysis and fuel cells, where complicated reaction mechanisms are involved, a more comprehensive understanding of catalytic phenomena is required for the rational design of high-performance catalysts.

A theoretical model, “Fermi level dependent adsorption energy theory” was developed by modifying the current standard CHE approach and incorporating the Fermi-Dirac statistics to more precisely consider the intrinsic properties of wide band semiconductors for understanding surface reaction mechanisms (Choi et al.). The applicability of this theoretical model has been validated by the elucidation of surface reaction mechanisms of simple systems such as oxygen evolution reaction (OER) on TiO_2.[44]

The present work aims to overcome the limitations of the current theoretical model that cannot fully explain the catalytic phenomena on semiconductor catalysts and suggest a new model for thermodynamics-based framework for catalysts design. To verify the hypothesis, literature data are compared with the theoretical predictions for electrochemical reactions, and the model will further be extended to photocatalytic reactions. Experimental verification is also performed to examine its applicability, providing a pathway for the rational design of catalysts with even more complex structures to enhance their performance in the future.

Chapter 2

Theoretical Background

2.1 Classical Approach

2.1.1 Adsorption Energy: A Determining Parameter in Chemical Reactions

In catalysis, adsorption strength between analyte and the substrates is one of the key factors in determining the catalytic activity. In 1911, Paul Sabatier highlighted the important role of optimal adsorption strength in determining catalytic activity, a concept known as the Sabatier principle.[45] It states that the interactions between the catalyst and the adsorbates in heterogeneous catalysis should be neither too strong nor too weak, but rather "appropriate", providing a basic qualitative concept of optimum adsorption strength for the catalytic activity.[46] Since then, "The Langmuir isotherm" model was proposed by Irvin Langmuir to describe the adsorption of molecules on a solid surface in 1918.[47,48] This model assumes monolayer adsorption and explains the adsorption of gas or liquid molecules onto specific active sites of a solid surface. The significance of this adsorption in catalytic processes arises because catalytic reactions occur on the solid surface. Building on this, the Langmuir isotherm provides a quantitative framework to understand the relationship, as the amount of adsorbed molecules directly impacts catalytic activity. In heterogeneous catalysis, for example, the Langmuir isotherm helps explain how well reactant gases adsorb on the catalytic surface and how these adsorbed molecules subsequently react to form products.

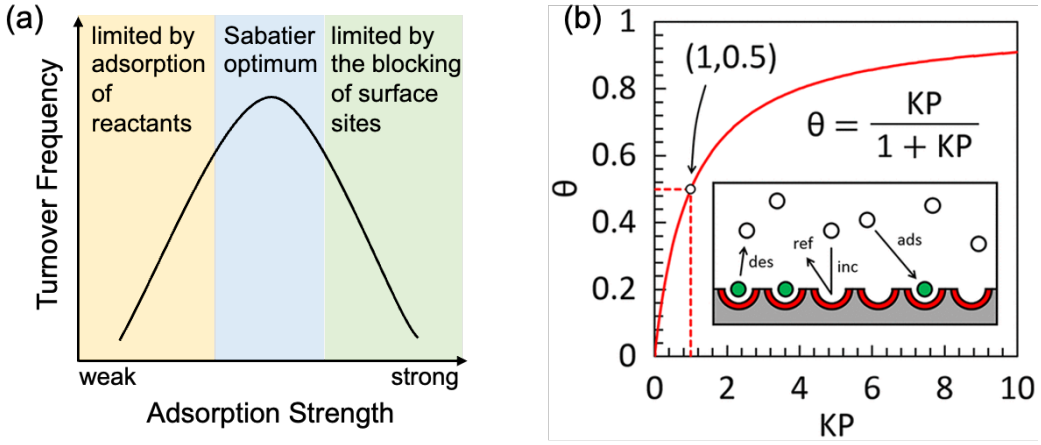

Figure 2.1 Schematic illustration of the Sabatier principle and Langmuir isotherm model.[48]

2.1.2 Rationale of Using Thermodynamics in Catalyst Design

This part has been prepared with reference to Chapters 2, 3, 17, and 18 of the textbook, P. Atkins, J. De Paula and J. Keeler, *Atkins' Physical Chemistry*, Oxford University Press, 11th edition, 2017.[9]

2.1.2.1 The Spontaneity of the Reaction: Thermodynamics

The Second Law of Thermodynamics

The Clausius inequality – a direct expression of the Second Law of Thermodynamics – is of great importance in describing the spontaneity of chemical reactions:

$$\oint \frac{\delta q}{T} \leq 0 \tag{2.1}$$

where $\oint$ denotes the cyclic (closed path) integral, δq is the infinitesimal amount of heat transferred into the system (an inexact differential, path dependent), and T is the absolute temperature of the heat reservoir at the boundary where the exchange occurs.

From this, a state function, entropy S, is defined for a reversible process as:

$$dS = \frac{\delta q_{rev}}{T} \tag{2.2}$$

where dS represents the infinitesimal change in entropy (an exact differential, state function), and δq_{rev} is the reversible heat exchanged with the reservoir at temperature T.

When a change occurs in the system and energy is transferred as heat between the system and the surroundings, the Clausius inequality is expressed as:

$$dS \geq \frac{\delta q}{T} \tag{2.3}$$

If the system is isolated from its surroundings (i.e., no heat exchange, $\delta q = 0$), this implies that:

$$dS \geq 0 \tag{2.4}$$

This statement leads to **the Second Law of Thermodynamics**:

"In an isolated system, the entropy cannot decrease during a spontaneous change."

In terms of the system and its surroundings, the Second Law can be more generally expressed as:

$$\Delta S_{tot} = \Delta S + \Delta S_{sur} \geq 0 \tag{2.5}$$

where ΔS_{tot} is the total entropy change, ΔS is the entropy change of the system, and ΔS_{sur} is the entropy change of the surroundings.

Clausius Inequality at Constant Pressure: The Definition of Gibbs Free Energy

When energy is transferred as heat at constant pressure and only expansion work is involved, the heat exchanged equals the infinitesimal change in enthalpy (dH):

$$\delta q_p = dH \tag{2.6}$$

Therefore, the Clausius inequality at constant pressure can be written as:

$$TdS \geq dH \tag{2.7}$$

The criterion of spontaneity at constant pressure can be more conveniently expressed using the Gibbs free energy (G) defined as:

$$G = H - TS \tag{2.8}$$

The differential of G (dG) under isothermal conditions ($dT = 0$) is:

$$dG = dH - TdS \tag{2.9}$$

Since $TdS \geq dH$, any spontaneous change at constant pressure and temperature satisfies:

$$dG \leq 0 \tag{2.10}$$

Under isothermal and isobaric conditions ($\Delta T = 0,\ \Delta P = 0$), the finite Gibbs free energy change (ΔG) is written as:

$$\Delta G = \Delta H - T\Delta S = (\Delta U + P\Delta V) - T\Delta S \tag{2.11}$$

where ΔU is the change in internal energy of the system.

For condensed systems, the volume change (ΔV) is negligible; therefore, the Gibbs free energy change (ΔG) is given by:

$$\Delta G = \Delta U - T\Delta S \tag{2.12}$$

The Maximum Non-Expansion Work

Since enthalpy is defined as $H = U + PV$, the Gibbs free energy can also be written in terms of internal energy (U) as:

$$G = H - TS = U + PV - TS \tag{2.13}$$

Taking the total differential of G (dG) at constant pressure and temperature ($dP = 0,\ dT = 0$), dG is defined as:

$$dG = dU + PdV - TdS \tag{2.14}$$

According to the first law of thermodynamics, the change in the internal energy (dU) equals the sum of the heat exchanges (δq) and the work done (δw):

$$dU = \delta q + \delta w = \delta q - P_{ext}dV + \delta w_{non-exp} \tag{2.15}$$

where $-P_{ext}dV$ is the mechanical work of expansion against the external pressure (P_{ext}) and $\delta w_{non-exp}$ is the non-expansion work, including contributions such as electrical work in an electrochemical cell. Substituting this expression for the change in the internal energy (dU) into the change in Gibbs free energy (dG) gives:

$$dG = \left(\delta q - P_{ext}dV + \delta w_{non-exp}\right) + PdV - TdS \tag{2.16}$$

For a reversible process at mechanical equilibrium, the heat exchange is given by $dq = TdS$, and the external pressure equals the system pressure ($P_{ext} = P$). Under these conditions:

$$dG = \delta w_{non-exp} \tag{2.17}$$

which means that, at constant pressure and temperature, the non-expansion work corresponds to the maximum value, defined as:

$$dG = \delta W_{non-exp}^{max} \tag{2.18}$$

In this framework, a negative differential Gibbs free energy (dG) indicates that the process occurs spontaneously, with $|dG|$ representing the maximum non-expansion work that a system can perform. Therefore, the Gibbs free energy serves as a fundamental thermodynamic criterion for determining the spontaneity of chemical reactions.

2.1.2.2 The Rate of Reactions: Kinetics

Although thermodynamics shows whether a reaction is energetically favorable, the reaction will not proceed unless its rate is sufficient. Transition state theory provides a theoretical framework to quantitatively estimate the reaction rate based on the free energy of activation. In transition state theory, a reaction pathway is considered a sequence of reaction steps, where a reaction proceeds through a transition state, forming an activated complex known as transition state in a quasi-equilibrium state.

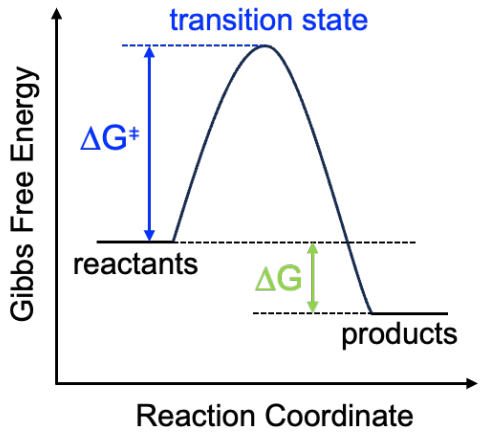

Figure 2.2 A schematic illustration of a free energy diagram, showing the Gibbs free energy barrier between the reactants and the transition state ($\Delta G^{\ddagger}$) and the Gibbs free energy difference between products and reactants (ΔG).

Figure 2.2 illustrates that a Gibbs free energy barrier exists between the reactants and the transition state, with its maximum corresponding to the Gibbs free energy of activation ($\Delta G^{\ddagger}$). The overall free-energy change of the reaction (ΔG) is given by the difference in the Gibbs free energy between products and reactants, determining the thermodynamic favorability of the reaction.

According to transition state theory, the rate constant k depends on the activation free energy at a given temperature T, which is given by:

$$k = \frac{k_B T}{h} e^{-\Delta G^{\ddagger}/RT} \tag{2.19}$$

where k_B, h, and R are the Boltzmann constant, Planck's constant, and the gas constant, respectively. The activation Gibbs free energy can be decomposed into enthalpic and entropic contributions as:

$$\Delta G^{\ddagger} = \Delta H^{\ddagger} - T\Delta S^{\ddagger} \tag{2.20}$$

where $\Delta H^{\ddagger}$ is and $\Delta S^{\ddagger}$ are the enthalpy and the entropy of activation, respectively. Then, the rate constant can be expressed by the Eyring Equation, which describes the relationship between reaction rate and temperature, as follows:

$$k = \frac{k_B T}{h} e^{\Delta S^{\ddagger}/R} e^{-\Delta H^{\ddagger}/RT} \tag{2.21}$$

This expression resembles the empirical Arrhenius equation, which is given by:

$$k = A e^{-E_a/RT} \tag{2.22}$$

where A is the pre-exponential factor, representing the effective frequency of molecular collision, and E_a is the activation energy. Accordingly, the pre-exponential factor A in the Arrhenius equation corresponds to $\frac{k_B T}{h} e^{\Delta S^{\ddagger}/R}$, and the activation energy E_a is associated with the enthalpic contribution $\Delta H^{\ddagger}$. Transition state theory therefore provides a molecular-level thermodynamic interpretation of the empirical parameters of the Arrhenius equation by linking entropy and enthalpy changes to reaction kinetics. Importantly, thermodynamics determines whether a reaction is favorable ($\Delta G < 0$), whereas kinetics dictates how fast the reaction proceeds. For instance, catalysts accelerate reactions by lowering the activation free energy barrier without altering the overall free-energy change.

2.1.2.3 Marcus Theory

Conventionally, thermodynamics, that determines the spontaneity of chemical reactions, and kinetics, that determines the reaction rate, have been independently treated. However, one may ask: does the reactivity of chemical reactions solely depend on kinetics, or do thermodynamics also control the reactivity? Marcus theory offers a comprehensive framework to evaluate the chemical reaction involving electron transfer by incorporating both kinetic and thermodynamic considerations.[9,49] The fundamental concept of Marcus theory is based on Franck-Condon principle, in which nuclei cannot shift position while electrons can transition between donor and acceptor states rapidly because electrons are much lighter than nuclei.[50,51] In this regard, Rudolph Marcus focused on how electron transfer can affect the reactivity of chemical reactions.

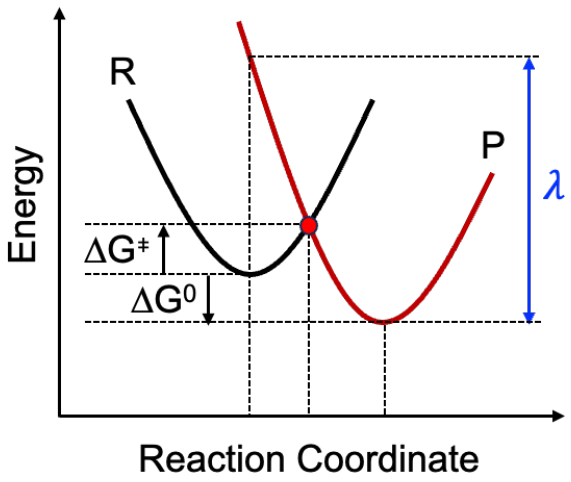

Figure 2.3 Marcus theory model for the outer sphere electron transfer reactions. The parabolic curves represent the potential energy surfaces of the reactants (R, black) and product (P, red) states. ΔG^0 is the reaction free energy and ΔG^0 is the activation free energy. λ is the reorganization energy. The red dot marks the transition state where electron transfer occurs.[52]

Given that electron transfer requires structural reorganization of both reactants and products to optimize energetically favored configurations, he introduced the concept of reorganization energy in addition to the thermodynamic driving force (i.e., Gibbs free energy change). Figure 2.3 shows the parabolic curves that represent the potential energy surface of the reactant and product states along the reaction coordinate under the harmonic approximation. The reorganization energy (λ, blue arrow) which corresponds to the energy required to reorganize the nuclear configuration of the system and surrounding environment from the equilibrium geometry of one state to that of the other without electron transfer. It consists of an inner-sphere component (λ_{in}) involving changes in the geometries, bond lengths and angles, and an outer-sphere component (λ_{out}) involving reorientation of the surrounding solvent.

$$\lambda = \lambda_{in} + \lambda_{out} \tag{2.23}$$

Considering the reaction free energy and the reorganization energy, the activation free energy ($\Delta G^{\ddagger}$) is defined as the energy barrier at the intersection point of the two parabolas and is given by the following equation,

$$\Delta G^{\ddagger} = \frac{(\lambda + \Delta G^0)^2}{4\lambda} \tag{2.24}$$

where ΔG^0 is the reaction free energy, which is the energy difference between the minima of the reactant and product states.

In the normal region, as ΔG^0 becomes more negative, the activation energy decreases and the reaction rate increases. However, the reaction rate slows down as ΔG^0 becomes even more

negative in the inverted region, especially when ΔG^0 is smaller than λ. Marcus theory demonstrates that thermodynamics controls kinetics, which is built upon classical concepts such as transition states theory, Arrhenius' Law, and the Franck-Condon Principle. In this work, a similar rationale to Marcus theory, where the reaction rate is determined by the activation free energy barrier. By evaluating Gibbs free energy changes of the intermediates and transition states, the reaction barriers can be estimated, which in turn allows us to predict the catalytic activity.

2.2 Computational Approach

In recent decades, density functional theory (DFT) has made significant contributions to advancing electrocatalysis research by providing insights into reaction mechanisms, adsorption energetics, and electronic structures of catalytic materials. For example, activity trends for hydrogen evolution reaction (HER),[53] oxygen evolution reaction (OER),[54] oxygen reduction reaction (ORR)[44] and carbon dioxide reduction (CO_2RR)[55] have been successfully rationalized using DFT calculations. Since Jen Nørskov et al. introduced the computational hydrogen electrode (CHE) approach in 2004,[43] which approximates the free energy of a proton–electron pair at the electrode-electrolyte interface as equal to half the free energy of a hydrogen molecule ($½H_2$), systematic evaluation of electrochemical reaction energetics of metal electrocatalysts has become possible.

However, even though the CHE approach has been widely used for evaluating catalytic activity, its applicability to advanced catalyst systems such as wide band gap semiconductors remains limited.[38] In particular, factors such as surface states, adsorption-induced Fermi level shifts, and defect formation can strongly influence the adsorption energies of reaction intermediates—effects not fully captured by the standard CHE model.

In this chapter, I will introduce a widely used theoretical framework for catalytic reactivity evaluation — CHE approach and furthermore, a new theory model for wide band gap semiconductors which is developed by employing Fermi-Dirac statistics. In this chapter, a widely used theoretical framework for catalytic activity evaluation, CHE approach will be explained. Furthermore, a new theoretical model developed for wide band gap semiconductors by incorporating Fermi–Dirac statistics to account for dynamic Fermi level variations will be introduced.

2.2.1 Computational Hydrogen Electrode (CHE) Approach

In electrochemical reactions, protons and electrons are transferred between an electrode and the electrolyte via a process known as proton-coupled electron transfer (PCET).[56]

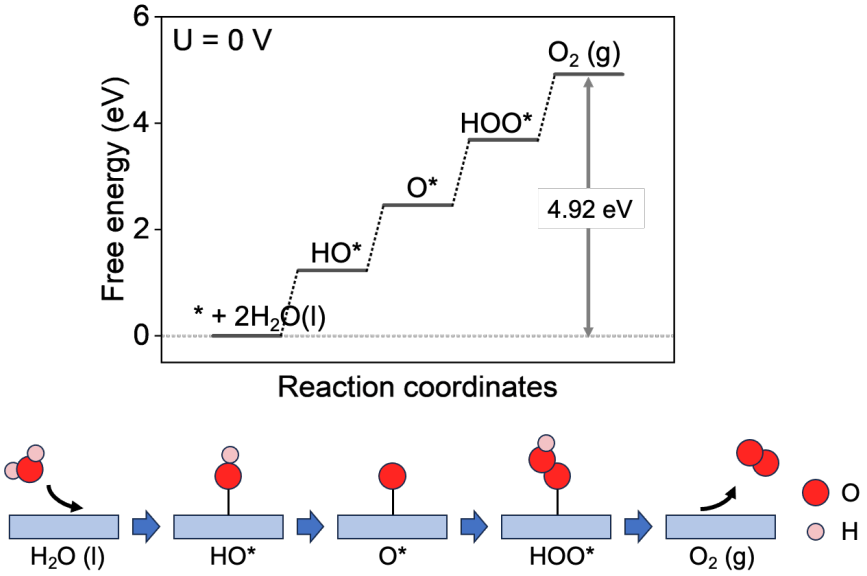

Figure 2.4 Standard free energy diagram for the OER at zero potential (U = 0)[54] and schematic illustration of OER process.

For example, the elementary steps of the oxygen evolution reaction (OER) in water splitting (which will be discussed in Chapter 4.2) are presented by,

$$(1)\ H_2O\ (l) + * \rightarrow *OH + H^+ + e^-$$
$$(2)\ *OH \rightarrow *O + H^+ + e^-$$
$$(3)\ H_2O\ (l) + *O \rightarrow *OOH + H^+ + e^-$$
$$(4)\ *OOH \rightarrow O_2 + * + H^+ + e^-$$

where * denotes an active site on the catalyst surface. In each step, both a proton and an electron are transferred. The reaction spontaneity of each step can be evaluated by the change in Gibbs free energy, ΔG_i (i = 1,2,3,4):[54]

$$\Delta G_1 = G_{OH^*} - G_{H_2O(l)} - G_* + \mu_{H^+} + \mu_{e^-} \quad (2.25)$$
$$\Delta G_2 = G_{O^*} - G_{OH^*} + \mu_{H^+} + \mu_{e^-} \quad (2.26)$$
$$\Delta G_3 = G_{OOH^*} - G_{H_2O(l)} + \mu_{H^+} + \mu_{e^-} \quad (2.27)$$
$$\Delta G_4 = G_{O_2(g)} - G_{OOH^*} + \mu_{H^+} + \mu_{e^-} \quad (2.28)$$

Here, G_{OH^*}, G_{O^*}, and G_{OOH^*} are the Gibbs free energies of the OER intermediates, OH, O, and OOH, respectively. $G_{H_2O(l)}$ and $G_{O_2(g)}$ correspond to the Gibbs free energies of liquid water and gaseous oxygen; and μ_{H^+} and μ_{e^-} are the chemical potential of a proton and an electron, respectively. However, in DFT calculations, PCET reactions in electrocatalysis cannot be straightforwardly described because electrons are treated as part of the delocalized electron density, which is the fundamental framework of DFT. Furthermore, protons do not exist as free particles in aqueous media; instead, they are solvated as hydronium ions (H_3O^+). This complexity makes it challenging to model reactions involving solvated protons explicitly.[57]

To solve these difficulties in modeling electrocatalytic PCET reactions, Jen Norskov et al. proposed the computational hydrogen electrode (CHE) approach in 2004.[43] The CHE approach simplifies the description of the proton-electron pair by referencing it to half a hydrogen molecule (H_2) under standard conditions:

$$H^+ + e^- \leftrightarrow \frac{1}{2}H_2(g)$$

Accordingly, the chemical potentials of a proton (μ_{H^+}) and electron (μ_{e^-}) in each elementary step are referenced to the free energy of a hydrogen molecule (G_{H_2}),

$$\mu_{H^+} + \mu_{e^-} = \frac{1}{2}G_{H_2} \text{ (at pH = 0, U = 0 V)} \quad (2.29)$$

Under realistic electrochemical conditions, i.e., finite pH and applied bias, the free energy is further corrected by the contributions of pH (ΔG_{pH}) and applied bias U (ΔG_U):

$$\Delta G_{pH} = -k_B T pH ln10 \approx -0.059pH \quad (2.30)$$

$$\Delta G_U = -eU \quad (2.31)$$

where k_B is the Boltzmann constant and T is the absolute temperature, respectively. This approach enables the construction of potential-dependent free energy diagrams for electrochemical reactions without explicitly modeling solvated protons and applied potentials in DFT calculations.

The Gibbs free energy of adsorbates in Eqs (2.25) – (2.28) can be obtained from DFT calculations. For a given species i, the Gibbs free energy (G_i) is given by:

$$G_i = H_i - TS_i \quad (2.32)$$

where H_i is the enthalpy and S is the entropy at temperature T. The enthalpy H_i is presented by:

$$H_i = U_i + PV \quad (2.33)$$

where P is the pressure and V is the system volume. The solid-phase reactions are carried out under nearly constant pressure and volume; therefore, the PV term in Eq (2.33) can be neglected. The primary component of the internal energy U_i in Eq (2.33) is the total energy (E_{DFT}) obtained from DFT calculations. DFT provides the electronic ground-state energy within **the Born-Oppenheimer approximation**, which assumes that nuclei are stationary because they are much heavier than electrons, therefore ignoring nuclear motion and thermal effects. The electronic contribution is described by **the Kohn-Sham equation**, which account for kinetic energy, external potential energy, the Hartree term, and exchange-correlation effects. As a result, the total energy computed by DFT (E_{DFT}) is given as:

$$E_{DFT} = E_{electronic} + E_{nucleus\ repulsion} \tag{2.34}$$

where $E_{electronic}$ is the electronic energy obtained from the Kohn-Sham equations, and $E_{nucleus\ repulsion}$ is the repulsive interaction between nuclei. A detailed discussion of DFT background will be provided in Chapter 3. To bridge the gap between the ground-state energy computed by DFT under the Born-Oppenheimer approximation and the experimentally relevant Gibbs free energy at finite temperature including the influence of the surrounding solvent environment, it is necessary to include correction terms accounting for (i) quantum mechanical effects (ii) thermal effects to the enthalpy and entropy and (iii) solvation effect.

(i) Quantum mechanical correction: Zero-point energy (ZPE)

In quantum mechanics, the energy levels are quantized due to Heisenberg's uncertainty principle. The energy levels for a quantum harmonic oscillator are defined by:

$$E_n = \hbar\omega(n + \frac{1}{2}) \tag{2.35}$$

where $\hbar$, ω, and n are the reduced Planck constant ($\hbar$ = $h/2\pi$, h is Planck constant), the vibrational frequency eigenvalue, and the vibrational quantum number, respectively.

The energy for the ground state (n = 0) is:

$$E_0 = \frac{1}{2}\hbar\omega \tag{2.36}$$

This energy is referred to as the zero-point energy (ZPE). It indicates that a system still has the minimum vibrational energy even at 0 K due to quantum effects. However, density functional theory (DFT) does not consider vibrational contributions in total energy calculations, resulting in an underestimation of the total energy. Therefore, it is necessary to consider the zero-point energy (ZPE) for accurate total energy calculations,

$$ZPE = \frac{1}{2}\sum_i \hbar\omega_i \tag{2.37}$$

where ω_i is the vibrational frequency eigenvalue of *i*-th mode.

(ii) Thermal effects corrections: Heat Capacity (C_p) and Entropy (S)

Thermal effects arise from translational, rotational, and vibrational motions, which describe the behavior of molecules at a finite temperature. For example, the total energy of a system increases when the temperature increases because atoms will move and vibrate faster. However, given that the movement of adsorbed molecules on the solid surface is restricted, translational and rotational contributions are negligible; vibrational entropy dominantly contributes to the free energy. In practice, the extent of this restriction depends on the adsorption type: in physisorption, adsorbates may retain partial translational and rotational degrees of freedom due to weak van der Waals interaction, whereas in chemisorption, strong chemical bonding to the surface effectively suppresses these motions, making vibrational modes as the primary thermal contribution.[58] As a result, the correction terms of heat capacity ($\int C_p dT$) and entropy (ΔS) to account for thermal effects are given by:[59]

$$\int C_p dT = \sum_i \frac{\hbar\omega_i}{exp\left(\frac{\hbar\omega_i}{k_B T}\right) - 1} \tag{2.38}$$

$$\Delta S = k_B \sum_i \left[\frac{\hbar\omega_i}{\exp\left(\frac{\hbar\omega_i}{k_B T}\right) - 1} - \ln\left(1 - \exp\left(-\frac{\hbar\omega_i}{k_B T}\right)\right)\right] \tag{2.39}$$

(iii) Solvation effect

In electrochemical environments, charged intermediates are stabilized by the surrounding solvent molecules. Since explicit solvent modeling is computationally demanding, solvation effects are often approximated by implicit solvation models, which treat the solvent as a polarizable continuum medium. The corresponding free energy correction (ΔG_{solv}) accounts for this stabilization at the solid-liquid interface and can be included as an additional term in the Gibbs free energy equation.[60]

To sum up, the change of Gibbs free energy is given by:

$$\Delta G = \Delta E_{DFT} + \Delta ZPE + \int C_p dT - T\Delta S + \Delta G_{pH} + \Delta G_U + \Delta G_{solv} \tag{2.40}$$

2.2.2 Fermi Level-dependency of Adsorption Energy Theory Model

In conventional studies, only the atoms of reactants and products were considered when calculating the Gibbs free energy change of chemical reactions (ΔG_{tot}), which is given by:

$$\Delta G_{tot} = \sum_i n_i \Delta \mu_i \tag{2.41}$$

where n_i is the number of moles and $\Delta \mu_i$ is the change in chemical potential of species *i*, which are involved in the reaction. However, while conventional semiconductors such as silicon (Si) exhibit high carrier mobilities with delocalized charges,[61] metal oxide semiconductors often show charge localization due to their low carrier concentration and weak dielectric screening.[62] These localized charges can contribute to charge transfer between adsorbates and the semiconductor. Hence, in systems where charge transfer involves electrons, it is important to consider the chemical potential of electrons in the Gibbs free energy calculations.

An electron with a half-integer spin is a type of fermion obeying the Pauli exclusion principle; in other words, electrons cannot simultaneously occupy the same energy state. It follows a specific statistical distribution known as the Fermi-Dirac distribution, which is given by:[63]

$$F(E) = \frac{1}{1 + e^{(E-E_F)/k_B T}} \tag{2.42}$$

where E, E_F, and k_B are the energy level, the Fermi level, and the Boltzmann constant. The Fermi level represents the energy at which the probability of electron occupancy is 50 % at absolute zero (T = 0 K). At this temperature, all electronic states below E_F are fully occupied, while those above E_F are empty, resulting in a sharp occupation step at the Fermi level. At finite temperature (T > 0 K), on the other hand, this sharp edge is smeared out due to thermal excitations, and the Fermi–Dirac distribution describes the gradual variation of occupancy near E_F.[63]

While the chemical potential for the adsorbates in gas- or liquid phases is related to the highest occupied molecular orbital (HOMO) and the lowest unoccupied molecular orbital (LUMO), in solids, the chemical potential of electrons is represented by the Fermi level, which is determined by the band structure and the electron occupancy of the conduction and valence bands. In metals, where the conduction band maximum (CBM) and valence band minimum (VBM) overlap, electrons occupy states up to E_F at 0 K. In intrinsic semiconductors, the Fermi level lies near the middle of the band gap because the concentrations of electrons and holes are

equal. When the balance of charge carrier concentrations is disrupted by impurities such as dopants or defects, the Fermi level shifts, and the semiconductor with impurities becomes an extrinsic semiconductor. For example, donor impurities shift the Fermi level closer to CBM, giving rise to an n-type semiconductor. On the other hand, electron acceptors are doped into a semiconductor, resulting in a p-type semiconductor.[61]

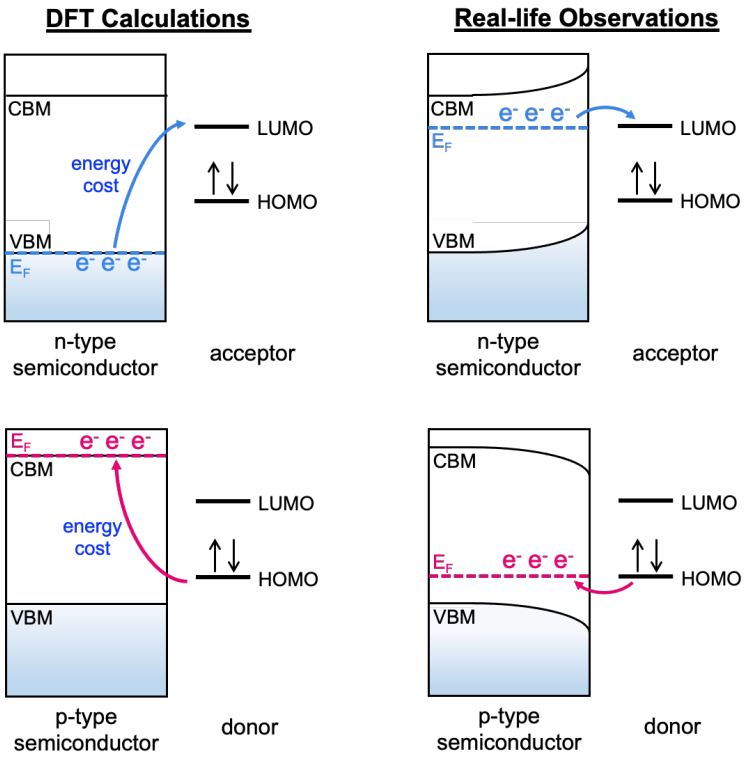

Figure 2.5 A schematic illustration of the inevitable error of adsorption energy between DFT calculations and real-life observations.[38]

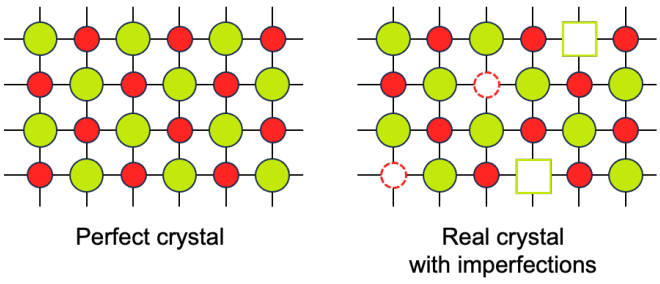

Figure 2.6 Schematic of a metal oxide (MO_X)-layer as considered in DFT and as observed under real-life consideration. Green and red balls represent metal (M) and oxygen of metal oxides. Green squares and red dashed circles represent cation vacancies and oxygen vacancies, respectively.

The charge transfer between a substrate and adsorbates during chemisorption is governed by the difference in their electrochemical potentials. It is important to accurately consider the relative positions of the Fermi level of a substrate and HOMO/LUMO level of adsorbates. HOMO/LUMO level is an intrinsic property of gas- or liquid-phase adsorbates, while the Fermi level of a substrate is changeable depending on the property of materials, consequently the Fermi level of a substrate determines the tendency for charge carrier transfer during the reaction.

The catalytic phenomena of a metallic catalyst have been well explained because the electronic structure of metallic catalysts does not significantly change by charge transfer due to sufficient charge carrier concentration. However, understanding the catalytic phenomenon of semiconductor catalysts with low charge carrier concentrations is elusive. As shown in Figure 2.5, if the Fermi level is close to the HOMO level of the adsorbates, electrons will be transferred from the adsorbate to the substrate. In contrast, the Fermi level of the substrate and LUMO level of the adsorbate are close; electrons will be donated from the substrate to the adsorbate. The energy cost for the adsorption (adsorption energy) depends on the position of the Fermi level of a semiconductor, which is easily changeable by charge transfer. Therefore, it is significant to consider the effect of the variable Fermi level of a wide band gap semiconductor on the catalytic reaction.

Even though the CHE approach has contributed to the recent significant progress in the field of heterogeneous catalysts, it is still challenging to study the catalytic phenomena on a wide band gap semiconductor by using the standard CHE method because of the following reasons:

(1) Theory and experiments have too large discrepancies for wide band gap semiconductors. In typical DFT calculations, the materials are treated as a perfectly periodic crystal without the consideration of imperfections of real crystals. (Figure 2.6) Moreover, although the tunable Fermi level of wide band gap semiconductors is one of the key factors determining the catalytic activity, it has been mostly neglected in DFT calculations. The Fermi level is determined by filling electronic states in order of increasing energy, under the assumption of zero temperature (T = 0 K). Consequently, the edge of VBM is often considered as the Fermi level in semiconductors, possibly resulting in an overestimation of the energy cost of charge transfer between the substrate and the adsorbate.

(2) To optimize doping concentration using DFT calculations, an impractically large supercell is needed to represent the very low doping levels observed in experiments. In general, DFT calculations become increasingly time-consuming and costly as the number of atoms (N) increases; the computational cost scales as N^3.[64]

To overcome the limitations of the currently adopted standard CHE approach, a new theoretical model, “Fermi level dependency of adsorption energy theory model” has been developed.[38] Considering the correlation between the Fermi level position and the adsorption energy, the Gibbs free adsorption energy of adsorbates (ΔG_{ads}) is expressed as a function of the Fermi level as follows:

$$\Delta G_{ads} = \Delta E_0 + \Delta ZPE + \int C_p dT - T\Delta S + q(\varepsilon_F + E_{VBM}) \quad (2.43)$$

where ΔE_0, q, ε_F and E_{VBM} are the binding energy, the charge state of adsorbates, the Fermi level ranged over the band gap of a semiconductor, and the DFT-computed eigenvalue of the VBM energy level of the slab model of a semiconductor with the adsorbate, respectively. In this approach, since charge transfer can result in various charge states of the adsorbates, all possible charge states of the adsorbates should be accounted for in this theory. The theoretical studies in this thesis will employ this theory model to elucidate the catalytic behavior.

Chapter 3

Computational Methods

In 1998, Walter Kohn and John Pople won the Nobel Prize in Chemistry for their contributions of density functional theory (DFT) to the development of computational methods in quantum chemistry.[65] DFT is groundbreaking for theoretical chemistry because it allows us to understand the electronic structure of large, complex systems by solving the many-body wavefunctions and enables the applications of computational methods to address practical problems in chemistry with much greater efficiency. DFT has a significant impact on condensed matter physics, computational physics, and quantum chemistry, making it possible to study complex systems with improved accuracy by capturing the essential properties of many-body interactions. The following chapter provides a brief overview of DFT, a fundamental tool for the computational work conducted in this thesis.

3.1 Theoretical Background

This part has been prepared with reference to the textbook, Richard M. Martin, *Electronic Structure: Basic Theory and Practical Methods,* Cambridge University Press, 2004, and David J. Griffiths, Darrell F. Schroeter, Introduction to Quantum Mechanics, Cambridge University Press, 3rd edition, 2018.[66,67]

3.1.1 Many-Body Wavefunction Problem

In quantum mechanics, the behavior of electrons and nuclei within the system is described by wavefunctions governed by the Schrödinger equation, which explains how the quantum state of the system evolves over time. However, for stationary states in which the wavefunction is separable into spatial and temporal parts, the time-independent Schrödinger equation is applied. This equation explains how the energy and wavefunction are determined by the coordinates of the particles within the system and is written as,

$$\hat{H}\Psi = E\Psi \tag{3.1}$$

where $\hat{H}$, E and Ψ in Eq (3.1) represent the Hamiltonian, the energy and the wavefunction, respectively.

For a system containing *N* electrons and *M* nuclei, the Hamiltonian can be written as:

$$\hat{H} = -\frac{1}{2}\sum_{i=1}^{N}\nabla_i^2 - \frac{1}{2}\sum_{I=1}^{M}\frac{\nabla_i^2}{M_I} - \sum_{i=1}^{N}\sum_{I=1}^{M}\frac{Z_I}{|r_i - R_I|} + \sum_{i=1}^{N}\sum_{j\neq i}^{N}\frac{1}{|r_i - r_j|} + \sum_{I=1}^{M}\sum_{J\neq I}^{M}\frac{Z_I Z_J}{|R_I - R_J|} \quad (3.2)$$

Eq (3.2) can be compactly written as:

$$\hat{H} = \hat{T}_e + \hat{T}_n + \hat{V}_{en} + \hat{V}_{ee} + \hat{V}_{nn} \quad (3.3)$$

where Z_I is the charge of nucleus I, and M_I is the the mass of nucleus I expressed in units of the electron mass. The distance between the i^{th} electron and the I^{th} nucleus is given by position vectors r_i and R_I, respectively. The first two terms in Eq (3.3) are the kinetic energy of electrons ($\hat{T}_e$) and nuclei ($\hat{T}_n$), respectively. The final three terms in Eq (3.3) are Coulomb interaction between electrons and nuclei ($\hat{V}_{en}$), repulsion between electrons ($\hat{V}_{ee}$) and repulsion between nuclei ($\hat{V}_{nn}$), respectively. The many-body wavefunction problem with ($3N + 3M$) degrees of freedom involves numerous interactions of all particles within the system. Accordingly, the Schrödinger equation becomes more complicated to solve as the size of the system increases; several approximations are needed.

3.1.2 Born-Oppenheimer Approximation

In 1927, the Born-Oppenheimer (BO) approximation was formulated to simplify the complex many-body problem by separating the nuclei motions from the electron motions. According to the fact that nuclear masses are approximately 10^4 times heavier than the mass of an electron, nuclei move relatively slowly while electrons move rapidly.[68] Hence, it is assumed that the nuclei can be considered as fixed-point charges and electrons follow the motion of nuclei. This enables us to determine the same stationary state using the electron Hamiltonian ($\hat{H}_{elec}$) instead of $\hat{H}$ in Eq (3.3), which can be described as:

$$\hat{H}_{elec} = -\frac{1}{2}\sum_{i=1}^{N}\nabla_i^2 - \sum_{i=1}^{N}\sum_{I=1}^{M}\frac{Z_I}{|r_i - R_I|} + \sum_{i=1}^{N}\sum_{j\neq i}^{N}\frac{1}{|r_i - r_j|} = \hat{T}_e + \hat{V}_{en} + \hat{V}_{ee} \quad (3.4)$$

The solution of the Schrödinger equation with $\hat{H}_{elec}$ is the electronic wavefunction (Ψ_{elec}) and the electronic energy (E_{elec}), describing the motion of the electrons.

$$\hat{H}_{elec}\Psi_{elec} = E_{elec}\Psi_{elec} \quad (3.5)$$

The total energy (E_{tot}) with the assumption of stationary nuclei is the sum of E_{elec} and the constant nuclear repulsion term (E_{nuc}), which can be described as,

$$E_{tot} = E_{elec} + E_{nuc} = E_{elec} + \sum_{I=1}^{M}\sum_{J\neq I}^{M}\frac{Z_I Z_J}{|R_I - R_J|} \quad (3.6)$$

Despite the simplification of many-body wave function (the full Hamiltonian) by BO approximation, it is still complex to solve the Schrödinger equation for many body systems because the electron wave function is a function of 3*N* independent variables.

3.2 Density Functional Theory (DFT)

The development of density functional theory (DFT) by Hohenberg, Kohn, and Sham marked a significant milestone in addressing the electronic structure problem and providing a new atomic-scale approach to describing the physical and chemical properties of matter. Density functional theory (DFT) employs the electron density $\rho(r)$ as the fundamental variable instead of the wave function. This approach simplifies the problem by reducing the degrees of freedom from 3*N* (where *N* is the number of electrons) to just three independent variables (x, y, and z), as $\rho(r)$ depending only on spatial coordinates. Therefore, this simplification is particularly useful for considering electron-electron interactions, making it more computationally efficient to study the properties of many-electron systems.

In this section, we will discuss the fundamental approaches in DFT: (i) the Hohenberg-Kohn theorems, which enable the use of ground-state electron density, (ii) the Kohn-Sham equation, which is used to compute the ground-state density and energy in practice. Furthermore, the exchange-correlation functionals are introduced to simplify the effects of electron-electron interactions for reducing computational complexity.

3.2.1 Hohenberg-Kohn Theorems

Hohenberg and Kohn provided two theorems, meaning that the properties in the ground states for the systems with many-electrons can be calculated from electron density $\rho(r)$ with the consideration of the electron-electron interactions in a system in an external potential $v_{ext}(r)$.

Theorem I: The external potential $v_{ext}(r)$ is uniquely determined by the ground-state electron density $\rho_0(r)$ of an arbitrary system.

Theorem II: The exact ground state can be calculated by minimizing the total energy functional of given electron density $\rho(r)$.

Accordingly, for any trial electron density $\rho(r)$, the total energy $E[\rho]$ is always greater than or equal to true ground-state energy E_0 corresponding to the true ground-state density $\rho_0(r)$ ($E[\rho] \geq E_0[\rho_0]$). Therefore, the total energy functional $E[\rho]$ can be considered as a functional of the electron density and the Hamiltonian is,

$$\hat{H} = -\frac{1}{2}\sum_i \nabla_i^2 - \sum_i v_{ext}(r_i) + \sum_i \sum_{j \neq i} \frac{1}{|r_i - r_j|} = \hat{T}_e + \hat{V}_{ext} + \hat{V}_{ee} \tag{3.7}$$

where $v_{ext}(r_i)$ is an external potential including the interactions between electrons and nuclei, which is rewritten as,

$$v_{ext}(r_i) = -\sum_I \frac{Z_I}{|r_i - R_I|} \tag{3.8}$$

The total energy functional can be expressed as follows,

$$\mathrm{E}[\rho] = T[\rho] + V_{ee}[\rho] + \int v_{ext}(r)\rho(r) \tag{3.9}$$

where $T[\rho]$ and $V_{ee}[\rho]$ represent the kinetic energy functional and electron-electron interaction functional for given electron density $\rho(r)$, respectively. The last term of Eq (3.9), $\int v_{ext}(r)\rho(r)dr$ is the interaction energy between the external potential and the electron density. This external potential energy term is written in a more compact form as follows:

$$V_{ext}[\rho] = \int v_{ext}(r)\rho(r)dr \tag{3.10}$$

Accordingly, the total energy functional can be expressed as:

$$\mathrm{E}[\rho] = T[\rho] + V_{ee}[\rho] + V_{ext}[\rho] \tag{3.11}$$

The functionals $T[\rho]$ and $V_{ee}[\rho]$ are independent on the external potential $v_{ext}(r)$. We can represent the two functionals by using the universal Hohenberg-Kohn functional $F_{HK}[\rho]$ as follows:

$$F_{HK}[\rho] = T[\rho] + V_{ee}[\rho] \tag{3.12}$$

Consequently, the total energy functional is given by:

$$\mathrm{E}[\rho] = F_{HK}[\rho] + V_{ext}[\rho] \tag{3.13}$$

3.2.2 Kohn-Sham Equations

3.2.2.1 Derivation of the Kohn-Sham Equations

In practice, even though the Hohenberg-Kohn theorems form the essential foundation of DFT by reformulating the many-body problem in terms of the electron density, calculating the electron-electron interactions directly from ground state electron density $\rho(r)$ is still not

feasible. In 1965, Kohn and Sham introduced the Kohn-Sham (KS) equation based on the Hohenberg-Kohn (HK) theorems by constructing an auxiliary system of non-interacting electrons that has the same electron density, allowing the functional to be minimized by varying the Kohn-Sham orbitals from which the density is constructed.[69]

The ground-state density of a non-interacting system $\rho_{KS}(r)$ is equal to the true ground-state density $\rho(r)$. Kohn and Sham decomposed the universal HK functional ($F_{HK}[\rho]$) in Eq (3.12) into the energy functional (F[ρ]) in three terms as follows:

$$\mathrm{F}[\rho] = T_s[\rho] + V_H[\rho] + E_{xc}[\rho] \tag{3.14}$$

where the first term of Eq (3.14) is the kinetic energy of non-interacting electrons ($T_s[\rho]$). The second term in Eq (3.14) is the classical Hartree electrostatic energy corresponding to the Coulombic energy of electron-electron interaction, equal to the classical electrostatic energy of the charge distribution $\rho(r)$, which is given by:

$$V_H[\rho] = \frac{1}{2}\iint \frac{\rho(r)\rho(r')}{|r-r'|}\,drdr' \tag{3.15}$$

The third term of Eq (3.14) is the non-trivial exchange-correlation (XC) energy to account for the energy difference between the hypothetical non-interacting Kohn-Sham system and the equivalent fully interacting system of electrons in a real system. We will discuss E_{xc} term in more detail in the following section 3.2.3.

The total energy functional ($E[\rho]$) of the Kohn-Sham equation is given by:

$$E[\rho] = T_s[\rho] + \frac{1}{2}\iint \frac{\rho(r)\rho(r')}{|r-r'|}\,drdr' + E_{xc}[\rho] + \int v_{ext}\,(r)\rho(r)dr \tag{3.16}$$

which can be rewritten as:

$$E[\rho] = T_s[\rho] + V_H[\rho] + E_{xc}[\rho] + V_{ext}[\rho] \tag{3.17}$$

The Kohn-Sham equations are derived by applying the variational principle. The goal is to find the set of orbitals, ψ_i, that minimize the total energy functional. To retain the orthonormality of the orbitals, as required by the Pauli exclusion principle, a set of Lagrange multipliers is introduced to minimize the total energy functional with respect to the orbitals. This constraint ensures that each single-electron wavefunction $\psi_i(r)$ satisfying the orthonormality condition with all other orbitals $\psi_j(r)$:

$$\int \psi_i^*(r)\psi_j(r)dr = \delta_{ij} \tag{3.18}$$

This constrained minimization problem leads to a set of single-particle equations where the orbital energies ϵ_i appear as Lagrange multipliers for the orthonormality constraint. The

resulting Kohn-Sham equations take the form of an effective single-electron Schrödinger equations as follows:

$$\widehat{H}_{KS}\psi_i(r) = \epsilon_i\psi_i(r) \tag{3.19}$$

where $\psi_i(r)$ is the *i*-th Kohn-Sham orbital and ϵ_i is its corresponding orbital energy.

The Kohn-Sham Hamiltonian (H_{KS}) consists of the kinetic energy operator and an effective potential that includes the Hartree, exchange-correlation, and external potentials:

$$\widehat{H}_{KS} = [-\frac{1}{2}\nabla^2 + v_{KS}(r)] \tag{3.20}$$

where v_{KS} term is rewritten as:

$$v_{KS}(r) = v_H(r) + v_{xc}(r) + v_{ext}(r) \tag{3.21}$$

where $v_H(r)$ is Hartree potential:

$$v_H(r) = \int \frac{\rho(r')}{|r - r'|} dr' \tag{3.22}$$

and $v_{xc}(r)$ is the exchange-correlation potential, which is related to the exchange-correlation energy functional $E_{xc}[\rho(r)]$ according to the equation as follows:

$$v_{xc}(r) = \frac{\delta E_{xc}[\rho]}{\delta\rho(r)} \tag{3.23}$$

and $v_{ext}(r)$ represents the external potential, which is usually the electron-nucleus interactions.

Now, the Kohn-Sham orbitals are used to obtain the total ground-state electron density ($\rho(r)$) by using Eq (3.24):

$$\rho(r) = \sum_i^n |\psi_i(r)|^2 \tag{3.24}$$

3.2.2.2 Self-consistency in Kohn-Sham Equations

In the Kohn-Sham equations, there is an interdependency among the Kohn-Sham potential $v_{KS}(r)$, electron density $\rho(r)$, and wavefunctions $\psi_i(r)$. The Kohn-Sham potential depends on the electron density, which is calculated from the Kohn-Sham wavefunctions using Eq (3.17). To obtain Kohn-Sham wavefunctions, however, the Kohn-Sham equations – which involve the Kohn-Sham potential – must be solved. Therefore, an iterative self-consistent field (SCF) procedure is required to achieve a converged solution for the Kohn-Sham equations. Figure 3.1 shows the self-consistent cycle of the Kohn-Sham equations.

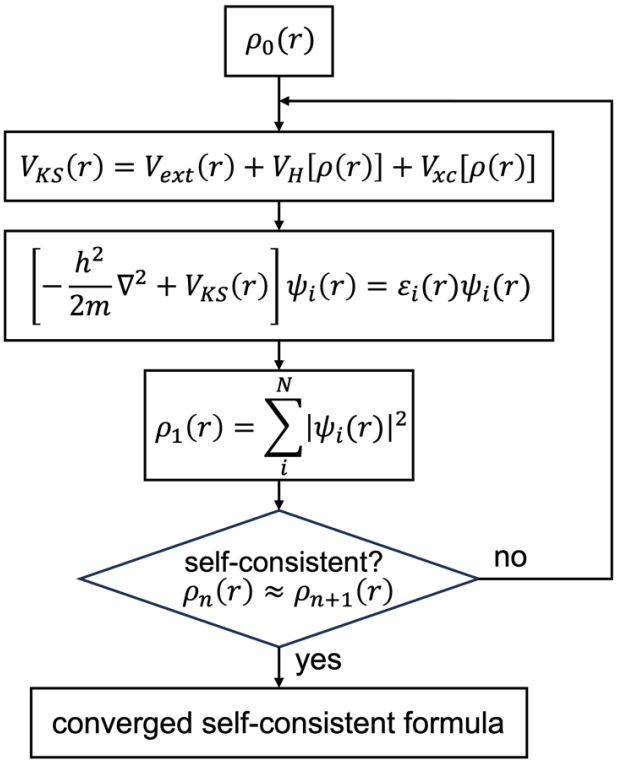

Figure 3.1 A flow-chart of the self-consistency in the Kohn-Sham equation.

1) Initial guess for electron density $\rho_0(r)$

The initial electron density $\rho_0(r)$ is an estimate of the electron distribution based on atomic wave functions, atomic electron densities or electrostatic potentials. This estimated density is used as the input for the self-consistency cycle in the Kohn-Sham equations.

2) Solving the Kohn-Sham potential and equations

The Kohn-Sham potential $v_{KS}(r)$ is calculated using the initial electron density $\rho_0(r)$. Then, the Kohn-Sham equations are solved using this potential to find a new set of occupied single-particle orbitals $\psi_i(r)$.

3) Calculate new electron density $\rho_1(r)$ and check for convergence

A new electron density $\rho_1(r)$ is obtained from the calculated Kohn-Sham wavefunctions $\psi_i(r)$ and is then compared with the initial electron density $\rho_0(r)$. If the density has not converged, use the new electron density is used to solve the Kohn-Sham equations again. This process is repeated until the input electron density $\rho_n(r)$ differs negligibly from $\rho_{n+1}(r)$, thereby achieving self-consistency:

$$\rho_n(r) \approx \rho_{n+1}(r) \tag{3.25}$$

4) Achieving self-consistency

The final output electron density represents the ground state of the system under the given external potential and interactions. Once the self-consistent field (SCF) procedure has converged within a specified tolerance, the ground-state total energy $E[\rho]$ can be evaluated using the converged electron density $\rho(r)$, which is given by:

$$E[\rho] = \sum_{v} \epsilon_v - V_H[\rho] - \int v_{xc}(r)\rho(r)dr + E_{xc}[\rho] \tag{3.26}$$

where $\sum_v \epsilon_v$ is the sum of the Kohn-Sham orbital energies, $V_H[\rho]$ is the Hartree energy functional, $\int v_{xc}(r)\rho(r)dr$ is the energy contribution from the exchange-correlation potential, and $E_{xc}[\rho]$ is the exchange-correlation energy functional, respectively.

3.2.3 Exchange-Correlation Functionals

In the Kohn-Sham equation, the exact form of the exchange-correlation (XC) functional (E_{XC}) is not known because the interactions between electrons are highly complicated. Therefore, the system of interacting particles is represented by an approximate XC functional rather than an exact form.

The exchange-correlation functional (E_{XC}) consists of two terms: (i) exchange energy (E_X) and (ii) correlation energy (E_C):

$$E_{XC}[\rho] = E_X[\rho] + E_C[\rho] \tag{3.27}$$

The exchange energy (E_X) is the term to account for the interaction between electrons which are indistinguishable Fermions, obeying antisymmetric wavefunctions. Due to the Pauli exclusion principle, electrons with the same spin cannot occupy the same space and keep being separated from each other, resulting in a reduction of the Coulomb repulsion between electrons. The exchange energy E_X reduces the self-interaction errors arising from the spurious Coulomb interaction of an electron with itself in the Hartree term, therefore enhancing the accuracy of predicted electronic properties.

The correlation energy (E_C) accounts for the dynamic electron-electron correlations, particularly those with opposite spins, which are not considered by the mean-field Coulomb of the Hartree and exchange interactions. In principle, the correlation energy can be obtained by solving the many-electron Schrödinger equation, which is computationally infeasible for most systems and thus requires approximations in practical DFT calculations.

3.2.3.1 Local Density Approximations (LDA)

The Local Density Approximation (LDA) is a simple approximation to the exchange-correlation functional based on the assumption that the electron density is locally uniform as in a homogeneous electron gas.[70] Under this assumption, the electron density $\rho(r)$ is considered constant within an infinitesimal volume element, allowing the exchange-correlation energy to be evaluated point by point in real space. The LDA exchange-correlation functional is written as:

$$E_{XC}^{LDA}[\rho] = \int \epsilon_{XC}^{LDA}[\rho(r)]\rho(r)d^3r \tag{3.28}$$

where $\epsilon_{XC}^{LDA}[\rho(r)]$ is the exchange-correlation energy per electron in a homogeneous electron gas system.

The exchange contribution from a homogeneous electron gas is given by:

$$E_X^{LDA}[\rho] = C\int \rho^{\frac{4}{3}}(r)dr = -\frac{3}{4}(\frac{3}{\pi})^{\frac{1}{3}}\int \rho^{\frac{4}{3}}(r)dr \tag{3.29}$$

However, the correlation energy density for a uniform electron gas does not have an exact functional form. Instead, it has been estimated using Quantum Monte Carlo (QMC) simulations, which use stochastic sampling to approximate the correlation energy of a homogeneous electron gas. While LDA can successfully predict certain ground-state properties, such as total energy, bond lengths, and electronic properties, it has significant limitations for non-uniform and real systems with significant spatial inhomogeneity. In particular, LDA systematically underestimates molecular bond energies and band gaps in semiconductors due to an underestimation of the exchange-correlation effects in systems with excited states and non-uniform charge distributions.

3.2.3.2 Generalized Gradient Approximations (GGA)

The Generalized Gradient Approximation (GGA) improves upon the limitations of the Local Density Approximation (LDA) by incorporating not just the local electron density, $\rho(r)$ but also the spatial gradient of the electron density $\nabla\rho(r)$ into the formulation of the exchange-correlation energy.[71–73] This allows GGA to consider the spatial inhomogeneity of the electron density in real space, thereby providing a more accurate description of the exchange-correlation effects in systems with varying electronic environments. The GGA functional is expressed as:

$$E_{XC}^{GGA}[\rho] = \int \epsilon_{XC}^{GGA}[\rho(r), \nabla\rho(r)]\rho(r)d^3r \tag{3.30}$$

The GGA is classified as a semi-local functional, in contrast to the strictly local nature of the LDA, as it includes information about the spatial variation of the electron density through $\nabla\rho(r)$, which varies at every point in space.

However, GGA still tends to underestimate band gaps in semiconductors and insulators due to its inherent limitations in describing discontinuities in the exchange-correlation potential. Nevertheless, it provides more accurate predictions of bond energies, chemical reactivity, and intermolecular interactions compared to LDA, making it a more reliable approximation for many chemical and physical systems.

The Perdew-Burke-Ernzerhof (PBE) functional is one of the most widely adopted in solid-state physics and materials science, due to its versatility and balanced performance. PBE is a non-empirical functional constructed based on several known exact constraints satisfied by the true exchange-correlation functional, without relying on experimental data fitting. As a result, it provides reasonably accurate predictions of physical and chemical properties for a variety of systems.

3.3 Computational Implementations

3.3.1 Plane-wave Basis Sets

Electron wave functions are expanded on a finite set of basis functions, which transforms the series of single-particle Schrödinger equations into a matrix equation.[67] As a result, plane-wave basis sets are used to represent the wave functions of electrons in a material. A plane-wave is written as:

$$\psi_k(r) = e^{ikr} \tag{3.31}$$

where k is the wave vector, and r is the position vector.

Bloch's theorem simplifies the problem of solving the single-particle Schrödinger equation in a periodic potential by reducing it to solving for the periodic function $u_k(r)$. The electron wavefunction $\psi_k(r)$ can be written as:

$$\psi_k(r) = e^{ikr}u_k(r) \tag{3.32}$$

The function $u_k(r)$ is periodic with respect to the lattice, satisfying

$$u_k(r + R) = u_k(r) \tag{3.33}$$

for any lattice vector R. This form significantly reduces the complexity of electronic structure calculations by exploiting the periodicity of the system. This form reflects the translational symmetry of the crystal and allows the wave vector k to be restricted to the first Brillouin zone.

However, while plane waves are suitable for periodic systems such as crystals, a very high resolution is required to accurately describe the rapidly oscillating wave functions of all electrons, especially the tightly bound core electrons near the nucleus. Capturing these sharp variations requires the inclusion of plane waves with a high kinetic energy cutoff, which increases the size of the basis set and consequently the computational costs. To address this, the pseudopotential approximation is introduced to make the plane-wave methods practical by simplifying the interactions near the nucleus.

3.3.2 Pseudopotentials

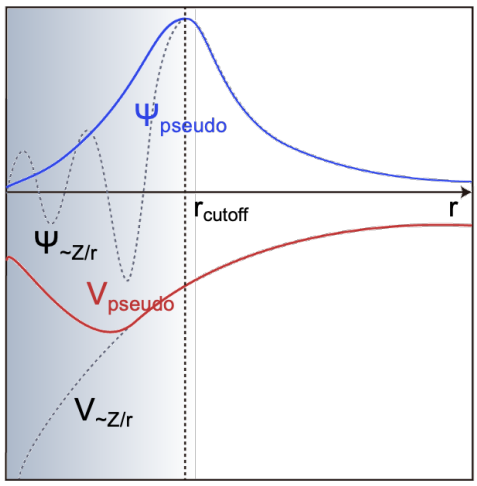

Figure 3.2 A schematic illustration of the comparison of a wavefunction in the Coulomb potential of the nucleus (broken lines) to the one in the pseudopotential (solid line). r_{cutoff} is the cutoff radius, which defines the boundary where the pseudopotential approximation is applied.

In the core region, the valence wave functions must be orthogonal to the core wave functions. To satisfy this orthogonality condition in the presence of the strong ionic potential, the valence wave functions develop rapid oscillations in the core region, which correspond to their high kinetic energy. However, the prediction of electron behavior becomes complicated because it requires a large number of basis functions. Furthermore, since valence electrons are primarily responsible for the physical and chemical properties of materials, explicitly calculating the tightly bound core electrons is often unnecessary. To simplify these calculations, the pseudopotential approximation is introduced.[74] This method replaces the core electrons and a strong ionic potential with a weaker pseudopotential that acts on a set of smoother pseudo-wavefunctions. These pseudo-wavefunctions are nodeless inside a cutoff radius r_{cutoff}

(represented by the blue region in Figure 3.2) but match the true valence wavefunctions in the region beyond r_{cutoff}, therefore requiring a smaller basis set. The pseudopotential approximation modifies the strong Coulomb potential of each nucleus, typically expressed as -1/r, into a smoother effective potential that primarily affects the valence electrons. By approximating the combined effects of the nucleus and core electrons on the valence electrons, pseudopotentials freeze the core states, allowing them to be treated as a single combined potential along with the nucleus. This approach reduces computational complexity while maintaining high accuracy for the electronic properties determined by valence electrons.

3.3.3 The Projector Augmented Wave (PAW) Method

The projected augmented wave (PAW) method, proposed by Blöchl, accurately represents the full electron wavefunctions by combining the accuracy of all-electron methods with the efficiency of pseudopotential. The effect of core electrons is also accounted for through augmentation functions, which describe the electron-nucleus interaction in the core region. Projector functions play an important role by providing a way to transform between the smooth pseudopotential wavefunctions and the true all-electron wavefunctions, ensuring that the core and valence electron effects are accurately captured. This method defines a linear operator to mathematically transform between all-electron and pseudowavefunctions within the spherical core regions. Therefore, unlike pseudopotentials which use the frozen core approximation, the PAW method considers all electrons in the system, allowing for an accurate description of all-electron properties, including those that depend on the core region.

The pseudowavefunction $\tilde{\psi}_n(r)$ can be transformed to the all-electron wavefunction $\psi_n(r)$ by using the central PAW transformation equation:

$$\psi_n(r) = \tilde{\psi}_n(r) + \sum_i \left(\phi_i(r) - \tilde{\phi}_i(r)\right)\langle \tilde{p}_i | \tilde{\psi}_n \rangle \tag{3.34}$$

where $\tilde{\psi}_n(r)$ is a pseudo wavefunction expanded in plane waves, $\phi_i(r)$ is the all-electron partial waves, $\tilde{\phi}_i(r)$ is the corresponding smooth pseudo partial wave, $\langle \tilde{p}_i | \tilde{\psi}_n \rangle$ is the projection of the pseudo-wavefunction onto the projector function $\tilde{p}_i$. This projection measures the contribution of the partial wave $\tilde{\phi}_i$ is contained within $\tilde{\psi}_n$.

3.4 DFT+U Approach

Standard DFT properly describes systems with delocalized electrons, such as *s* and *p* orbitals, by treating each electron as moving in an average field created by all other electrons. However, standard approximations to the DFT exchange-correlation functional, such as the LDA or the GGA, struggle to accurately capture the behavior of systems with localized and strongly correlated electrons, such as *d* and *f* electrons in transition metals or rare earth elements, where electrons are highly interdependent on each other. To address this limitation in precisely describing these systems, the DFT+U method was introduced, incorporating the Hubbard U parameter derived from the Hubbard model.[75] In the Hubbard model, which is designed to describe electron-electron interactions in systems with strongly correlated electrons, the U parameter represents the on-site Coulomb repulsion between electrons occupying the same atomic site. In addition, the DFT+U method can also incorporate an exchange interaction parameter, J, which accounts for the on-site exchange interaction between electrons with parallel spins, further improving the accuracy of the electronic-structure calculations.[76]

The total energy in the DFT+U method can be expressed by adding a correction term to the standard DFT energy. Dudarev et al. proposed a simplified approach that combines the on-site Coulomb (U) and exchange (J) interactions into a single effective parameter U_{eff}:

$$U_{eff} = U - J \tag{3.35}$$

With this correction, the corrected energy functional is simplified to:

$$E_{DFT+U} = E_{DFT} + \frac{U_{eff}}{2}\sum_{i,\sigma}(n_{i\sigma} - n_{i\sigma}^2) \tag{3.36}$$

where E_{DFT} is the standard DFT total energy and n_i is the occupation number of the localized electron state i with spin σ. The term $n_{i\sigma} - n_{i\sigma}^2$ reaches its maximum when the occupation is fractional and is zero for integer occupations. This term penalizes non-integer occupations and therefore correctly promotes electron localization in strongly correlated systems.

Chapter 4

A New Theoretical Model for Predicting Catalytic Activity on Wide Band Gap Semiconductors

In recent years, nanostructured catalysts have been modified to enhance reactivity by heterojunction formation, surface modifications, and doping. Density functional theory (DFT) calculations provide valuable insights into the underlying mechanisms of catalytic reactions, thereby guiding the identification and design of new catalysts. However, as these materials generally have complex compositions and structures, understanding their fundamental mechanisms becomes increasingly challenging; even minor changes in fabrication conditions can markedly reduce the catalytic activity of semiconducting materials. Furthermore, the origins of the significant variations in catalytic activity with particle size, surface morphology, and doping concentration have not been fully understood. It is time-consuming to optimize the performance of catalysts without a solid understanding of the mechanisms. Therefore, a more straightforward and accurate method for elucidating catalytic phenomena remains necessary.

In this chapter, a new method to predict the reactivity of wide band gap semiconductor catalysts is introduced by establishing a multi-scale analytical model. For prototype studies, it was applied to electrocatalytic methane oxidation and further extended to photocatalytic water splitting.

4.1 Electrocatalysis: Overcoming the Limitation of Atomic-scale Simulations on Semiconductor-Catalysis with Changing Fermi Level and Surface Treatment

The content of this chapter is based on the following paper:

Seulgi Ji, Dong Won Jeon, Junghyun Choi, Haneol Cho, Bo-In, Park, Ilpyo Roh, Hyungil Choi, Chansoo Kim, Jung Kyu Kim, Uk Sim, Danlei Li, Hyunseok Ko*, Sung Beom Cho*, Heechae Choi*, *"Overcoming the Limitation of Atomic-scale Simulations on Semiconductor-Catalysis*

with Changing Fermi Level and Surface Treatment", Journal of Materials Chemistry A, 2024, 12, 33537-33545 (Back Cover)

4.1.1 Introduction

4.1.1.1 Methane oxidation on CeO_2-based catalysts in solid oxide fuel cell (SOFC) anodes

Ceria (CeO_2) catalyst has been used as a base material for a long time in various reactions because of the highly reversible Ce^{4+}/Ce^{3+} redox pair and the structural flexibility of its fluorite lattice, which allows facile modifications.[77]

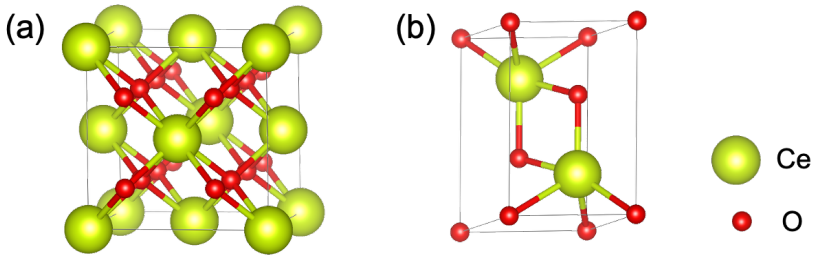

Figure 4.1.1 (a) Fluorite type structure of CeO_2 (face-centered cubic, *Fm-3m*) (b) the sesquioxide A-type structure of CeO_2 (hexagonal, *P-3m1*). Green and red balls indicate Ce and O atoms, respectively.

The redox properties of CeO_2 arise from the reversible transition between CeO_2 and Ce_2O_3. In CeO_2 (fluorite structure), the reduction of Ce^{4+} to Ce^{3+} is accompanied by oxygen vacancy formation. Accumulation of vacancies leads to partial transformation into Ce_2O_3 (sesquioxide structure). This structural flexibility underlies the high oxygen storage capacity and redox activity of CeO_2.[78]

In particular, a number of materials engineering strategies and mechanism studies have been performed to boost and optimize the methane (CH_4) oxidation reaction of CeO_2-based catalysts in solid oxide fuel cells (SOFCs) anodes.[79] As the most widely used routes to improve the catalytic activity of CeO_2 in methane oxidation, cocatalyst depositions, and impurity doping methods have been intensively used.[80–82] Atomic-scale modeling-based computational studies have been performed along with experiments to understand how the catalytic methane oxidation activities of CeO_2 are highly enhanced by up to several orders, even with only tiny coverages of cocatalyst nanoparticle (NP) deposition and/or dilute-limit impurity doping.[83–85] However, it is extremely challenging to investigate mechanisms by experiments and even

density functional theory calculation-based analysis on wide band gap CeO_2[84] because the catalytic activity of CeO_2 catalysts largely varies with the deposited NP size and the doping concentration.[86–89]

Previous theoretical studies often regarded dopant sites on CeO_2 surfaces as the main active sites because of their enhanced catalytic activity.[90–92] However, experimental evidence indicates that Au or Cu dopants in CeO_2 segregate predominantly to grain boundaries,[93–96] which further enhance the intrinsic n-type conductivity of CeO_2 rather than creating new surface active sites.[97,98] Therefore, the key message here is that metal dopants in CeO_2 mainly act as electronic modifiers, not as direct catalytic sites.

For the NP-decorated CeO_2 catalyst case, the synergistic effects in the methane oxidation of metallic Ni/CeO_2 heterojunction were explained using adsorption energy calculations and Mars-Van Krevelen (MvK) mechanism, in which the lattice oxygen atoms of the metal oxide substrates are involved in the oxidation reaction by forming oxygen vacancies.[99,100] However, the assumption that cocatalyst NPs provide the main active sites is not sufficient to explain many other cases. Some studies explained that cocatalyst NPs on CeO_2 can mainly behave as an active site,[84,101] whereas other reports show that the reactivity first increases but subsequently declines as the cocatalyst size grows. This is because large metal particles can cover most of the CeO_2 surface, thereby reducing the number of exposed metal-support interfacial sites.[102,103] Since the catalytic activity primarily originates from these interfacial sites rather than from the metal or CeO_2 alone, excessive cocatalyst loading leads to lower activity. This indicates that the cocatalyst is not the only active site; rather, the reactivity is also governed by support-cocatalyst interactions, such as surface orientation, morphology, termination, and the atomic composition of the cocatalyst NPs on CeO_2. Such evidence contradictory to the conventional assumptions in the modeling schemes implies that the cocatalyst depositions and impurity doping contribute to the changed activity of CeO_2 surface in different ways, which were never discussed. Hence, further mechanistic investigation is necessary to advance the rational engineering of the wide band gap CeO_2 catalyst.

4.1.1.2 Surface modification of a wide band gap semiconductor

Recent experimental and computational research on wide band gap oxide materials has demonstrated that catalytic reactions on the oxide surface are greatly altered by manipulating the Fermi level either by doping or surface treatment.[44,104]

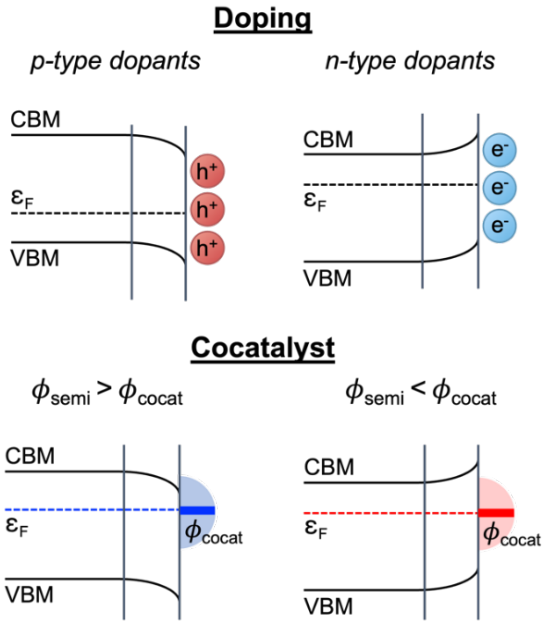

Figure 4.1.1 A schematic illustration of surface Fermi level modification strategies: doping and cocatalyst deposition.

Heterovalent dopants in CeO_2 or point defects can change the bulk Fermi level due to the changed charge carrier concentration, and accordingly band bending occurs near the surface because the bulk Fermi level ($\varepsilon_{F(bulk)}$) and surface Fermi level (ε_F) deviate from each other (Figure 4.1.1).[39,105] Therefore, the surface Fermi level can be modulated by the difference between bulk Fermi level ($\varepsilon_{F(bulk)}$) and the degree of bend banding (ΔV_{BB}) (Eq 4.1.1); although the exact quantitative loading threshold cannot be specified in this study, it can be reasonably assumed that when the loading of cocatalyst NPs on the CeO_2 surface exceeds a critical level sufficient to induce Fermi level alignment between cocatalyst NPs and CeO_2, the surface Fermi level can be directly altered by the band alignment with the work function of the decorated cocatalyst NPs ($\emptyset_{cocat}$) as shown in Figure 4.1.1.[106]

$$\varepsilon_F = \varepsilon_{F(bulk)} - \Delta V_{BB} \tag{4.1.1}$$

4.1.2 Method

4.1.2.1 Computational Method

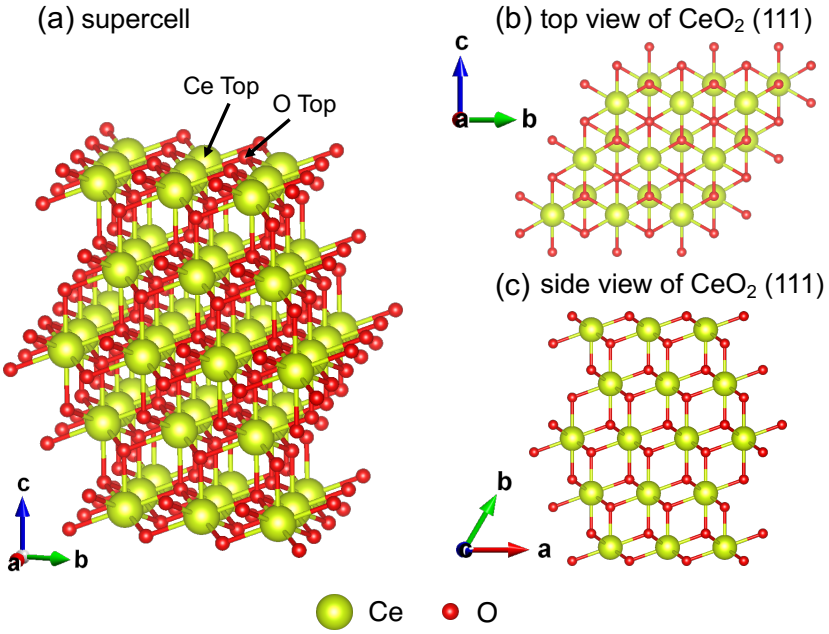

Figure 4.1.2 The model structure for DFT calculations. (a) supercell (b) top view and (c) side view of CeO_2 (111). Light green and red balls represent Ce and O atom, respectively.

DFT calculations were performed using the Vienna *Ab initio* Simulation Package (VASP) with the projector augmented wave method (PAW) to describe the interaction between valence and core electrons.[107–109] All DFT calculations were conducted with the general gradient approximation (GGA) with the Perdew-Burke-Ernzerhof (PBE) exchange-correlation functional.[71,72] Optimization of cell parameters used a Gamma-centered *k*-point grids of 2 x 2 x 1 in a cell for Brillouin zone sampling and a kinetic energy cut-off of 400 eV was used.[110] This work used the DFT + U method, where the introduction of a Hubbard parameter U approximation modifies the self-interaction error and enhances the description of the on-site Coulomb interactions.[111] U_{eff} = 6 eV for Ce is employed to improve the description of the 4f states of Ce.[112] The energy convergence criteria in the self-consistent field were set to 10^{-6} eV and all geometry structures were fully relaxed until Hellman-Feynman forces achieved a range of 0.1 eV $Å^{-1}$. The supercell structure of CeO_2 (111) contains 135 atoms (Ce: 45 atoms, O: 90 atoms) in lateral dimensions of 11.60 Å x 11.60 Å x 33.94 Å. A vacuum region of 20 Å was added perpendicular to the substrate surface to avoid interactions between periodic slabs. The contour maps were plotted using a Python code developed in this work.

4.1.2.2 Gibbs Free Adsorption Energy Calculation

For the precise prediction of the catalytic activity of a wide band gap semiconductor such as CeO_2, the Fermi level dependency of the adsorption energy theory model was applied to calculate Gibbs free adsorption energy (ΔG_{ads}) which is given by:

$$\Delta G_{ads} = \Delta E_0 + \Delta ZPE + \int C_p dT - T\Delta S + q(\varepsilon_F + E_{VBM}) \quad (4.1.2)$$

where E_0 in Eq (4.1.2) is the binding energy of intermediates, which was calculated by considering proton-coupled electron transfer (PCET) processes. It can be obtained by:

$$\Delta E_0 = E_{ads/CeO_2} - E_{CeO_2} - \sum_i n_i \mu_i \quad (4.1.3)$$

where E_{ads/CeO_2} and E_{CeO_2} in Eq (4.1.3) are the total energies of CeO_2 with and without the adsorbates, respectively, n_i is the number of atoms of species *i* (positive for reactant, negative for product), μ_i is the chemical potential of species *i*. The terms ΔZPE, $\int C_p dT$ and ΔS in Eq (4.1.2) mean the changes of zero-point energy, enthalpic and entropy contributions at temperature T to Gibbs free energy of an adsorbates, respectively. q, ε_F and E_{VBM} in Eq (4.1.2) are the possible charge state of the adsorbates due to charge transfer, the Fermi level that ranged over the bandgap of CeO_2 (111), and the DFT-computed eigenvalue of the VBM energy level of CeO_2 (111) slab with the adsorbate, respectively.[31,44,104] Regarding the term q, charge states of intermediates, as the charge transfer occurs during chemisorption, all possible charge states of intermediates should be considered. A detailed discussion regarding the Gibbs free energy calculations considering the partial pressure of reactants was described in the next section 4.1.2.3.

4.1.2.3 Gibbs Free Energy Calculations: The Partial Pressure of Reactants

Gibbs free energies of reaction (ΔG) for each of the reaction pathways were calculated with considerations of the partial pressure of produced H_2O (g) ($P_{H_2O\,(g)}$) in each reaction step depends on the amount of reactants. This assumption gives more reasonable local energetic landscape at each reaction step.

The partial pressure of produced H_2O(g) ($P_{H_2O(g)}$) is dependent on the amount of reactants CH_4(g) and O_2(g), accordingly, we should consider the changeable $P_{H_2O(g)}$ to calculate Gibbs free energy of the reaction (ΔG).

e.g. $CH_4(g) + aO_2(g) \rightarrow *Int + bH_2O(g)$ (Reaction 1)

Reaction 1 is the reaction equation of methane oxidation producing the adsorbed intermediate (Int) and H_2O (g) with O_2 (g) and CH_4 (g), where a and b are the coefficient of O_2 (g) and that of H_2O (g). Regarding the reaction of adsorbates with O_2 (g), the equilibrium constant (K_p) can be derived relating to Boltzmann distribution,

$$K_p = \frac{{P_{H_2O(g)}}^b}{P_{CH_4(g)}\,{P_{O_2(g)}}^a} = \exp\left(-\frac{\Delta}{k_B T}\right) \tag{4.1.4}$$

where $P_{H_2O(g)}$, $P_{O_2(g)}$, k_B, and T and represent the partial pressure of H_2O and O_2, Boltzmann constant, and temperature, which was set to 923 K in this work. Δ is Gibbs free energy difference, which can be written as,

$$\Delta = \Delta G_{Int^*} + b\,\mu_{H_2O(g)} - (\mu_{CH_4(g)} + a\,\mu_{O_2(g)}) \tag{4.1.5}$$

where ΔG_{Int^*} is related to Gibbs free energy of adsorption of intermediate. $\mu_{H_2O(g)}$, $\mu_{CH_4(g)}$, and $\mu_{O_2(g)}$ represent the chemical potential of H_2O (g), CH_4 (g) and O_2 (g), respectively, which can be obtained by,

$$\mu_A(T,P) = E_A^{DFT} + \mu_A^o(T,P_A^o) + k_B T ln\frac{P_A}{P_A^o} \tag{4.1.6}$$

where E_A^{DFT}, μ_A^o, and P_A are the total energy derived from DFT calculations, the standard chemical potential at the standard pressure P_A^o,[113] and the partial pressure of A at temperature T, respectively. ${P_{H_2O(g)}}^b$ in Eq (4.1.7) can be written as,

$${P_{H_2O(g)}}^b = P_{CH_4(g)}\,{P_{O_2(g)}}^a \exp\left(-\frac{\Delta}{kT}\right) \tag{4.1.7}$$

We can derive the equation relating Δ to $P_{H_2O(g)}$. Δ_0 is related to the difference of Gibbs free energy when $P_{H_2O(g)}$ is 1 atm and can be presented by,

$$\Delta_0 = \Delta G_{Int^*} + b\mu_{H_2O(g)}^o - (\mu_{CH_4(g)} + a\,\mu_{O_2(g)}) \tag{4.1.8}$$

$\mu_{H_2O(g)}^o$ is the chemical potential of H_2O at the standard states. Accordingly, Δ in Eq (4.1.5) and Δ_0 in Eq (4.1.8) can be written as using Eq (4.1.7),

$$\Delta = \Delta G_{Int^*} + b(E_{DFT}^{H_2O} + \mu^o(T,P^o) + k_B T ln P_{H_2O(g)}) - (\mu_{CH_4(g)} + a\,\mu_{O_2(g)}) \tag{4.1.9}$$

and

$$\Delta_0 = \Delta G_{Int^*} + b(E_{DFT}^{H_2O} + \mu^o(T,P^o)) - (\mu_{CH_4(g)} + a\,\mu_{O_2(g)}) \tag{4.1.10}$$

Thus, the difference between Δ and Δ_0 can be given by,

$$\Delta - \Delta_0 = b k_B T ln P_{H_2O(g)} \tag{4.1.11}$$

Δ can be expressed as,

$$\Delta = \Delta_0 + bk_BTlnP_{H_2O(g)} \quad (4.1.12)$$

Δ in Eq (4.1.7) can be substituted for Δ in Eq (4.1.12), accordingly, ${P_{H_2O(g)}}^b$ can be represented,

$${P_{H_2O(g)}}^b = P_{CH_4(g)}\,{P_{O_2(g)}}^a \exp\left(-\frac{\Delta_0 + bk_BTlnP_{H_2O(g)}}{k_BT}\right) \quad (4.1.13)$$

And ${P_{H_2O(g)}}^b$ can be rewritten as,

$${P_{H_2O(g)}}^b = {P_{O_2(g)}}^{\frac{1}{4}} \exp\left(-\frac{\Delta_0}{k_BT}\right)\exp\left(-blnP_{H_2O(g)}\right) \quad (4.1.14)$$

Thus, $P_{H_2O(g)}$ for the Reaction 1 is,

$$P_{H_2O(g)} = \left[P_{CH_4(g)}{P_{O_2(g)}}^a \exp\left(-\frac{\Delta_0}{k_BT}\right)\right]^{\frac{1}{2b}} \quad (4.1.15)$$

Given that CH_4 (g) and O_2 (g) are introduced into the chamber first, it was assumed that the active sites on CeO_2 surface were taken by reaction intermediates and oxygen competitively. Accordingly, at first the adsorption energies of *CH_4 and *O were calculated to check whether the reactants contribute to the reaction as a gas phase itself or adsorbed phase on the surface. The pressures of CH_4 (g) and O_2 (g) are set to 0.2 Torr (≈ 0.00026 atm) and 1 Torr (≈ 0.0013 atm) in this work, which is the reaction condition from the literature.[81] To calculate the adsorption energy of CH_4 (g) and O_2 (g), the chemical potentials of gas phase molecules A were obtained by using the following equation,

$$\mu_A(T,P) = E_A^{DFT} + \mu_A^o(T,P_A^o) + k_BTln\frac{P_A}{P_A^o} \quad (4.1.16)$$

where E_A^{DFT}, μ_A^o, and P_A in Eq (4.1.16) are the total energy derived from DFT calculations, the standard chemical potential at the standard pressure P_A^o,[113] and the partial pressure of gas-phase *A* molecules A at temperature T, respectively.

4.1.2.4 Correction energy term: The effect of periodicity of supercell on the adsorption energy calculations

The formation energies of finite-size supercells with charged defects to calculate the Gibbs free adsorption energy were additionally considered in this work. In general, DFT calculations for solids are performed using periodic boundary conditions to model the periodicity and bulk properties of materials because atoms in materials are arranged in a repeating lattice. Periodic boundary conditions enable us to perform DFT calculations by treating the system as infinite with a small unit cell with minimal computational effort. To precisely calculate the free energy

of charged adsorbates, this work adopts the correction scheme developed for the formation energies calculations of charged defect.[114,115] In that context, a charged finite cell is simulated by artificially introducing a compensating uniform background charge ("jellium background") to avoid the divergence in the electrostatic energy. The formation energy of the charged slab significantly depends on the supercell, especially on the vacuum thickness and charged states. Therefore, the formation energy will contain a non-negligible error without correction.[114] To eliminate the error for the precise calculations, the formation energies of finite-size supercells with charged defects were corrected by adding slab-based correction term (E_{corr})[115,116] to Eq (4.1.4) as given by:

$$E_{corr} = E_{iso} - E_{per} + q\Delta V \quad (4.1.17)$$

where E_{iso} is self-interaction of the isolated charge distribution; the energy of the model charge embedded in an infinite dielectric medium. E_{per} is the energy of the model charge embedded in the model dielectric medium under periodic boundary conditions; both the self-interaction and the interaction with the periodic images and the background charge. ΔV is the difference between the potential of the model charge system and DFT calculations. The correction term (E_{corr}) is assessed at two distinct vacuum thicknesses (10 and 25 Å). Subsequently, the corrected energies for charged adsorbates (E_{corr}) were validated by their substantial concordance (i.e., within 20 meV difference). The calculated values of corrected energy terms are presented in Table 4.1.1.

Table 4.1.1 The uncorrected and corrected energetics for charged adsorbates across varying vacuum thicknesses.

species	$E_{\mathrm{uncorr}} = \Delta E_0 + q(E_{VBM})$ [eV]		$E_{\mathrm{corr}} = E_{\mathrm{uncorr}} + E_{iso} - E_{per} + q\Delta V$ [eV]	
	Vacuum 10 Å	Vacuum 25 Å	Vacuum 10 Å	Vacuum 25 Å
$^{*}CH_3^+$	-2.89	-2.39	-3.07	-3.06
$^{*}CH_2^+$	1.70	2.19	1.56	1.56
$^{*}CH^+$	6.78	7.31	6.63	6.62
$^{*}CH_3^-$	4.41	4.87	4.33	4.34
$^{*}CH_2^-$	6.00	6.47	5.80	5.80
$^{*}CH^-$	5.31	5.79	5.11	5.11

Consequently, the Gibbs free energy equation, including the correction energy term as a function of Fermi level, can be calculated by using Eq (4.1.18):

$$\Delta G_{ads} = \Delta E_0 + \Delta ZPE + \int C_p dT - T\Delta S + q(\varepsilon_F + E_{VBM}) + E_{iso} - E_{per} + q\Delta V \quad (4.1.18)$$

where ΔE_0 in Eq (4.1.18) is the binding energy of adsorbates on CeO_2. q, ε_F and E_{VBM} in Eq (4.1.18) are the possible charge states of the adsorbates due to charge transfer, the Fermi level that ranges over the band gap of CeO_2 (111), and the DFT-computed eigenvalue of the VBM energy level of the CeO_2 (111) slab with the adsorbate, respectively.[31,44,104]

4.1.3 Results and Discussion

4.1.3.1 Fermi level-dependent reaction pathway and energy barrier

In this work, the methane oxidation reaction at a typical SOFCs operating temperature of 923 K (650 °C) was considered for the reaction intermediates free energy calculations.[117] The equilibrium of total methane oxidation is presented as,

$$CH_4\ (g) + 2O_2\ (g) \rightleftarrows CO_2\ (g) + 2H_2O\ (g)$$

There are two representative surface-catalyzed reaction mechanisms in heterogeneous catalysis: the Langmuir-Hinshelwood (LH) mechanism and the Eley-Rideal (ER) mechanism. In the LH mechanism, both reactants are first adsorbed on the surface, and the surface reaction occurs between these adsorbed species.[9] On the other hand, in the EF mechanism, one reactant is adsorbed on the surface first, then the other reactant in the gas phase reacts with the adsorbed species. Since O_2 can either adsorb on the catalyst surface to generate reactive oxygen species (*O) or directly participate in the reaction in its molecular form, both LH type and ER type reaction pathways were considered. In the former case, CH_4 interacts with pre-adsorbed oxygen species (*O), while in the latter, gas-phase O_2 directly reacts with surface intermediates. Accordingly, the first reaction step involves the interaction between CH_4 and O, leading to $*CH_3$ formation, and thus the adsorption energies of $*CH_4$ and *O were calculated.

Considering the adsorption of CH_4 molecule on the CeO_2 surface for the initiation of methane oxidation, it is not energetically favored, showing the positive value of the adsorption energy (2.75 eV) as shown in Figure 4.1.3. On the other hand, Gibbs free adsorption energy becomes negative as the Fermi level of CeO_2 increases. Especially, *O with -2 charge ($*O^{2-}$) showed the negative value of adsorption energy when the Fermi level of CeO_2 is above 1.58 eV, indicating that $*O^{2-}$ competes with the adsorbates of the first reaction step ($*CH_3$

formation). Therefore, the methane oxidation reactant oxygen reservoir is O_2 (g) ($*O^{2-}$) with the Fermi level below (above) 1.58 eV.

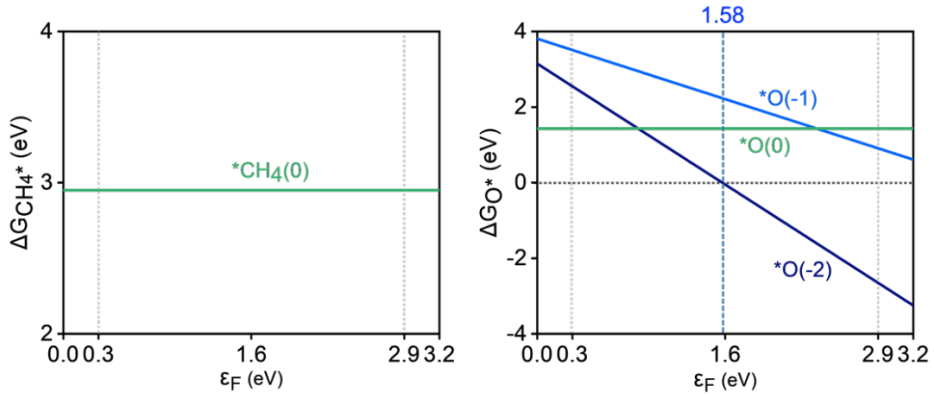

Figure 4.1.3 The graph of Gibbs free adsorption energy of $*CH_4$ and *O, respectively.

In this regard, the two main reactions of methane oxidation with O_2 (g) or *O should be considered as follows:

(1) Methane oxidation with O_2 (g) (ER mechanism type reaction pathway)

(i) CH_4 (g) → $*CH_3$ → $*CH_2$ → *CH → *C → *CO → $*CO_2$ → CO_2 (g)

(ii) CH_4 (g) → $*CH_3$ → $*CH_2$ → *CH → *CHO → *CO → $*CO_2$ → CO_2 (g)

(iii) CH_4 (g) → $*CH_3$ → $*CH_2$ → *CH → *CHO → *OCHO → $*CO_2$ → CO_2 (g)

(2) Methane oxidation with O* in case that O* is adsorbed on the surface if the Fermi level of CeO_2 is higher than 1.58 eV (LH mechanism type reaction pathway)

CH_4 (g) → $*CH_2$ → *C → *CO → $*CO_2$ → CO_2 (g)

Consequently, the considered reaction pathways for methane oxidation are shown in Scheme 4.1.1:

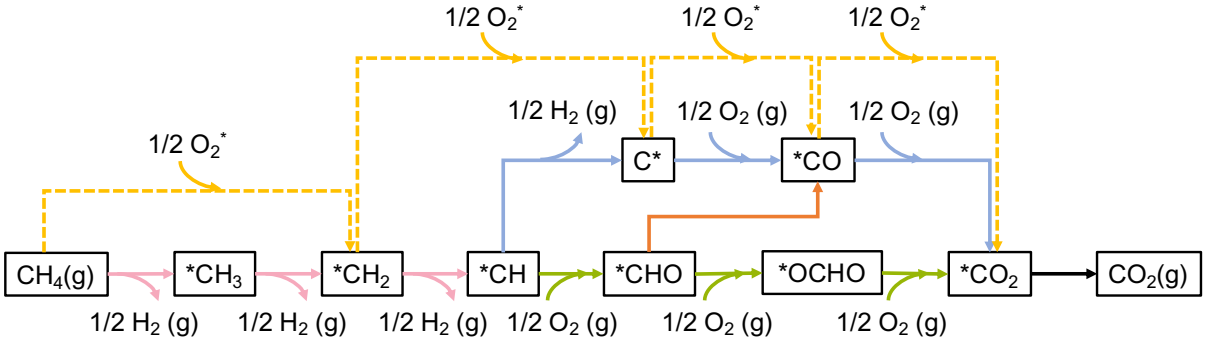

Scheme 4.1.1 The reaction pathways of methane oxidation. The asterisk (*) denotes an adsorbed species. The yellow dashed line is the pathway with O*. The solid lines (except the black solid line) correspond to pathways with O_2 (g): the pink lines indicate the primary pathway, while blue, orange, and green lines denote the *C-, *CHO-, and *OCHO-mediated pathways, respectively. The black solid represents the elementary step of CO_2 (g) formation.

The elementary reaction steps of methane oxidation with O_2 (g) are listed below,

$$CH_4\,(g) + \frac{1}{4}O_2\,(g) \rightarrow *CH_3 + \frac{1}{2}H_2O\,(g)$$

$$*CH_3 + \frac{1}{4}O_2\,(g) \rightarrow *CH_2 + \frac{1}{2}H_2O\,(g)$$

$$*CH_2 + \frac{1}{4}O_2\,(g) \rightarrow *CH + \frac{1}{2}H_2O\,(g)$$

$$*CH + \frac{1}{4}O_2\,(g) \rightarrow *C + \frac{1}{2}H_2O\,(g)$$

$$*CH + \frac{1}{2}O_2\,(g) \rightarrow *CHO$$

$$*C + \frac{1}{2}O_2\,(g) \rightarrow *CO$$

$$*CHO + \frac{1}{4}O_2\,(g) \rightarrow *CO + \frac{1}{2}H_2O\,(g)$$

$$*CHO + \frac{1}{2}O_2\,(g) \rightarrow *OCHO$$

$$*OCHO + \frac{1}{4}O_2\,(g) \rightarrow *CO_2 + \frac{1}{2}H_2O\,(g)$$

$$*CO + \frac{1}{2}O_2\,(g) \rightarrow *CO_2$$

$$*CO_2 \rightarrow CO_2\,(g) + *$$

For the methane oxidation with *O can be written below,

CH_4 (g) + *O → *CH_2 + H_2O (g)

*CH_2 + *O → *C + H_2O (g)

*C + *O → *CO + H_2O (g)

*CO + *O → *CO_2

*CO_2 → CO_2 (g) + *

Considering the charge transfer during chemisorption, the intermediates of methane oxidation can be charged. In this regard, charges of -1, 0, and +1 are considered for CH_3, CH, C, CHO, and OCHO; charges of -2, -1, 0, +1, and +2 are considered for CH_2; and only the neutral charge is considered for CO and CO_2 in the Gibbs free energy calculations. The detailed discussion of charge states of intermediates is described:

***CH_4:** only neutral CH_4 was considered because four valence electrons of C atom are bonded with four H atoms by sp^3 hybridization.

***CH_3:** two adsorption configurations were considered: vertical and horizontal. Because the horizontal adsorption configuration was thermodynamically more favored than the vertical configuration, the adsorption energies of horizontally adsorbed CH_3 were considered to calculate the Gibbs free energy. Since CH_3 has one radical in p orbital, +1, -1, and 0 charge states were considered. Neutral CH_3 was not adsorbed on the CeO_2 surface.

***CH_2:** CH_2 has one empty p orbital and one lone pair of electrons, thus, they can behave as an electron acceptor and donor. Accordingly, charge states of +2, +1, -1, and -2 were considered. +2 charged CH_2 (q = +2) was not adsorbed, because CH_2O molecule was formed with O atom from CeO_2 surface.

***CH:** CH has either one or three unpaired electrons, depending on the molecule's excitation state. Only one radical of CH with +1, 0, and -1 charge states were considered to calculate the adsorption energy.

***C:** The electron configuration of C is $1s^2 2s^2 2p^2$, in which C has two half-filled and one unoccupied 2p orbitals, so we considered +2, +1, and -1 charge states. C with charge state +2 was not adsorbed.

***CHO**: Since C has a radical, behaving electron donor or acceptor, +1, -1, and 0 were considered. CHO^+ with a linear molecular geometry was not adsorbed on the surface.

***OCHO:** O atom of OCHO has one radical and two lone pairs, thus, charge states of -1, +1, and 0 are considered.

***CO:** C and O atoms, which are bonded with triple bonds each other, obey the octet rule for both molecules. Therefore, only neutral CO was considered.

***CO_2:** C and two O atoms are bonded with double bonds, and each atom obeys the octet rule. Only neutral CO_2 was considered.

***O:** The electron configuration is $1s^2 2s^2 2p^4$ with one fully filled and two half-filled 2p orbitals, so the considered charge states are +1, -1, and -2. However, the adsorption of *O charged with +1 was found to be highly unstable.

The optimized configurations of adsorbates are shown in Figure 4.1.4.

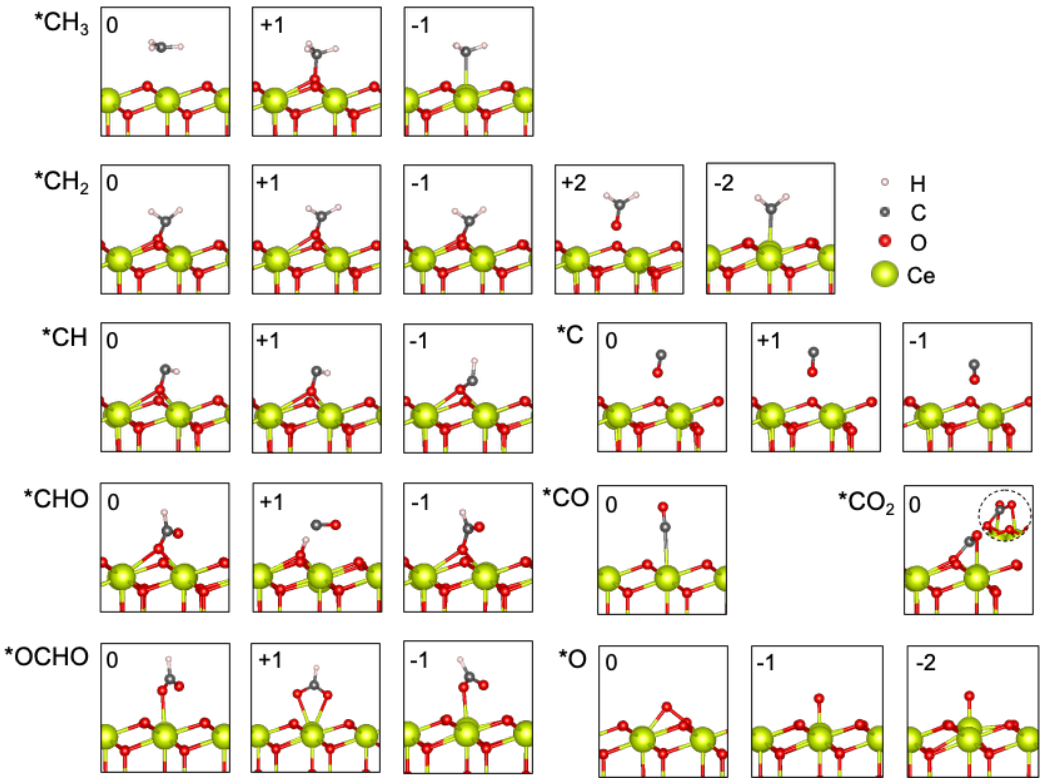

Figure 4.1.4 The optimized configurations of adsorbates. The numbers inside the boxes represent the charge state of adsorbates, q.

Figure 4.1.4 shows that *CH_3 (q = 0), CH_2 (q = +2), C (q = -1, 0, +1), and CHO (q = +1) were not adsorbed on the surface. Therefore, these adsorbates were not considered as an intermediate of methane oxidation on CeO_2 (111) in this work. The graphs of Gibbs free energy of methane oxidation on CeO_2 with all possible (adsorbed) intermediates were depicted in Figure 4.1.5.

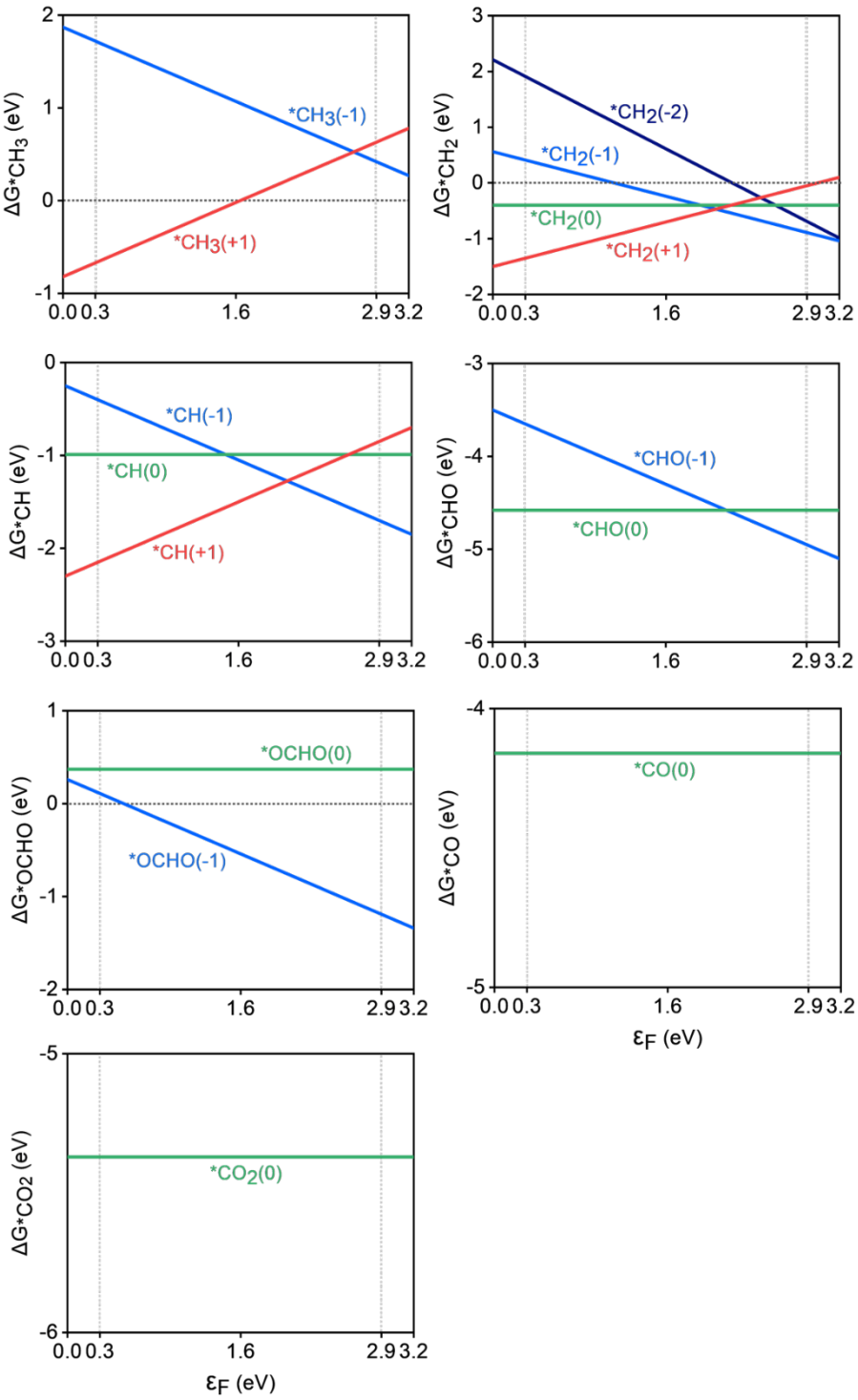

Figure 4.1.5 The graph of Gibbs free adsorption energy of the reaction.

The charge density difference ($\Delta\rho$) between CeO_2 and adsorbed intermediates was calculated to qualitatively visualize the localization of the excessive charges using the following equation,

$$\Delta\rho = \Delta\rho_{slab/charged\ adsobate} - \Delta\rho_{slab/adsobate} \quad (4.1.19)$$

where $\Delta\rho_{slab/charged\ adsobate}$ and $\Delta\rho_{slab/adsobate}$ are charge density of CeO_2 slab with adsorbed charged adsorbate and adsorbate without charge.

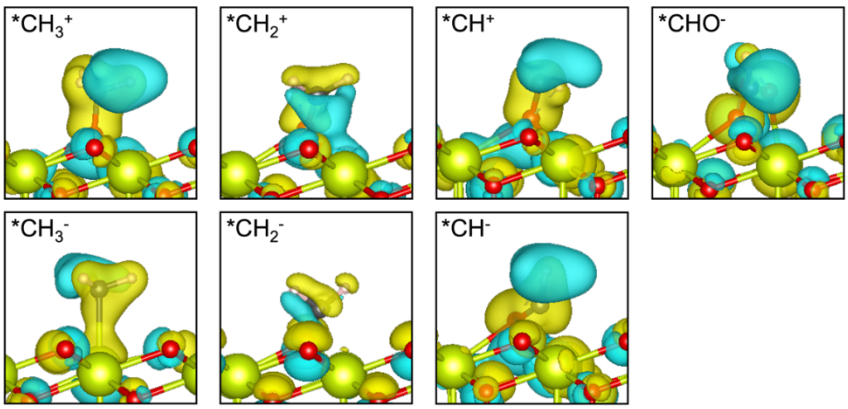

Figure 4.1.6 Charge density difference plots of CH_3, CH_2, CH, C, and CHO on a CeO_2 surface. The yellow and cyan blue regions denote the electron accumulation and depletion regions, respectively. The isovalue is 0.20 e/Bohr.

This difference represents the redistribution of electrons upon charging, highlighting regions where the excessive charges are localized. Figure 4.1.6 shows that all the excessive charges in the models were localized on intermediates on the CeO_2 surface. Since this indicates the charges are transferred between adsorbates and CeO_2, it is reasonable to apply the Fermi level dependency of the adsorption energy theory model.

4.1.3.2 Fermi level dependent reaction pathway and energy barrier

The free energy diagrams of the methane oxidation reactions by neutral (ε_F = 1.6 eV), heavily p-type (ε_F = 0.3 eV), and n-type (ε_F = 2.9 eV) CeO_2 with the thermodynamically preferred intermediates and the atomic structure of each reaction step are presented in Figure 4.1.7 to examine whether Fermi level can affect reaction pathway and energy barriers.

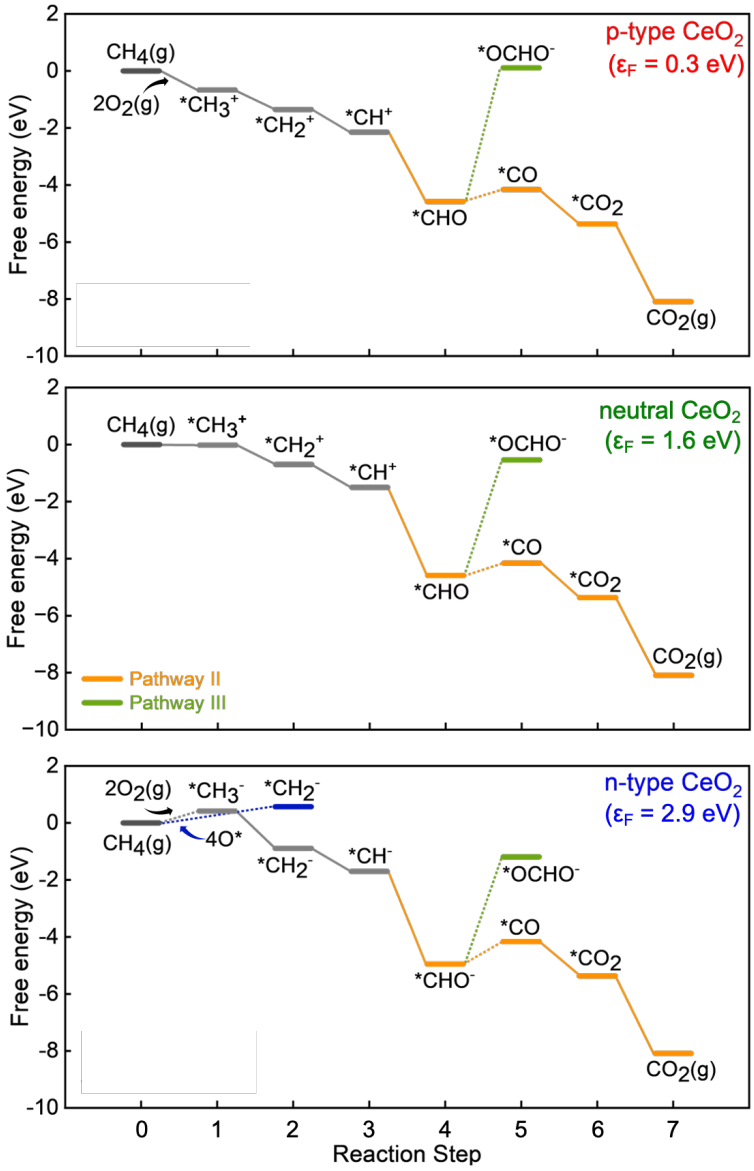

Figure 4.1.7 The free energy diagrams of methane oxidation on heavily p-type, neutral and heavily n-type CeO_2 with all possible intermediates.

The detailed free energy diagrams of methane oxidation on heavily p-type, neutral, and heavily n-type CeO_2 with all possible intermediates are depicted in Figure 4.1.7. The results indicate that the charge state of *CH_3 in reaction step 1 is positive (CH_3^+) on p-type (ε_F = 0.3

eV), neutral (ε_F = 1.6 eV) CeO_2, and turns negative (CH_3^-) on n-type (ε_F = 2.9 eV) CeO_2. Given that adsorbed $*O^{2-}$ is stabilized on n-type CeO_2 surface due to stronger binding to surface Ce ions, the formation of $*CH_3^-$ is suppressed.

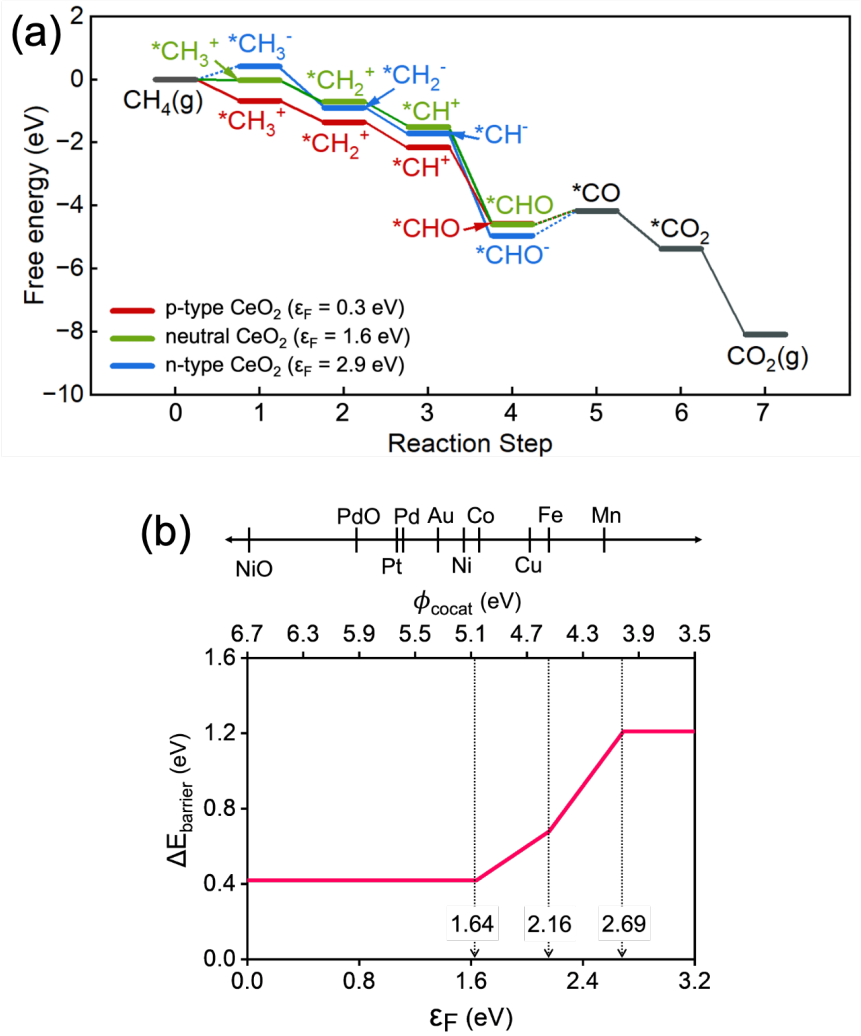

Figure 4.1.8 DFT Calculations of methane oxidation on a CeO_2 (111) surface with Fermi level variation (a) Calculated free energy diagrams and (b) the atomic structures of the methane oxidation reaction pathways of methane oxidation on the p-type (ε_F = 0.3 eV), neutral (ε_F = 1.6 eV), and the n-type (ε_F = 2.9 eV) CeO_2. Black lines in (a) indicate the energy levels in the reaction steps 5-7 in the methane oxidation, which is the same regardless of the Fermi level of CeO_2. Solid and dashed lines in (a) indicate the energy downhill and uphill reactions, respectively.

In Figure 4.1.8 (a), we can see that dehydrogenation reactions are all thermodynamically favorable from the reaction step 2 to 4, regardless of the surface Fermi level position of CeO_2. The theoretical prediction of energy downhills for reaction steps 2 to 4 is consistent well with

the experimental in situ observations on CeO_2 catalysts, that the CH_2 group was not detected due to its very short lifetime.[99] For reaction step 4, it is predicted that *C adsorption on CeO_2 is not thermodynamically stable. (Figure 4.1.4) Instead, *CHO formation is favored with charge neutral (q = 0) on p-type CeO_2 and negative charge (q = -1) on n-type CeO_2. Since the adsorption energy of $*CHO^-$ becomes more negative with increasing Fermi level of CeO_2, the energy uphill in the reaction step 5 becomes larger with the CeO_2 surface Fermi level. The formation of $*CHO^-$ adsorbate on CeO_2 catalyst surfaces during methane oxidation reactions are in accordance with the experimental observations of significant stretching vibration frequencies of CHO^- groups at 1735, 1715, and 1704 cm^{-1}.[118,119] Furthermore, $*CO_2$ adsorption and CO_2 (g) formation are expected to proceed spontaneously, indicating that these processes are thermodynamically favorable. To summarize, the endothermic steps of methane oxidation on CeO_2 (111) were identified as reaction step 1 ($*CH_3$ formation) and reaction step 5 (*CO formation from *CHO).

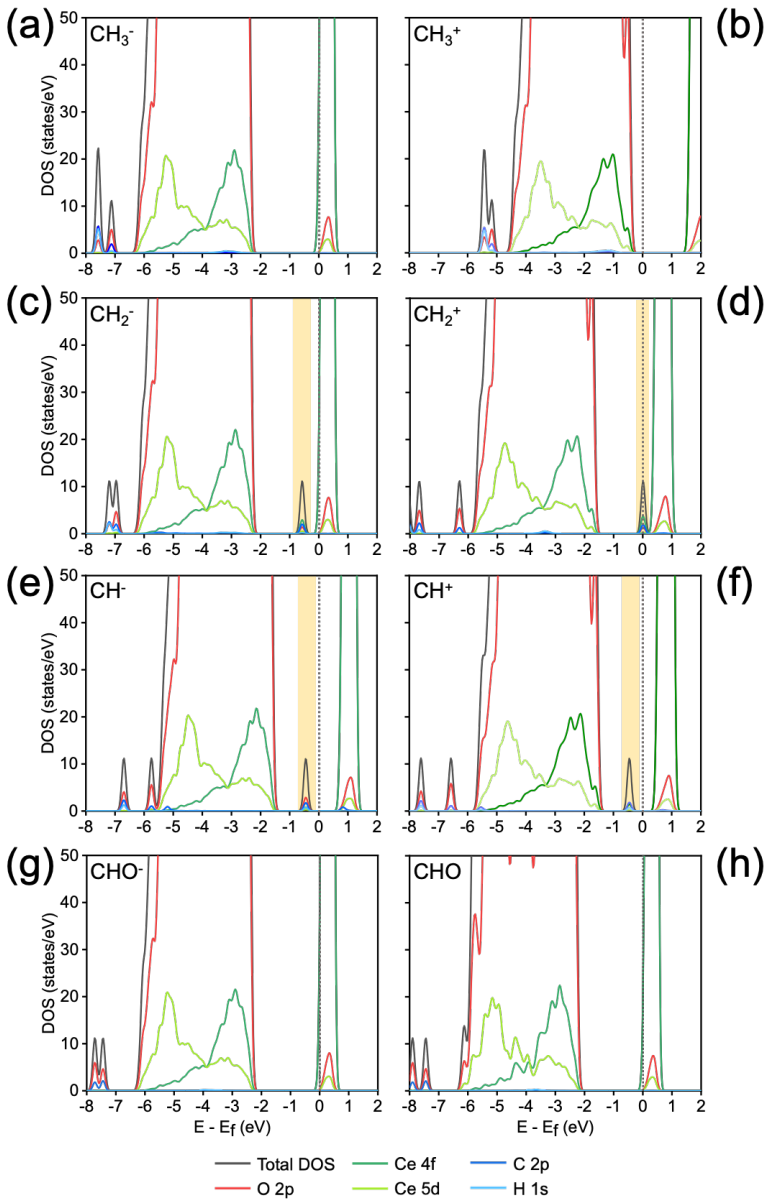

Figure 4.1.9 Density of states (DOS) of (a) CH_3^- (b) CH_3^+ (c) CH_2^- (d) CH_2^+ (e) CH^- (f) CH^+ (g) CHO^- and (h) CHO intermediates. The highlighted yellow region in (c) – (f) corresponds to the mid-gap states.

To see the change in the electronic states of CeO_2 during methane oxidation, the density of states (DOS) of each charged intermediate (CH_3, CH_2, CH, and CHO) was calculated as shown in Figure 4.1.9. In the DOS plots, the valence band maximum (VBM) and conduction band minimum (CBM) are mainly derived from O 2p (red line) and Ce 5d states (light green line), respectively. The existence of mid-gap states between these two bands indicates strong binding between adsorbates and surface. Figure 4.1.9 (c) – (f) show that the adsorption of both negatively and positively charged CH_2 and CH resulted in the formation of mid-gap states, while there is no mid-gap state formation by CH_3 and CHO adsorption (Figure 4.1.9 (a, b, g,

h). According to the calculated free energy diagram in Figure 4.1.8 (a), CH_2 and CH are not expected to remain residually bound to the CeO_2 surface but rather proceed to CHO formation, showing the free energy downhill in reaction step 4. Therefore, the mid-gap states generated by CH_2 and CH adsorption have a negligible influence on the surface Fermi level position.

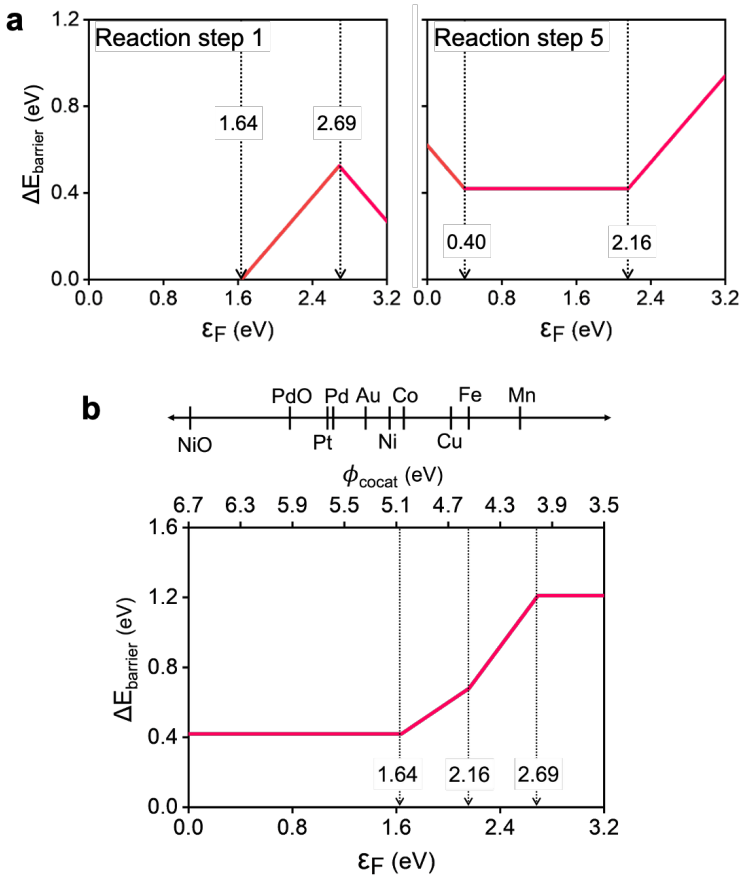

Figure 4.1.10 The graphs of (a) the energy barrier of reaction step 1 and reaction 5 as a function of the Fermi level of CeO_2 (b) total energy barrier as a function of Fermi level of CeO_2 and cocatalyst work function.

To give quantitative insight, the energy barrier of the endothermic reaction steps 1 and 5 is plotted in Figure 4.1.10 (a). The reaction steps showing the energy barrier within a specific Fermi level range are presented as follows,

The reaction step 1:

$$CH_4(g) + ¼O_2 \rightarrow *CH_3^+ + ½H_2O\ (g)\ (1.64 \leq \varepsilon_F\ (eV) < 2.69)$$

$$CH_4(g) + ¼O_2 \rightarrow *CH_3^- + ½H_2O\ (g)\ (2.69 \leq \varepsilon_F\ (eV))$$

The reaction step 5:

$$*CHO + ¼O_2 \rightarrow *CO + ½H_2O(g)\ (\varepsilon_F\ (eV) < 2.16)$$

$$*CHO^- + ¼O_2 \rightarrow *CO + ½H_2O(g)\ (2.16 \leq \varepsilon_F\ (eV))$$

The graph of total energy barrier with respect to the surface Fermi level of CeO_2 (ε_F) is plotted by the summation of the energy barriers of the endothermic reaction steps for methane oxidation on CeO_2 as shown in Figure 4.1.10 (b). It indicates that the minimum total energy barrier to methane oxidation is 0.42 eV when the Fermi level of CeO_2 ranges from 0 eV to 1.64 eV. Now, we can conclude that the Fermi level of CeO_2 should be controlled in the following ways to enhance the reactivity of methane oxidation on CeO_2: (i) hindering the strong adsorption of the O atom, so that $*CH_3$ can dominantly occupy the active site of CeO_2 and (ii) the total energy barrier including two endothermic reaction steps for the $*CH_3$ and *CO formations should be minimized.

General methods to control the surface Fermi level of a wide band gap semiconductor include (i) impurity doping,[120] (ii) grain size control,[121] and (iii) depositions of other NP on the surface.[122] However, it is extremely challenging to lower the Fermi level of CeO_2 via impurity doping or grain size control because even metal dopants having smaller valence preserve the intrinsic n-type characteristic of CeO_2, as the dopants are segregated at grain boundaries.[93,94] Such size effects on surface band bending are only relevant when the grain radius is smaller than the charge depletion region width (< 30 nm).[121] Since the grains in most of CeO_2 catalysts, including those studied here, are typically larger than 50 nm,[86,90,123] this mechanism can be excluded. As a result, the modulation of the surface electronic structure was the only approach in this work. To evaluate the feasibility of modifying the CeO_2 surface via cocatalyst deposition, cocatalyst candidates previously reported as cocatalysts or dopants for CeO_2 were chosen from the literature. The theoretical prediction that cocatalysts having work functions between 5.06 eV and 6.70 eV to adjust the Fermi level of CeO_2 is consistent with many experimental evidences such as CeO_2 decorated with Ni,[99,123,124] Pt,[125,126] Pd,[79,90,127] and Au.[100]

4.1.3.3 Analytical models for the combinational effect of cocatalyst dispersion and work function

When a cocatalyst is deposited on a semiconductor surface, the work function difference induces charge redistribution at the interface, resulting in band bending. Consequently, the electrostatic potential—and thereby the band edge positions—on the semiconductor side exhibit a quadratic variation. Then, accordingly, the reaction energy barriers and the resultant reaction rate are also changed with the radial distance of the interface between cocatalyst NP and the semiconductor (Figure 4.1.10 (b)).

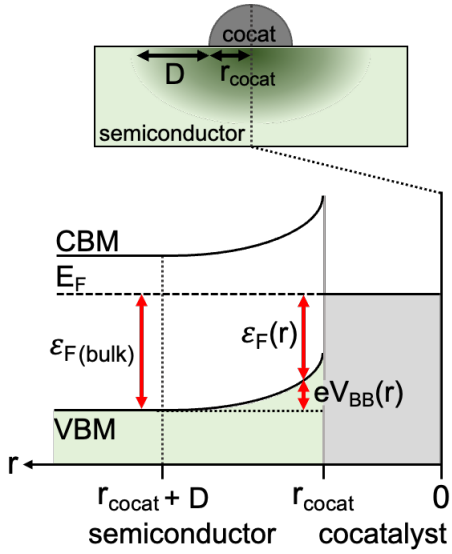

Figure 4.1.11 A schematic explanation of the analytical model for the prediction of the catalytic activity of cocatalyst-loaded CeO_2 to calculate the surface reaction rate.

In addition, there are several factors affecting the catalytic activity of wide band gap semiconductors such as nonstoichiometry of host semiconductor materials, doping concentration, cocatalyst species, cocatalyst geometry, and surface coverage of cocatalyst. However, it is very challenging to account for multiple factors simultaneously to predict the catalytic activity. Hence, in order to make an accurate prediction in the overall reaction rate, it is necessary to utilize analytical models integrating the changes in the reaction rates with distance from the cocatalyst.

The analytical model was built for the precise prediction in the reaction rates for methane oxidation of cocatalyst-decorated CeO_2. Given that the work functions of predicted cocatalyst candidates are larger than that of CeO_2, Schottky contact between a cocatalyst NP and CeO_2

was considered as shown in Figure 4.1.11. In reality, the interfacial structure between the metal cocatalyst and CeO_2 is not always an ideal Schottky contact. Under oxidative reaction conditions, the cocatalyst can undergo partial oxidation, leading to the formation of an interfacial oxide layer. This layer modulates the effective distance between the cocatalyst nanoparticle and CeO_2, thereby influencing the Schottky barrier properties and charge transfer pathways. As aforementioned, the deposited cocatalyst NP on CeO_2 is smaller than the CeO_2 nanoparticle, we can assume that the work function of cocatalyst NP is aligned with the Fermi level of CeO_2 because the amount of electrons that cocatalyst NP can donate is not enough to adjust Fermi level of CeO_2. In the cocatalyst-CeO_2 junction, the surface Fermi level ($\varepsilon_F(r)$) and the degree of band bending ($V_{BB}(r)$) varies with the distance from the loaded cocatalyst (r), which is presented by the following equation:

$$\varepsilon_F(r) = \varepsilon_{F(CeO_2)} - \mathrm{e}V_{BB}(r) \tag{4.1.20}$$

The contact potential ($V_{BB}(r_{cocat})$) at the interface when r is the radius of a cocatalyst (r_{cocat}) is given by:

$$V_{BB}(r_{cocat}) = (\phi_{cocat} - \phi_{semi})/e \tag{4.1.21}$$

where ϕ_{cocat} and ϕ_{semi} are the work function of a cocatalyst and semiconductor (ϕ_{semi}), respectively.

With the consideration of the Fermi level-dependent adsorption energy theory model and the change in the reaction rate with distance from the cocatalysts (r), we can assume that the band bending is induced near the cocatalyst/CeO_2 interface in a radial direction from the center of a cocatalyst. In general, the cocatalyst NPs with a diameter of 1 – 10 nm are deposited on a CeO_2 surface;[122] a model of a hemispherical cocatalyst NPs on a semiconductor surface featuring a finite interface was employed to calculate the surface reaction rate with a consideration of the Fermi level change by the band bending near the interface of cocatalyst NPs and CeO_2. The mathematical model of a partially embedded spherical cocatalyst NP in a semiconductor with a finite interface was employed by editing an embedded spherical cocatalyst NP/a semiconductor model, which was proposed by Ioannides and Verykios.[122] Accordingly, the Poisson equation in the three-dimensional form must be employed for a finite interface between a metal NP with a small size and a semiconductor instead of the one-dimensional form for an infinite cocatalyst/semiconductor interface model.[39,122]

$$\nabla^2 V_{BB}(x, y, z) = -\frac{\rho}{\varepsilon_r \varepsilon_0} = -\frac{\rho}{\varepsilon} \tag{4.1.22}$$

where ρ, ε_r, and ε_0 in Eq (4.1.22) present the space charge density, the relative dielectric constant of CeO_2, which is 23, and the vacuum permittivity ($8.854\times 10^{-12} C\cdot V^{-1}m^{-1}$), respectively. $\varepsilon_r\varepsilon_0$ is the permittivity of the medium and is denoted by ε. The electric field ($E(r)$) within the depletion region ($r_{cocat} \leq$ r $\leq r_{cocat}+D$, D is the depletion layer thickness) between a hemispherical cocatalyst and a semiconductor (3D) can be,

$$E(r) = \frac{eN_d}{3\varepsilon r^2}((r_{cocat}+D)^3 - r^3) \ (r_{cocat} \leq r \leq r_{cocat}+D) \tag{4.1.23}$$

where N_d is the space charge density and D is the width of a depletion region. Accordingly, the electric potential (V_{BB}) can be obtained as follows:

$$V_{BB}(r) = \frac{eN_d}{\varepsilon}\left(\frac{D^2}{2} - \frac{r^2}{6} - \frac{D^3}{3r}\right) \ (r_{cocat} \leq r \leq r_{cocat}+D) \tag{4.1.24}$$

$$V_{BB} = 0 \ (r > r_{cocat}+D) \tag{4.1.25}$$

The band bending magnitude induced by the work function difference between a cocatalyst and CeO_2 can be expressed, as derived from Poisson equation in the three-dimensional form for a spherical coordinate can be written as:

$$V_{BB}(r) = \frac{eN_d}{\varepsilon_r\varepsilon_0}\left[\frac{(D+r_{cocat})^2}{2} - \frac{r^2}{6} - \frac{(D+r_{cocat})^3}{3r}\right] \tag{4.1.26}$$

Using the fixed value of r to r_{cocat}, we can obtain the width of the depletion region (D) by using Eq (4.1.27),

$$V_{BB}(r_{cocat}) = \phi_{cocat} - \phi_S = \frac{eN_d}{\varepsilon_r\varepsilon_0}\left[\frac{(D+r_{cocat})^2}{2} - \frac{r_{cocat}^2}{6} - \frac{(D+r_{cocat})^3}{3r_{cocat}}\right] \tag{4.1.27}$$

The equation of reaction rate constant (R) can be employed to compare the surface reaction activity of cocatalyst/CeO_2 and bare CeO_2 for methane oxidation, which can be written as:[9]

$$R = A\exp\left(-\frac{\Delta E_{barrier}}{kT}\right) \tag{4.1.28}$$

where A is the frequency factor, i.e., the number of attempts to react by vibrations, and $\Delta E_{barrier}$ is related to the total energy barrier that we calculated, respectively. To compare the reaction rate with/without cocatalysts on CeO_2, it is expressed the surface reaction rate constant ratio (R_1/R_0) where R_1 and R_0 are the surface reaction rate constants of methane oxidation on CeO_2 with/without cocatalyst at the induced band bending area (Dark green-color area in Figure 4.1.11 as follows:

$$\frac{R_1}{R_0} = \gamma\int_{r_{cocat}}^{r_{cocat}+D}\frac{\theta_{ads}^1}{\theta_{ads}^0}\exp\left(\frac{\Delta E_{barrier}^0 - \Delta E_{barrier}^1}{kT}\right)2\pi r\,dr \tag{4.1.29}$$

where θ_{ads} in Eq (4.1.29) is the coverage of adsorbates.

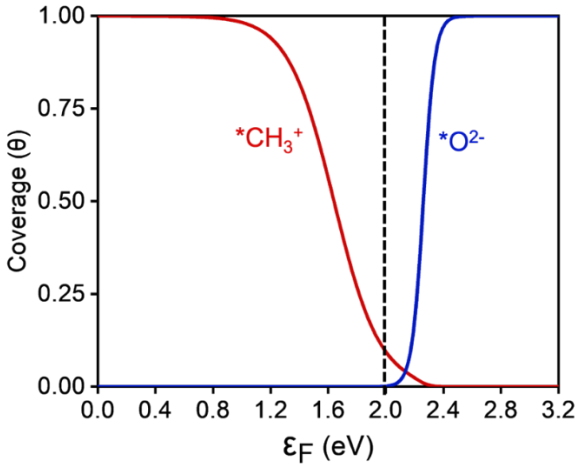

Figure 4.1.12 The graph of the coverage of *CH_3 and *O as a function of Fermi level. The coverage of *CH_3 for θ_{ads} term was considered because *CH_3 is a key intermediate to initiate methane oxidation with O_2 (g) in the first reaction step. This process competes with *O^{2-} adsorption. As the Fermi level of CeO_2 increases, the coverage of *CH_3 decreases, while *O^{2-} occupies most of the active sites.

The graph in Figure 4.1.12 was obtained by using the following equations:

$$\theta_{*CH_3} = \frac{e^{-\frac{\Delta G_{*CH_3}}{kT}}}{1 + e^{-\frac{\Delta G_{*O}}{kT}} + e^{-\frac{\Delta G_{*CH_3}}{kT}}} \tag{4.1.30}$$

$$\theta_{*O} = \frac{e^{-\frac{\Delta G_{*O}}{kT}}}{1 + e^{-\frac{\Delta G_{*O}}{kT}} + e^{-\frac{\Delta G_{*CH_3}}{kT}}} \tag{4.1.31}$$

The graph of coverage of *CH_3 (θ_{*CH_3}) and *O (θ_{*O}) considering the competing reaction between *CH_3 and *O in the first reaction step is depicted in Figure 4.1.12.

Given that the functionality and selectivity of catalysts are governed by the coverage and dispersion of a cocatalyst on a semiconductor,[128,129] the effect of cocatalyst coverage and dispersion on the reaction rate was considered by γ term in Eq (4.1.29), which is the ratio of the active site on the CeO_2 surface and it can be presented by:

$$\gamma = 1 - \frac{{r_{cocat}}^2 \pi}{A_{semi}} \tag{4.1.32}$$

where A_{semi} can be rewritten as ${r_{av}}^2 \pi$ and r_{av} is half of the average distance between adjacent cocatalysts.

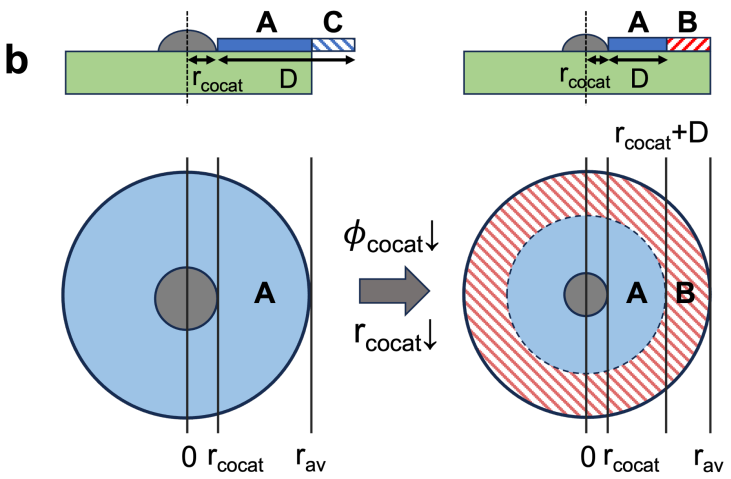

Figure 4.1.13 A schematic illustration of two cases of depletion region formation on the CeO_2 surface. The blue color area is the depletion region (band bending area, A), and the red color area is the area where the cocatalyst loading does not affect. (flat band area, B)

Figure 4.1.13 shows two cases of depletion region formation on a cocatalyst-loaded CeO_2 surface. If the band bending occurs at a broader area in the depletion region than half of the average distance between cocatalysts, the band bending area (blue color area A in Figure 4.1.13) can be distributed in all areas of the exposed CeO_2 surface, where the reaction ratio can be obtained using Eq (4.1.29) above. On the other hand, a flat band area (red-hatched area B in Figure 4.1.13) can exist on the CeO_2 surface when band bending occurs at a narrower area than half of the average distance between cocatalysts with a decrease in the work function and/or radius of a cocatalyst. The ratio of reaction rate constant on flat band area ranging from $r_{cocat} + D$ to r_{av} can be calculated using Eq (4.1.29). To simplify the calculation, the depletion region overlap area was ignored in this work.

In this regard, the contour maps of the surface reaction rate constant ratio (R_1/R_0) of a cocatalyst/CeO_2 (R_1) to that of bulk CeO_2 without a cocatalyst (R_0) as a function of the cocatalyst work function and the active sites ratio (γ) were calculated using Eq (4.1.33) and Eq (4.1.34):

i) $r_{cocat} + D$ is narrower than r_{av},

$$\frac{R_1}{R_0} = \gamma\left[\int_{r_{cocat}}^{r_{cocat}+D} \frac{\theta_{ads}^1}{\theta_{ads}^0} \exp\left(\frac{\Delta E_{barrier}^0 - \Delta E_{barrier}^1}{kT}\right) 2\pi r\, dr + \int_{r_{cocat}+D}^{r_{av}} \frac{\theta_{ads}^1}{\theta_{ads}^0} \exp\left(\frac{\Delta E_{barrier}^0 - \Delta E_{barrier}^1}{kT}\right) 2\pi r\, dr\right] \quad (4.1.33)$$

ii) $r_{cocat} + D$ is wider than r_{av},

$$\frac{R_1}{R_0} = \gamma \int_{r_{cocat}}^{r_{av}} \frac{\theta_{ads}^1}{\theta_{ads}^0} \exp\left(\frac{\Delta E_{barrier}^0 - \Delta E_{barrier}^1}{kT}\right) 2\pi r\, dr \quad (4.1.34)$$

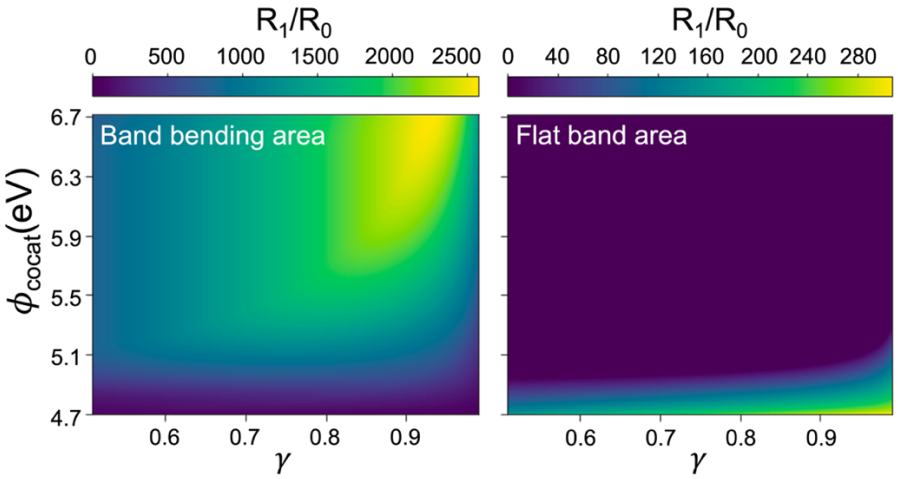

Figure 4.1.14 The contour map of surface reaction rate constant ratio (R_1/R_0) of a cocatalyst/CeO_2 (R_1) to that of bulk CeO_2 without a cocatalyst (R_0) of band bending area and flat band area ($N_d = 10^{19}$ cm^{-3}), respectively.

Figure 4.1.14 presents the contour map of surface reaction rate constant ratio of band bending area and flat band area when N_d is 10^{19} cm^{-3}. In previous studies, without the assumptions of the band bending dependency of methane oxidation reaction on CeO_2, cocatalyst coverage effects were not fully understood. The result in Figure 4.1.14 shows that the reaction rate of methane oxidation in the band bending area is approximately 9 times higher than that of the flat band area of CeO_2 for $N_d = 10^{19}$ cm^{-3}. It indicates that the considerations of cocatalyst dispersion (coverage) is a crucial factor due to the changed band bending and Fermi level positions with radial distance from a cocatalyst.

4.1.3.4 Optimum cocatalyst coverage and space charge density predictions

In most of the experimental works on cocatalyst-deposited CeO_2 catalysts, the methane oxidation reaction activities are sensitively changed with the combinations of many factors, such as cocatalyst species, dispersion distance, size, and impurity concentrations in CeO_2 supports.[86]

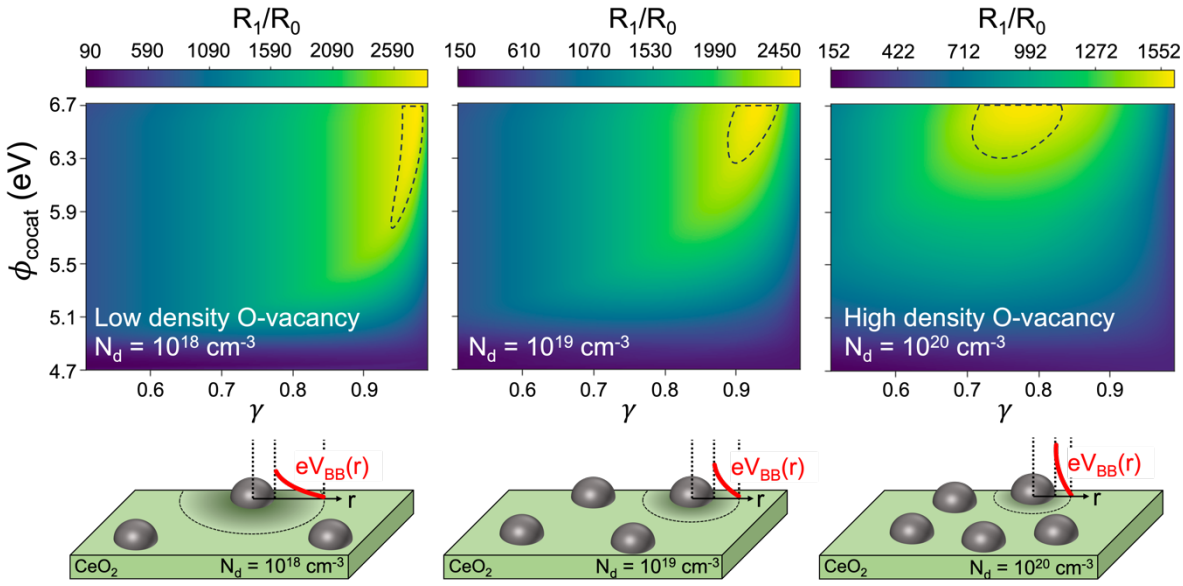

Figure 4.1.15 Top: the contour map of surface reaction rate ratio (R_1/R_0) of a cocatalyst/CeO_2 (R_1) to that of bulk CeO_2 without a cocatalyst (R_0) as a function of cocatalyst work function (ϕ_{cocat}) and the ratio of active sites (γ) with various space charge density (N_d) values. The areas enclosed by the dashed curves represent the reaction conditions for the high reactivity of methane oxidation. Bottom: Schematic illustration of the relation between N_d and the cocatalyst dispersion on CeO_2 by the changed band bending potential change at the interfaces (V_{BB}).

To further verify the hypothesis, Fermi level dependent methane oxidation reactions rate of CeO_2 catalyst, the ratio of the reaction rate is plotted by the use of a cocatalyst (R_1/R_0), with contour maps for the simultaneous variations of cocatalyst work function, coverage, and the nonstoichiometry of CeO_2 in Figure 4.1.15 using Eq (4.1.33) and Eq (4.1.34). The areas enclosed by the dashed curves in Figure 4.1.15 point the optimum cocatalyst deposition conditions for high catalytic activity of methane oxidation. For a high coverage of cocatalysts (lower γ value) with high work function for $N_d = 10^{19}\ cm^{-3}$ showed a lower reaction rate than that with the low coverage of cocatalysts (higher γ value). A number of previous experimental and theoretical studies have reported that the high coverage of a cocatalyst on CeO_2 can rather lower the catalytic activity.[80,84,130,131] For example, Lustemberg et al. reported that an undoped CeO_2 catalyst particle with low NiO coverage of 0.10 - 0.13 ML induces the

highest reaction rate of methane oxidation, which is in accordance with our theoretical observation in Figure 4.1.15 for $N_d = 10^{19} cm^{-3}$ (dashed circle at $0.87 < \gamma < 0.93$).[84] Considering the interface between the loaded catalyst and CeO_2 as the only area where the reaction dominantly takes place, Ni and NiO on CeO_2 were predicted to have total energy barrier (0.41 eV) for the whole methane oxidation. (Figure 4.1.10 (b)) However, with the analytical model, it can be reasoned that the different interface band bending of the Ni/CeO_2 and the NiO/CeO_2 systems will result in different overall reaction activity over the CeO_2 active site area.

The effects of oxidations of metal cocatalysts on the activity of methane oxidation reaction of CeO_2 catalyst have not been actively discussed before. Pd(0) and Ni(0) species deposited on CeO_2 catalysts surface are commonly oxidized and behave as the main active species by experimental works.[79,90,99,132] The methane oxidation reaction activity on CeO_2 catalyst is rather improved when the Pd and Ni particles.[90,132,133] The enhanced methane oxidation reaction activity of CeO_2 catalyst by the cocatalyst oxidation in the literatures[90,132,133] agree very well with the theoretical predictions in Figure 4.1.15: the higher reaction rate ratio of PdO/CeO_2 (work function 6.00 eV) than that of Pd/CeO_2 (work function 5.60 eV) and Pt/CeO_2 (work function 5.65 eV). With consideration that the work function of bimetallic catalysts has a linear trend with different compositions of bimetallic alloys,[134] bimetallic cocatalysts with CeO_2 can also be used by manipulation of metal composition to change the work function and thus depletion region width[135–138] such as the CuNi/CeO_2 catalyst reported by Hornes et al.[92] Many research works have already been devoted to studying the effect of oxygen vacancy formation in CeO_2 on the oxidation reaction.[82,83] Due to the unique property of Ce^{4+}/Ce^{3+} redox pair of CeO_2, the oxidation reaction on cocatalyst-decorated CeO_2 has been explained by MvK mechanism, in which lattice oxygen atoms of CeO_2 are involved in the oxidation reaction.[99,100,139,140] However, the underlying reaction mechanisms and active site are still controversial because the optimum cocatalyst coverage differs by species of cocatalyst, especially when Ce^{3+} species have high concentrations.[90,99]

The first few cycles of methane oxidation on CeO_2 can dominantly follow MvK mechanism. However, as methane oxidation takes place continuously, the formation energy of oxygen vacancies increases.[141,142] Accordingly, the contribution of MvK mechanism to the methane oxidation, where oxygen vacancy formation is involved, is rapidly decreased as the Fermi level increases. Therefore, it is insufficient to explain the long-term oxidation reaction by MvK mechanism alone. To precisely predict the reaction conditions of CeO_2 for even long-term methane oxidation, the synergistic effect of the formation of oxygen vacancies and the change

in band bending with increasing the surface Fermi level of CeO_2 on the reaction rate should be considered.

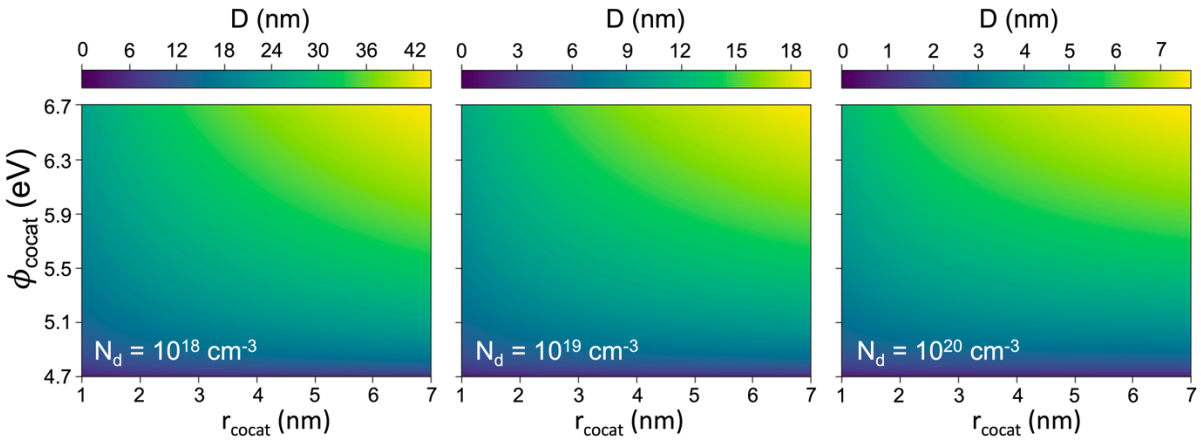

Figure 4.1.16 The graph of depletion region width as a function of a cocatalyst radius (r_{cocat}) and cocatalyst work function ($\emptyset_{cocat}$).

As the oxygen vacancy formation shifts the Fermi level of a CeO_2 higher, the surface band bending is induced at the narrower area in depletion region width as shown in Figure 4.1.16. Doping with Sm^{3+}, Eu^{3+}, or Zr^{4+} in Ni/CeO_2 increases the electron concentration (higher N_d value) by segregation at the grain boundary and oxygen vacancy formation. In addition, Ni NP tend to cluster within a few nanometers, which is much smaller than the depletion region width, thereby leading to a high cocatalyst coverage (lower γ value).[82,83,85] On the other hand, the distance of dispersed Ni NPs of undoped Ni/CeO_2 is wider (higher γ value) than that of heterovalent dopants doped CeO_2,[82] which is consistent with the calculations. Thus, the Fermi level dependency of adsorption energy theory model can provide further elucidation of the oxidation reaction on CeO_2, considering oxygen vacancy formation can change Fermi level to heavy n-type CeO_2, allowing us to understand the mechanism, including the long-term catalytic reaction.

4.1.4 Conclusion

In this work, methane oxidation on CeO_2 (Band gap (E_g), 3.2 eV) was used as the case model. The DFT calculation results showed that the surface Fermi level position of CeO_2 catalyst can alter the reaction energy barrier and also the reaction pathways, which can clearly explain why only a few specific cocatalyst elements, such as Ni, Pt, Pd and Au are used in most of the published reports. The combination of DFT calculations and a new analytical model was used to consider the band bending effects at the cocatalyst-CeO_2 interface to accurately predict the correlation between the methane oxidation reactivity of CeO_2 and the cocatalyst coverage. In addition, the combinatorial and synergistic effects of doping concentration, species of cocatalyst, and cocatalyst dispersion distance on CeO_2 catalyst on the methane oxidation reaction activity could be explained for many commonly observed phenomena. The newly suggested method of this work is expected to be widely used for efficient optimizations of doping concentration (Bulk Fermi level position) and cocatalyst materials, without suffering from the typical cell size limitations in atomic-scale modelling for DFT calculations on modified wide band gap semiconductor catalysts.

4.2 Photocatalysis: Incorporating Charge Carrier Contribution to the Theoretical Models for Photocatalytic Activity Prediction

As light-driven catalytic reactions have gained much attention, it has a high demand to precisely understand the underlying photocatalytic phenomena. Numerous research studies have been devoted to elucidating the theoretical photocatalytic reaction mechanisms. However, the complex reaction mechanisms, particularly those involving charge carriers, complicate its better understanding. In addition, since most photocatalysts are semiconducting materials, or even complex materials combining with semiconductors, it was necessary to develop a new theoretical framework to predict the reactivity of semiconductors, which was already solved by a new theoretical model introduced in Chapter 4.1.

Although charge carrier dynamics have been investigated in several theoretical works, the methodologies are insufficient to predict the overall catalytic reaction.[143,144] In this chapter, the "Fermi level-dependency of adsorption energy theory" will be expanded to photocatalysis by additionally accounting for the contribution of photoexcited charge carriers to the absorption phenomena.

4.2.1 Water Splitting Reaction

As renewable energy sources have been in significant demand because of fossil fuel depletion and climate change, water splitting has emerged as a promising approach for producing environmentally friendly H_2 generation.[145] The overall water-splitting consists of two half-reactions: i) the oxygen evolution reaction (OER) at the anode and ii) the hydrogen evolution reaction (HER) at the cathode. The overall water electrolysis reaction is:

$$2H_2O\ (l) \rightarrow O_2\ (g) + 2H_2\ (g)$$

which is a thermodynamically uphill process, requiring an energy input of 286 kJ mol^{-1} under standard conditions. Consequently, the minimum theoretical voltage needed to drive the reaction is 1.23 V.

There are three representative types of water splitting systems: electrochemical catalysis, photocatalysis, and photoelectrochemical catalysis.

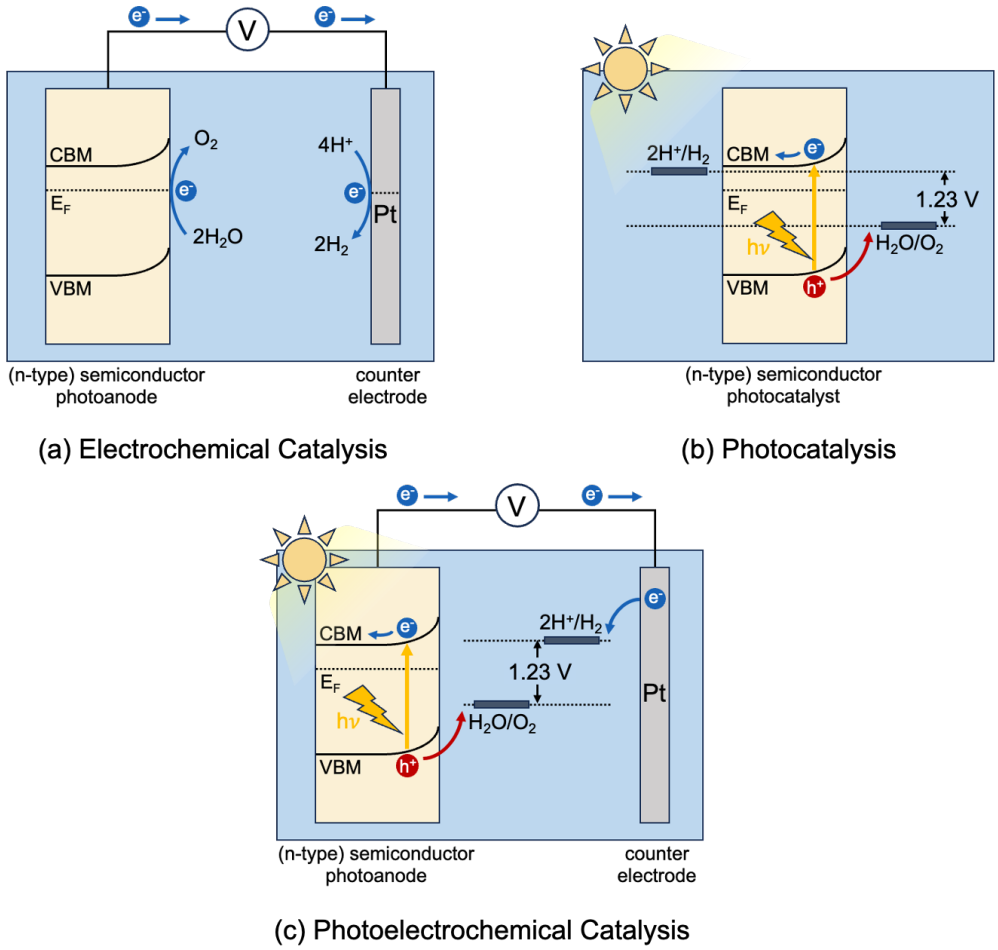

Figure 4.2.1 Illustrations of mechanisms of (a) electrochemical catalysis, (b) photocatalysis and (c) photoelectrochemical catalysis.

- **Electrochemical (EC) water splitting**

In electrochemical catalysis, the reaction is driven by an external electrical potential, which directly provides/withdraws electrons. The external power source provides the necessary driving force to overcome both the thermodynamic potential barrier and the kinetic overpotentials associated with OER and HER. In EC systems, the catalytic activity is governed by the relative position of the Fermi level of a semiconductor to the redox potentials of the adsorbed intermediates.[146] In electrochemical water splitting, the reaction proceeds via two half-reactions occurring at the anode and cathode, respectively, as follows:

i) Oxygen evolution reaction (OER) at the anode

$$2H_2O\ (l) \rightarrow O_2\ (g) + 4H^+ + 4e^-$$

where a four-electron transfer reaction is involved as described in Table 4.2.1:

Table 4.2.1 The reaction steps of electrochemical OER under acidic and neutral/basic conditions.

Acidic condition	Neutral/Basic condition
(i) H_2O (l) + * → *OH + H^+ + e^-	(i) * + OH^- → *OH + e^-
(ii) *OH → *O + H^+ + e^-	(ii) *OH + OH^- → *O + H_2O (l) + e^-
(iii) *O + H_2O (l) → *OOH + H^+ + e^-	(iii) *O + OH^- → *OOH + e^-
(iv) *OOH → * + O_2 (g) + H^+ + e^-	(iv) *OOH + OH^- → * + O_2 (g) + H_2O (l) + e^-

ii) Hydrogen evolution reaction (HER) at the cathode

$$4H^+ + 4e^- \rightarrow 2H_2\ (g)$$

where two kinds of reaction mechanisms can be considered: Volmer -Heyrovsky step (i → ii-1) and Volmer-Tafel step (i → ii-2), as summarized in Table 4.2.2:

Table 4.2.2 The reaction steps of HER under acidic and neutral/basic conditions.

Acidic condition	Neutral/Basic condition
(i) H^+ (eq) + e^- + * → H*	(i) H_2O (l) + e^- + * → H* + OH^- (eq)
(ii-1) H* + H^+ (eq) + e^- → H_2 (g) + *	(ii-1) H* + H_2O (l) + e^- → H_2 (g) + OH^- (eq)
(ii-2) H* + H* → H_2 (g) + *	(ii-2) H* + H* → H_2 (g)

- **Light-driven catalysis: Photocatalytic (PC) and Photoelectrochemical (PEC) water splitting**

While electrochemical water splitting offers high efficiency and technical maturity, photocatalytic (PC) and photoelectrochemical (PEC) approaches continue to receive considerable attention due to their potential for direct solar-to-hydrogen conversion in PC systems without relying on external electrical power, while PEC systems can operate in either unbiased or externally biased configurations. However, the mechanism of photo(electrochemical)catalysis is more complex than that of electrochemical catalysis because light-driven charge carriers are involved in the redox reactions.[147]

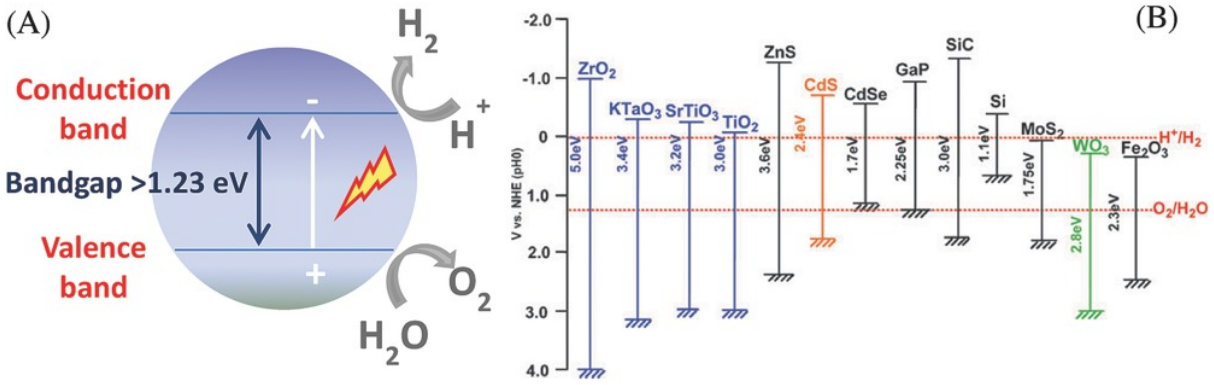

Figure 4.2.2 (a) Schematic of water splitting using semiconductor photocatalyst. (b) Band structure of semiconductors and redox potentials of water splitting.[148]

1) Photocatalytic (PC) water splitting

Photocatalytic water splitting utilizes semiconductor materials to directly convert a light source into chemical energy in the form of hydrogen. For overall water splitting to occur spontaneously, photocatalysts must satisfy two fundamental requirements:[148]

- **Band gap (Eg) energy:** The band gap must be at least 1.23 eV to provide the thermodynamic driving force for splitting water as shown in Figure 4.2.2 (a); however, in practice, a band gap of approximately 1.6–3.0 eV is necessary to overcome overpotentials and ensure efficient visible-light adsorption.
- **Band edge positions:** The conduction band minimum (CBM) must be above the H^+/H_2 reduction potential (0 V vs. NHE) and the valence band maximum (VBM) must be below the H_2O/O_2 oxidation potential (+1.23 V vs. NHE). Only when these energy levels are aligned, photogenerated electrons and holes respectively can drive the hydrogen evolution reaction (HER) and oxygen evolution reaction (OER). In that context, several representative examples of promising semiconductors for photocatalytic water splitting such as TiO_2 and CdS are shown in Figure 4.2.2 (b).

Narrower band gaps (<1.6 eV) allow absorption of a significant part of the solar spectrum but often position the conduction or valence band edges at insufficient potentials to drive the HER or OER. Conversely, wider band gaps (> 3.0 eV) provide strong driving forces for the reactions, but they limit light absorption mainly to the ultraviolet region, which accounts for less than 5% of solar irradiance. Therefore, finding an optimal band gap in the visible-light region while maintaining appropriate band edge alignment relative to the H^+/H_2 and O_2/H_2O redox potentials is essential for designing effective photocatalysts.[149]

Photocatalytic water splitting occurs through the three sequential steps:[150]

(1) **Photon adsorption and charge carrier generation**: A photocatalytically active semiconductor adsorbs a photon having energy greater than its band gap. As electrons are excited from the valence band (VB) to the conduction band (CB), electron-hole pairs are generated. The resulting carrier concentrations form electron and hole quasi-Fermi levels, which act as the reactive potential for subsequent reactions.

(2) **Charge separation and migration to the surface**: The generated electron-hole pairs are transported from the bulk to the surface, driven by the formed electric field in the space charge region.

(3) **Redox reactions with the generated charge carriers on the surface**: At the surface, the transported electrons and holes are transferred to adsorbates, initiating HER and OER, respectively.

Ultraviolet-driven photocatalysts (e.g., TiO_2, $SrTiO_3$) exhibit strong activity due to their wide band gaps, but their limited solar utilization efficiency motivates the search for visible-light-responsive photocatalyst such as CdS, GaP, or modified metal oxides.[151]

2) Photoelectrochemical (PEC) water splitting

Photoelectrochemical water splitting combines aspects of both electrolysis and photocatalysis. A PEC cell consists of a semiconductor photoelectrode (either a photoanode or a photocathode) and a counter electrode immersed in an electrolyte.[106] In the case of a photoanode, photogenerated holes migrate to the electrode surface, where they oxidize water to produce oxygen. The excited electrons travel through an external circuit to the photocathode, where they reduce protons to generate hydrogen. The first demonstration of PEC water splitting was reported by Honda and Fujishima in the 1970s using TiO_2 as photoanode coupled with a Pt counter electrode.[152]

For water splitting, the driving force for charge transfer arises from the potential difference between the quasi-Fermi levels of the photogenerated charge carriers and the redox potentials of the water splitting half-reactions. Specifically, hole and electron carriers are involved in oxidation and reduction reactions, respectively, as follows:

(i) Oxygen evolution reaction (OER) at the valence band of the photocatalyst or photoanode:

$$2H_2O\ (l) + 4h^+ \rightarrow O_2\ (g) + 4H^+$$

(ii) Hydrogen evolution reaction (HER) at the conduction band of the photocatalysis or photocathode:

$$2H^+ + 2e^- \rightarrow H_2\ (g)$$

The fundamental oxidation pathway in photo(electrochemical) water splitting involves the multi-step oxygen evolution reaction (OER). Since OER requires the sequential transfer of four electrons and protons, it is kinetically sluggish and strongly influenced by pH. The reaction steps of photo(electrochemical) OER under acidic and neutral/basic conditions are summarized in Table 4.2.3:

Table 4.2.3 The reaction steps of photo(electrochemical)catalytic OER under acidic and neutral/basic condition.

Acidic condition	Neutral/Basic condition
(i) H_2O (l) + h^+ + * → *OH + H^+	(i) * + OH^- + h^+ → *OH
(ii) *OH + h^+ → *O + H^+	(ii) *OH + OH^- + h^+ → *O + H_2O (l)
(iii) *O + h^+ + H_2O (l) → *OOH + H^+	(iii) *O + OH^- + h^+ → *OOH
(iv) *OOH + h^+ → * + O_2 (g) + H^+	(iv) *OOH + OH^- + h^+ → * + O_2 (g) + H_2O (l)

These reaction schemes highlight the role of photogenerated holes in driving surface oxidation and show how proton-coupled electron transfer (PCET) processes are modulated by the electrolyte environment. Understanding these pathways is essential for designing catalysts with reduced overpotentials and enhanced OER kinetics.

4.2.2 Theoretical Model for Light-driven Catalytic Reaction of Wide Band Gap Semiconductors

While the adsorption energy of electrochemical reactions is governed by the chemical potential of electrons, in photo(electrochemical) catalytic reactions, the photo-generated charge carriers also contribute to the surface kinetics and overall catalytic reactivity. However, the contribution of charge carriers to the photocatalytic reactions has still been overlooked in the calculation of adsorption energy. In recent years, many studies have highlighted the important role of photogenerated holes/electrons in photocatalytic redox reactions.[144,153,154] Especially, the theoretical work done by Harb et al. showed that the photocatalytic activity is determined by the suitable VBM/CBM position relative to water oxidation/hydrogen reduction potential.[155] It implies that the contribution of photoexcited carriers to the photocatalytic reactions should be considered to calculate the adsorption energy for the evaluation of the catalytic activity.[144]

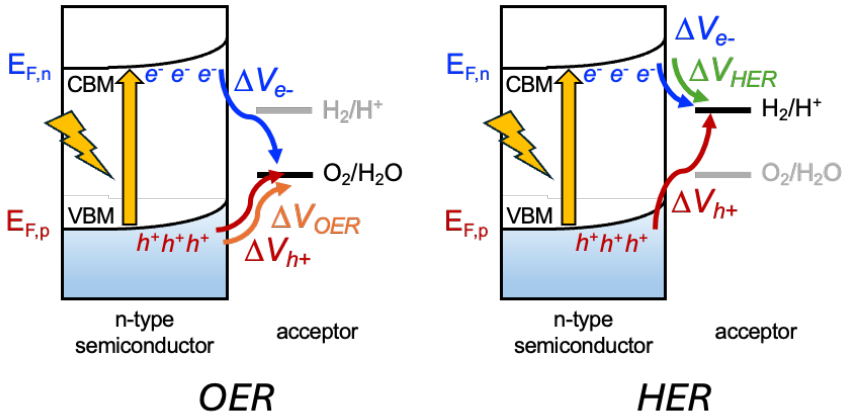

Figure 4.2.3 Schematic explanation of the consideration of the charge carrier potential for the adsorption energy calculations of the photocatalytic reaction.

Given that the relative position of the chemical potential of photoexcited charge carriers with respect to the redox potential governs the driving force for initiating reactions, the adsorption energy in photocatalytic reactions must be expressed as a function of the quasi-Fermi level of charge carriers. Therefore, the term for the driving force of photogenerated charge carriers towards the photocatalytic reactivity, $n\Delta V_{redox}$, is added into the equation of Gibbs free adsorption energy of semiconductors, which is given by (introduced in Chapter 4.1):[38,44]

$$G_{ads} = \Delta E_{\text{ads}} + \Delta ZPE + \int C_p dT - T\Delta S + \Delta G_{pH} + q(\varepsilon_F + E_{VBM}) \qquad (4.2.1)$$

For simplification, there are two major assumptions: (i) full photoexcitation, which defines hole- and electron quasi-Fermi levels that correspond to VBM and CBM, respectively, (ii) negligible electron-hole recombination, as supported by kinetic simulations showing that recombination losses are at most ~8% in the bulk and negligible at the surface.[153] In this context, in case of photocatalytic OER, ΔV_{redox} is ΔV_{OER} in Figure 4.2.3, which is the difference between hole quasi-Fermi level and water oxidation potential. For photocatalytic HER, ΔV_{redox} corresponds to ΔV_{HER}, the difference between electron quasi-Fermi level and hydrogen reduction potential. n is the number of charge carriers involved in each reaction step. Accordingly, the term for this driving force to the photocatalytic reactivity, $n\Delta V_{redox}$, is added in Eq (4.2.1) above.

In addition, according to Wolkenstein's theory,[156] charge carriers can move from a material to adsorbates if the adsorbates are strongly bound, a condition referred to as "strong chemisorption," leading to ionization of the adsorbates. In this context, we can additionally consider that light-driven electron-hole pairs possibly interact with charged adsorbates (*ads) on a semiconductor surface in photocatalytic reactions, as follows:

$$*ads^{-}\ (q = -1) + \text{photoexcited } h^{+} \rightarrow *ads'$$

$$*ads^{+}\ (q = +1) + \text{photoexcited } e^{-} \rightarrow *ads'$$

Adsorbates neutralized by surface charge carriers are denoted with a prime (′). For instance, during the water oxidation process, negatively charged $*OH^{-}$ on the surface of an n-type semiconductor can be oxidized to neutral *OH by a hole carrier transferred from the VBM. If the *OH species generated by the oxidation of $*OH^{-}$ is thermodynamically more stable than the neutral *OH, the OER process will involve this additional reaction step (**ads'*-mediated step); otherwise, the neutral *OH will directly participate in the reaction. (**ads*$^{-}$ or **ads*$^{+}$-mediated step)

$$\Delta G_{*ads^{-}} + \Delta V_{h^{+}}\ or\ \Delta G_{*ads^{+}} + \Delta V_{e^{-}} \geq \Delta G_{*ads} \rightarrow *ads'\text{-mediated step}$$

$$\Delta G_{*ads^{-}} + \Delta V_{h^{+}}\ or\ \Delta G_{*ads^{+}} + \Delta V_{e^{-}} < \Delta G_{*ads} \rightarrow *ads^{-} \text{ or } *ads^{+}\text{-mediated step}$$

In this context, the term $\Delta V_{h^{+}/e^{-}}$ is added to consider the potential neutralization of charged adsorbates by interactions with charge carriers on the surface.

As a result, the equation of Gibbs free adsorption energy of photocatalytic redox reactions is defined as follows:

$$\Delta G_{ads} = \Delta E_{ads} + \Delta ZPE + \int C_p dT - T\Delta S + \Delta G_{pH} + q(\varepsilon_F + E_{VBM}) + n\Delta V_{redox} + m(\Delta V_{h^{+}} + \Delta V_{e^{-}}) \quad (4.2.2)$$

ΔV_{h^+} and ΔV_{e^-} in Eq (4.2.2) corresponds to the energy required for the hole carrier to oxidize the negatively charged adsorbates (q = -1) and that for the electron carrier to reduce the positively charged adsorbates (q = +1), respectively, and m is the number of required holes or electrons for neutralization.

For water oxidation, ΔE_{ads} in Eq (4.2.2) is the bonding energy of adsorbates calculated for water oxidation using the following equations:

$$\Delta E_{*\mathrm{OH}} = E_{*OH} - E_{*} - E_{H_2O} + \frac{1}{2}E_{H_2} \tag{4.2.3}$$

$$\Delta E_{*O} = E_{*O} - E_{*} - E_{H_2O} + E_{H_2} \tag{4.2.4}$$

$$\Delta E_{*OOH} = E_{*OOH} - E_{*} - 2E_{H_2O} + \frac{3}{2}E_{H_2} \tag{4.2.5}$$

The terms ΔZPE, $\int C_p dT$, and $T\Delta S$ in Eq (4.2.2) are the change of zero-point energy, enthalpy, and entropy contributions at temperature T to a Gibbs free energy of an adsorbate, respectively. ΔG_{pH} is the correction for pH contribution to the reactivity, which is defined as $-nk_BTln10pH$, where k_B is the Boltzmann constant and n denotes the number of charge carriers involved in each reaction step. For the Fermi level-dependency of the adsorption energy correction, q, ε_F and E_{VBM} in Eq (4.2.2) are the possible charge state of the adsorbates due to charge transfer, the Fermi level that ranged over the band gap of TiO_2 (anatase TiO_2: 3.2 eV, rutile TiO_2: 3.0 eV), and the DFT-computed eigenvalue of the VBM energy level of the TiO_2 slab with the adsorbate, respectively. The charge state (q) of intermediates: O (q = -2, -1, 0, +1), OH (q = -1, 0, +1), and OOH (q = -1, 0, +1) were considered.

4.2.3 Results and Discussion

For the prototype study, TiO_2, one of the classical photocatalytic materials, was employed as a model material. Since the pioneering work of Fujishima and Honda in 1972,[157] TiO_2 has emerged as a promising photocatalytic material for water splitting due to its chemical stability, natural abundance, and non-toxicity, and it has remained a subject of active investigation.[152]

TiO_2 exists in three major morphologies: anatase, rutile, and brookite. Among the polymorphs of TiO_2, anatase (A-TiO_2) and rutile TiO_2 (R-TiO_2) have been most extensively investigated for their photocatalytic activity due to their higher thermodynamic stability, ease of synthesis, and wide range of practical applications.[158,159] The crystallographic properties of A-TiO_2 and R-TiO_2 are outlined in the Table 4.2.4:

Table 4.2.4 The reaction steps of electrochemical OER under acidic and neutral/basic condition.[160]

	Anatase (A-TiO_2)	**Rutile (R-TiO_2)**
Crystal structure	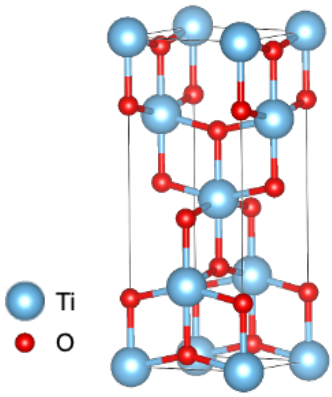 Tetragonal	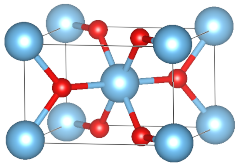 Tetragonal
Lattice constant (Å)	a = 4.5936 c = 2.9587	a = 3.784 c = 9.515
Space Group	P42/mnm	$I4_1/amd$
Molecule (cell)	2	2
Volume/molecule ($Å^3$)	31.21	34.061
Density (g cm^{-3})	4.13	3.79
Band gap (eV)	3.2 (indirect)	3.02 (direct)

On the TiO_2 surface, Ti atoms are present as six-fold (Ti_{6c}) and five-fold (Ti_{5c}) coordinated sites, while oxygen atoms appear as in-plane three-fold (O_{3c}) and bridging two-fold (O_{2c}) coordinated sites. Among these, the Ti_{5c} and O_{2c} atoms are coordinatively unsaturated, existing on the primary surface-active sites. In bulk anatase, each Ti atom is surrounded by a distorted TiO_6 octahedron with O_{3C} coordination, resulting in a more distorted local geometry compared to rutile.[161]

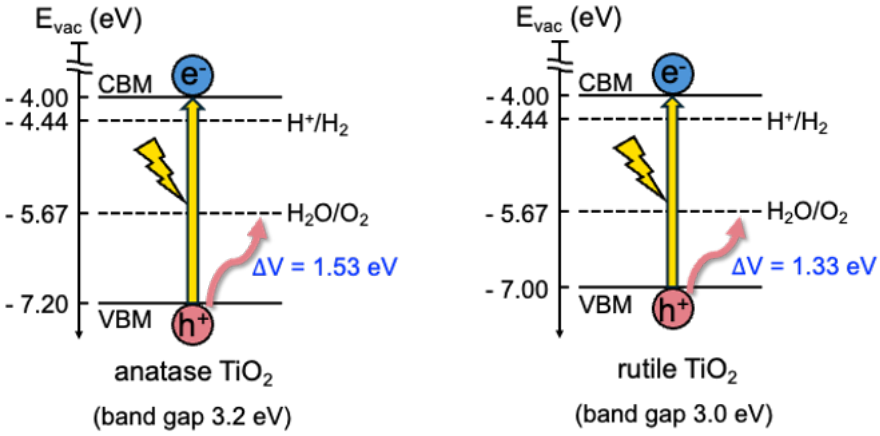

Figure 4.2.4 The energy band diagram of A-TiO_2 (left) and R-TiO_2 (right).[162]

Figure 4.2.4 shows the energy band diagram representing the relative alignment of the VBM and CBM.[163] According to the position of VBM, the values of ΔV for A-TiO_2 and R-TiO_2 are 1.53 eV and 1.33 eV, respectively. It implies that the valence band edge of anatase is positioned at a higher potential than that of rutile, providing a stronger driving force for hole-induced oxidation reactions. Hence, anatase is expected to exhibit superior photocatalytic activity for the OER due to its higher hole-driving capability.

Despite extensive research on the mechanism of water splitting on TiO_2, several aspects remain controversial:

(i) Phase-dependence of the photocatalytic activity of TiO_2

It is well known that R-TiO_2 is thermodynamically more stable than A-TiO_2, whereas the photocatalytic activity of A-TiO_2 is higher than that of R-TiO_2. Many studies have proposed rationales for the higher photocatalytic activity of A-TiO_2 compared with R-TiO_2:[164] (i) the indirect band gap nature of anatase, leading to a longer photo-induced charge carrier lifetime. (ii) the larger band gap of anatase (3.2 eV) than that of rutile (3.0 eV) and different position of band edges, providing a stronger thermodynamic driving force for redox reactions (iii) superior charge transport properties in anatase, attributed to a smaller effective mass of charge carriers; and (iv) intrinsic differences in surface properties and structures.

(ii) Facet-dependence of the photocatalytic activity

The A-TiO_2 (101) possesses the lowest surface energy among A-TiO_2 facets (0.44 J m^{-2}) and that of A-TiO_2 (001) is approximately 0.90 J m^{-2}. Nevertheless, it has been demonstrated that the (001) facet exhibits higher catalytic activity for photocatalytic water splitting than that of A-TiO_2 (101).[165] The superior photocatalytic activity of the A-TiO_2 (001) facet is generally attributed to its atomic configuration. It can be predicted that since the A-TiO_2 (001) facet has a higher surface energy than the A-TiO_2 (101) facet, which is generally associated with higher reactivity, surfaces with elevated surface energies tend to stabilize their intrinsic instability through stronger interactions with adsorbates. To be specific, all surface Ti atoms are 5-fold-coordinated Ti atoms (Ti_{5c}) in A-TiO_2 (001) can offer more active sites and stronger adsorbate binding. On the other hand, A-TiO_2 (101) exposes equal proportions of Ti_{5c} and Ti_{6c}, leading to comparatively lower activity.

Extensive theoretical and experimental efforts have been devoted to elucidating the reaction mechanisms of photocatalytic water splitting, providing insights into the facet- and phase-dependent reactivity of TiO_2. For example, electronic band structure analyses have been carried out to rationalize the intrinsic properties of TiO_2.[166] Kakuma et al. reported that the difference in TiO_2 photocatalytic mechanism between rutile and anatase arises from the Ti-Ti distance on the surface, in which anatase stabilizes trapped holes for •OH formation, while rutile promotes hole pairing into Ti-OO-Ti dimers.[167] Also, Li et al. investigated that rutile can be active under UV light, while anatase requires prolonged irradiation due to kinetic differences in intermediates and thermodynamic trapped states.[168] Recently, Wang et al. demonstrated that the concentration of surface-reaching photogenerated holes determines the photocatalytic water splitting instead of being limited by the intrinsic catalytic activity of R-TiO_2 (110).[144]

Nevertheless, the underlying reaction mechanisms are not yet fully understood. From a theoretical perspective, it can be reasoned that one of the contributing factors is that the contribution of photoexcited charge carriers to the reactivity has still been neglected in the adsorption calculations; the accuracy of commonly used energy profile calculations may be limited. In this regard, this new theoretical framework may provide a more comprehensive explanation of the observed reactivity.

In this work, A-TiO_2 (001) was employed as a reference, and its catalytic activity will be compared with that of A-TiO_2 (101) to investigate facet-dependent activity and with R-TiO_2 (110) to examine phase-dependent activity.

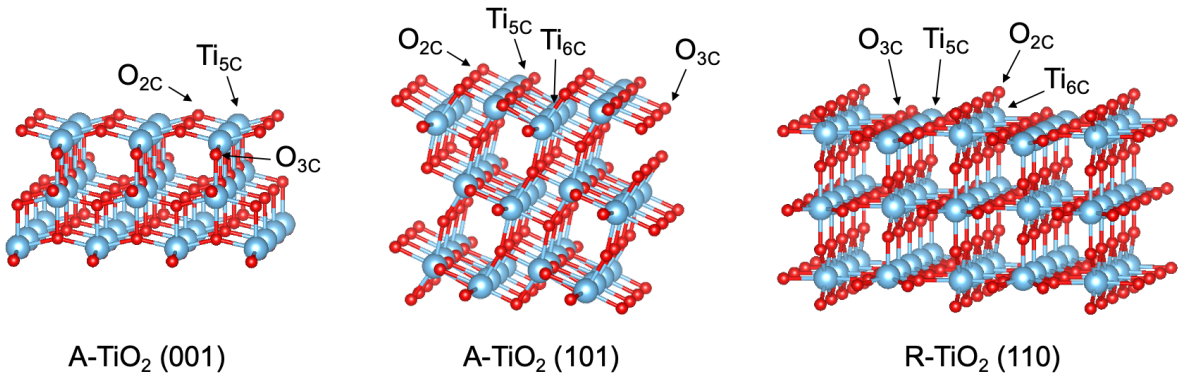

Figure 4.2.5 Crystal structures of A-TiO_2 (001), A-TiO_2 (101) and R-TiO_2 (110). The red and light-blue balls denote O and Ti atoms, respectively.[169]

Figure 4.2.5 shows crystal structures of A-TiO_2 (001), A-TiO_2 (101) and R-TiO_2 (110). The A-TiO_2 (001) exhibits undercoordinated sites, which are Ti_{5C}-rich terminations and equal

distribution of O_{2C} and O_{3C} atoms, making it more reactive. In contrast, A-TiO_2 (101) has comparable proportions of Ti_{5C} and Ti_{6C} sites, as well as O_{2C} and O_{3C} atoms. Similar to A-TiO_2 (101), the R-TiO_2 (110) surface consists of rows of Ti_{5C} and O_{2C} with in-plane Ti_{6C} bonded with O_{3C}, with Ti_{5C} and Ti_{6C} existing in approximately equal numbers.[170–172]

The adsorption energies of OER intermediates were calculated using Eq (4.2.1) without the consideration of charge carrier contribution/in the dark. In addition, the total energy barriers of OER in the dark ($\Delta E_{barrier}$)/with illumination ($\Delta E^0_{barrier}$) on A-TiO_2 as a function of the Fermi level are calculated and the graphs were depicted in Figure 4.2.6 and 4.2.7. To compare the catalytic reactivity of OER in photocatalytic water splitting, the rate constant of OER in the dark as a reference to comparison (R_0) and with illumination (R) is compared and the rate constant ratio was calculated as follows:

$$\frac{R}{R_0} = \exp\left(-\frac{\Delta E_{barrier} - \Delta E^0_{barrier}}{kT}\right) \tag{4.2.6}$$

4.2.3.1 Oxygen Evolution Reaction (OER)

The adsorption energies of OER intermediates were calculated using Eq (4.2.2) as shown in Figure 4.2.6 and 4.2.7. As mentioned, A-TiO_2 (001) was employed as a reference to compare the catalytic activity with A-TiO_2 (101) and R-TiO_2 (110). The adsorption energies of *OH, *O, and *OOH were evaluated as a function of the Fermi level to elucidate the thermodynamically favorable reaction pathway and charge state of adsorbates-dependent behavior of each intermediate.

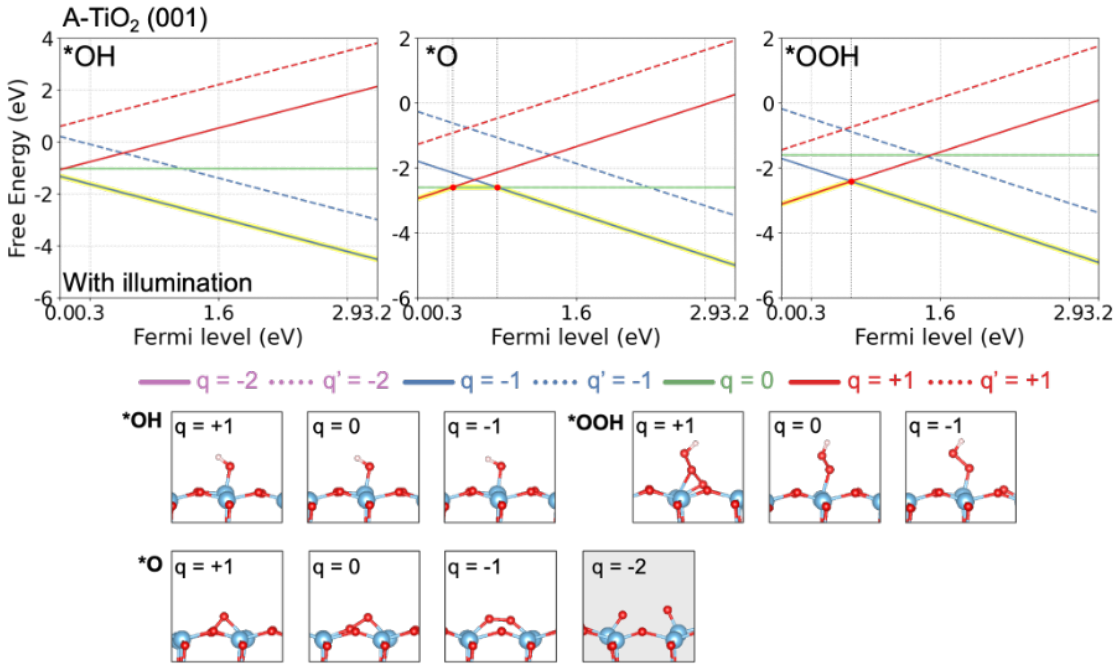

Figure 4.2.6 The adsorption energies of OER intermediates (*OH, *O and *OOH) of A-TiO_2 (001) as a function of the Fermi level and the adsorption configuration of OER intermediates. Red, light blue, and pink balls represent O, Ti, and H atoms, respectively. The gray-shaded $*O^{2-}$ configuration indicates that adsorption does not occur.

For A-TiO_2 (001), the adsorption of O* charged with -2 ($*O^{2-}$) is not thermodynamically favorable because it leads to the breaking of surface Ti-O bonds in the TiO_2 lattice. Negatively charged *OH is the most stable configuration regardless of the Fermi level, whereas the thermodynamically preferred charge state of *O and *OOH varies depending on the Fermi level, which are +1, 0, and -1 for *O and +1 and -1 for *OOH, respectively.

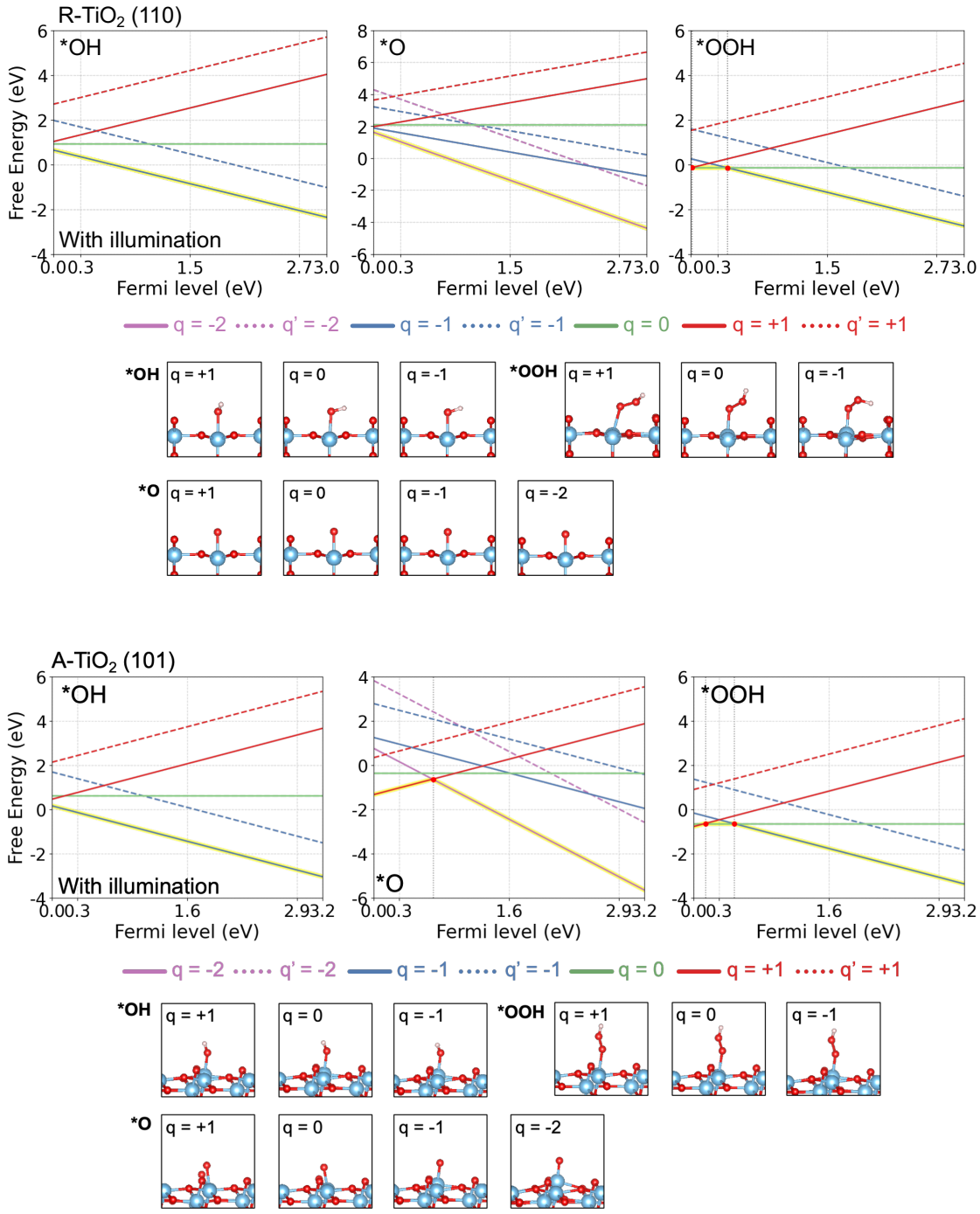

Figure 4.2.7 The adsorption energies of OER intermediates (*OH, *O and *OOH) of R-TiO_2 (110) and A-TiO_2 (101) as a function of the Fermi level and the adsorption configuration of OER intermediates. Red, light blue, and pink balls represent O, Ti, and H atoms, respectively.

For R-TiO_2 (110), *OH and *O adsorbates are thermodynamically stable only in the neutral charge state (q = 0), whereas the neutral *OOH adsorbate is favored when R-TiO_2 (110) has a heavily p-type character. In the case of A-TiO_2 (101), negatively charged $*OH^-$ and *O charged

with +1 and -2 (*O^- and *O^{2-}) are favorable. The thermodynamically preferred charge state of *OOH is also variable, similar to other facets.

Charge neutralization is not expected to spontaneously occur on A-TiO_2 (001), (101), and R-TiO_2 (110). It indicates that the favored reaction pathway for photocatalytic OER on TiO_2 is dependent on the surface termination (facet/phase) and the Fermi level.

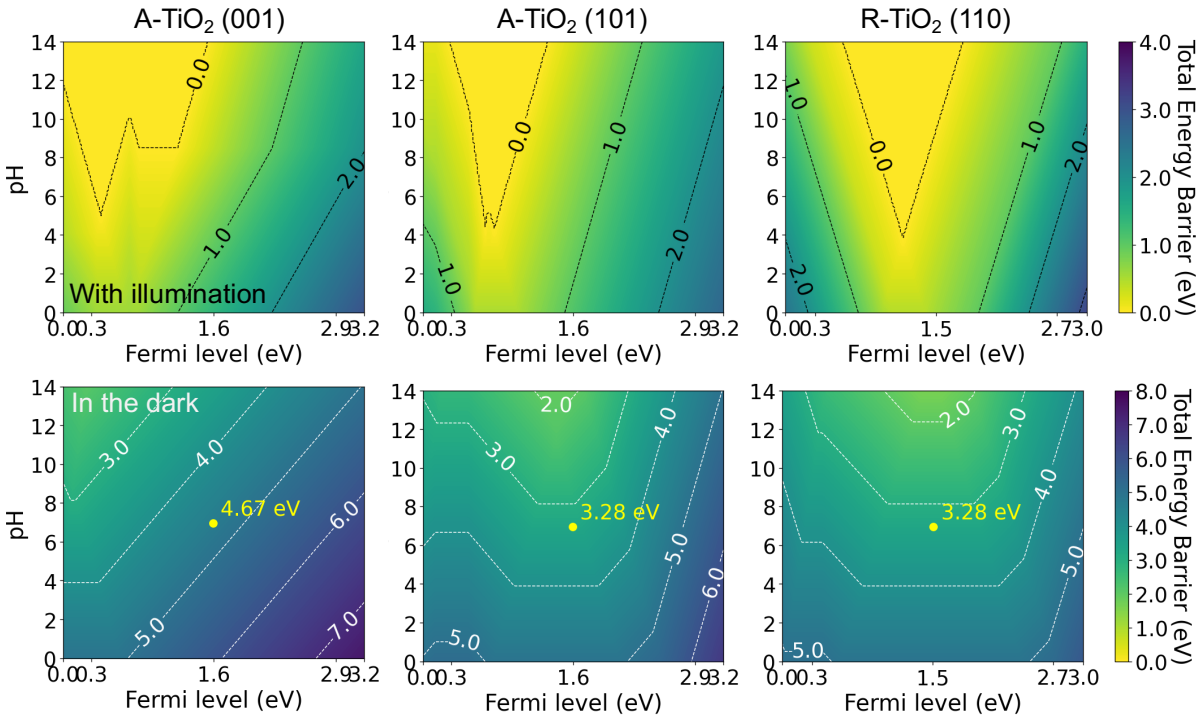

Figure 4.2.8 The contour maps of the total energy barriers of OER as functions of the Fermi level (eV) and pH with illumination (top)/in the dark (bottom) of A-TiO_2 (001), A-TiO_2 (101), and R-TiO_2 (110), respectively.

Furthermore, the contour maps of the total energy barrier as functions of the Fermi level and pH, both with and without illumination, are shown in Figure 4.2.8 to see the dependence of reaction energetics on the reaction conditions (pH and surface Fermi level). Considering the band bending induced at the material-electrolyte interface, the typical reaction condition for photocatalytic water splitting (pH = 7, without an applied bias) was taken as the reference, where the Fermi level lies at the mid-gap in the dark. The values of the reference are indicated by the yellow dots in Figure 4.2.8. It shows that under illumination, A-TiO_2 (001) exhibits a wider region with a lower total energy barrier (close to zero, represented by the yellow area), whereas in the dark, its energy barrier is relatively higher compared to A-TiO_2 (101) and R-

TiO_2 (110). This result suggests that the photocatalytic reactivity of A-TiO_2 (001) is significantly enhanced under illumination, relative to A-TiO_2 (101) and R-TiO_2 (110).

To compare the catalytic activity of R-TiO_2 (110), A-TiO_2 (001), and A-TiO_2 (101), the contour maps were generated using a self-written Python code based on Eq (4.2.6). (Figure 4.2.9)

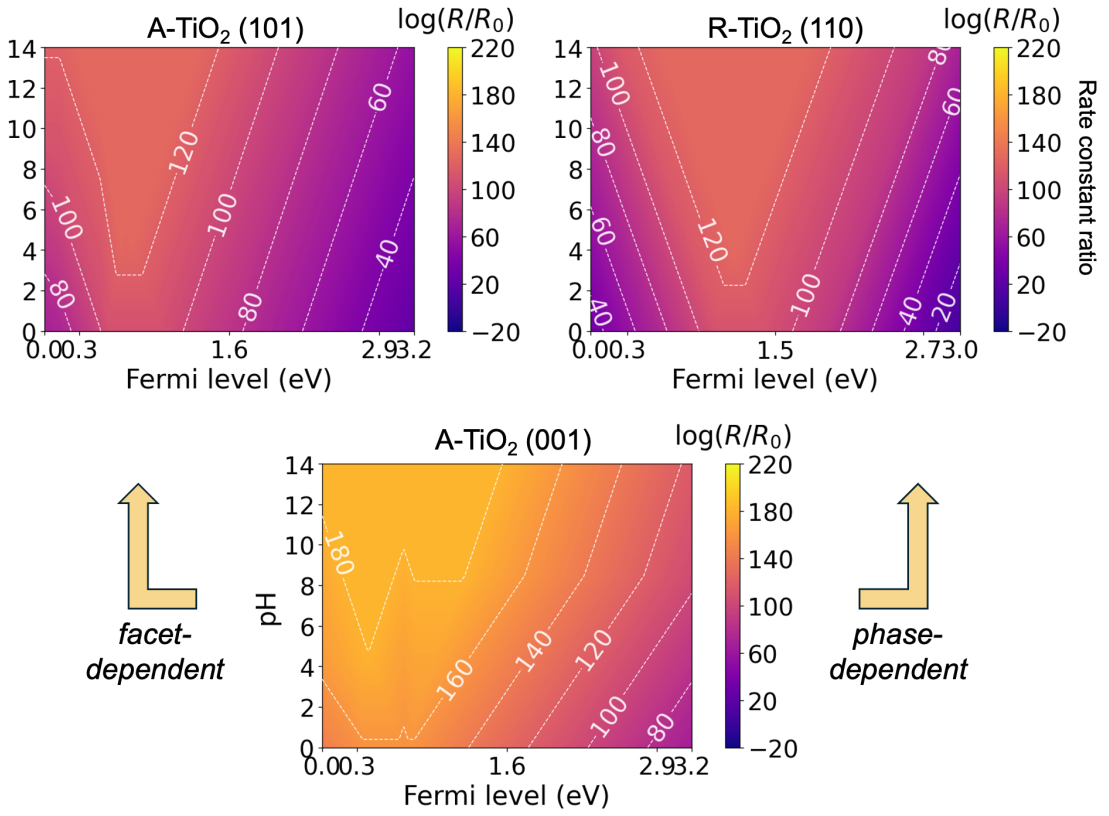

Figure 4.2.9 The contour maps of rate constant ratio on a logarithmic scale as functions of the Fermi level (eV) and pH of A-TiO_2 (101), R-TiO_2 (110), and A-TiO_2 (001). The contour lines and numbers in the graph denote the logarithmic value of the rate constant ratio.

Similar to the total energy barrier contour maps, the brighter regions indicate higher photocatalytic activity for the OER under illumination compared to that in the dark. To identify the trend first, A-TiO_2 (001) exhibits the highest calculated activity among the studied facets, with the minimum log (R/R_0) value exceeding 60, while A-TiO_2 (101) and R-TiO_2 (110) show lower values of approximately 20 and 0, respectively.

For all TiO_2 surfaces, the photocatalytic OER activity tends to increase under conditions with a higher hole concentration (at pH = 7). In contrast, for R-TiO_2 (110), the reaction becomes more favorable when the Fermi level is located near the mid-gap, whereas an excessively p-type condition appears to be less favorable for the OER.

(i) Phase-dependent photocatalytic OER activity: A-TiO_2 (001) and R-TiO_2 (110)

Without applying the additional term to calculate the adsorption energy, A-TiO_2 (001) exhibits a higher total energy barrier at pH = 7 compared to R-TiO_2 (110), which does not theoretically support many previous experimental observations. In contrast, when the newly derived theoretical model that accounts for the consideration of charge carriers is applied, there is a significant difference in the total energy barrier as a function of the Fermi level for both A-TiO_2 (001) and R-TiO_2 (110).

To quantitatively compare the photocatalytic activity of OER between A-TiO_2 (001) and R-TiO_2 (110), the rate constant ratio of the photocatalytic OER (with illumination) to OER (in the dark) was evaluated. We can clearly see that A-TiO_2 (001) exhibits higher OER performance with a lower total energy barrier than that of R-TiO_2 (110), consistent with the experimental observation. Furthermore, these results suggest that optimizing both OER on A-TiO_2 (001) and R-TiO_2 (110) toward p-type properties is beneficial, as photo-generated hole carriers play a crucial role in the photocatalytic reactions.

(ii) Facet-dependent photocatalytic OER activity: A-TiO_2 (001) and A-TiO_2 (101)

In a manner similar to R-TiO_2 (110), A-TiO_2 (101) shows a lower energy barrier than A-TiO_2 (001) under dark conditions. However, when charge carriers are considered in the adsorption energy calculations, A-TiO_2 (001) demonstrates higher OER performance than A-TiO_2 (101). It was predicted that the trends in phase- and facet-dependent reactivity of TiO_2 are analogous. Indeed, some studies have reported that the OER activities of R-TiO_2 (110) and A-TiO_2 (101) with illumination are comparable.

In both cases, phase- and facet-dependent photocatalytic activities, the main theoretical challenge in elucidating the mechanism underlying these differences lies in the limitations of standard models, which have neglected the significant contribution of charge carriers to the absorption behaviour. In this work, the driving force of photo-generated holes is quantified by considering the difference between the hole quasi-Fermi level and the oxidation potential in photocatalytic oxidation, thereby providing an explanation for this discrepancy.

Indeed, pristine TiO_2 has limited photocatalytic activity for overall water splitting due to its wide band gap, rapid electron-hole recombination, and intrinsically low surface reactivity. To enhance its catalytic reactivity, various modification strategies such as cocatalyst deposition and defect engineering have been employed to fabricate more efficient TiO_2-based

photocatalysts. For example, IrO_2 and RuO_2 are commonly used to promote the OER activity of TiO_2.[173] Furthermore, adjusting the electronic properties of TiO_2 by heterojunction formation with semiconductors (such as g-C_3N_4) or introducing dopants can enhance OER activity by facilitating charge separation and improving hole transport.[174] In general, achieving stable heavily p-type TiO_2 remains challenging;[173] therefore, heterojunction design has been demonstrated as a more feasible and effective approach to increase hole concentration and transport efficiency.

4.2.3.2 Hydrogen Evolution Reaction (HER)

Even though OER is a bottleneck of water splitting because it involves multi-step reactions, HER activity is also essential to evaluate the reactivity of water splitting. It is generally known that the hydrogen evolution reaction (HER) takes place via either the Volmer-Heyrovsky or the Volmer-Tafel mechanism. Each reaction step can be written as follows:[175,176]

Volmer step: $H^+ + e^- + * \rightarrow H^*$

Heyrovsky step: $H^* + H^+ + e^- \rightarrow H_2\,(g) + *$

Tafel step: $H^* + H^* \rightarrow H_2\,(g) + 2*$

However, as mentioned above, since the adsorbates can be charged depending on the properties of a semiconductor, the contribution of charge carriers to the redox reaction must be considered. In that context, each reaction step is written as presented in Table 4.2.5:

Table 4.2.5 The reaction steps of the hydrogen evolution reaction (HER)

Volmer step	Heyrovsky step	Tafel step
$H^+\,(aq) \rightarrow *H^+$	$*H^+ + (H^+\,(aq) + e^-) + e^- \rightarrow H_2\,(g)$	$*H^+ + *H^+ + 2e^- \rightarrow H_2\,(g)$
$H^+\,(aq) + e^- \rightarrow *H$	$*H + (H^+\,(aq) + e^-) \rightarrow H_2\,(g)$	$*H + *H \rightarrow H_2\,(g)$
$H^+\,(aq) + 2e^- \rightarrow *H^-$	$*H^- + (H^+\,(aq) + e^-) + h^+ \rightarrow H_2\,(g)$	$*H^- + *H^- + 2h^+ \rightarrow H_2\,(g)$

For HER, the Gibbs free adsorption energy is obtained using Eq (4.2.2), where ΔV_{redox} is the difference between the electron quasi-Fermi level (i.e., CBM assuming full photoexcitation) and hydrogen reduction potential. The equations of Gibbs free adsorption energy of each reaction step are written as:

1) **Volmer Step**

$$\Delta G_{Volmer} = G_{H^*(q=+1,0,-1)} - G_* - \frac{1}{2}G_{H_2} + k_B T ln10 \cdot pH + q(\varepsilon_F + E_{VBM}) + \Delta V_{HER} + e(\Delta V_{h^+} + \Delta V_{e^-}) \quad (4.2.7)$$

2) **Heyrovsky Step**

$$\Delta G_{Heyrovsky} = G_{H_2} - G_* - G_{H^*(q=+1,0,-1)} - \frac{1}{2}G_{H_2} + k_B T ln10 \cdot pH - q(\varepsilon_F + E_{VBM}) + \Delta V_{HER} + e(\Delta V_{h^+} + \Delta V_{e^-}) \quad (4.2.8)$$

3) **Tafel Step**

$$\Delta G_{Tafel} = G_{H_2} - 2G_* - 2G_{H^*(q=+1,0,-1)} - 2q(\varepsilon_F + E_{VBM}) + 2e(\Delta V_{h^+} + \Delta V_{e^-}) \quad (4.2.9)$$

Based on the charge state of the adsorbates, the reaction steps of HER can be written as follows:

• The Volmer-Heyrovsky mechanism

In the Volmer-Heyrovsky mechanism, one adsorbed hydrogen atom reacts with a proton and an electron to form molecular hydrogen, without requiring the recombination of two adsorbed hydrogen atoms on the surface. Considering the possible charge states of *H adsorption, *ads$^-$-/*ads$^+$-mediated step, and *ads'-mediated step were considered (Table 4.2.6).

Table 4.2.6 The reaction steps of the Volmer-Heyrovsky mechanism of hydrogen evolution reaction (HER).

***H$^-$ (q = -1)**	***H (q = 0)**	***H$^+$ (q = +1)**
(i) H^+ (aq) + * → *H^+	(i) H^+ (aq) + * → *H^+	(i) H^+ (aq) + * → *H^+
(ii) *H^+ + 2e^- → *H^-	(ii) *H^+ + e^- → *H	(ii) *H^+ → *H^+
(iii) *H^-+H^+(aq)+ e^- →H_2 (g)	(iii) *H+ H^+(aq)+e^- →H_2 (g)	(iii) *H^++H^+(aq)+2e^- →H_2 (g)

***H' (q' = +1)**	***H' (q' = -1)**
(i) H^+ (aq) + * → *H^+	(i) H^+ (aq) + * → *H^+
(ii) *H^+ → *H^+	(ii) *H^+ + 2e^- → *H^-
(iii) *H^+ + e^- → *H'	(iii) *H^- + h^+ → *H'
(iv) *H' + H^+ (aq) + e^- → H_2 (g)	(iv) *H' + H^+ (aq) + e^- → H_2 (g)

• The Volmer-Tafel mechanism

In the Volmer-Tafel mechanism, two adsorbed hydrogen atoms combine on the catalyst surface to form molecular hydrogen, without further electron transfer. (Table 4.2.7)

Table 4.2.7 The reaction steps of the Volmer-Tafel mechanism of hydrogen evolution reaction (HER).

***H$^-$ (q = -1)**	***H (q = 0)**	***H$^+$ (q = +1)**
(i) H^+ (aq) + * → *H^+	(i) H^+ (aq) + * → *H^+	(i) H^+ (aq) + * → *H^+
(ii) *H^+ + 2e^- → *H^-	(ii) *H^+ + e^- → *H	(ii) *H^+ → *H^+
(iii) *H^- + *H^- + 2h^+ → H_2 (g)	(iii) *H + *H → H_2 (g)	(iii) *H^+ + *H^+ + 2e^- → H_2 (g)

According to the Sabatier principle,[45] the adsorbate should be adsorbed neither strongly nor weakly.[45] Therefore, the value of ΔG_{H^*} closest to zero in the Volmer step, which is the rate-determining step, is used as the main criterion to evaluate the favored reaction pathway of HER. In this context, the thermodynamically preferred charge state of adsorbates in the Volmer step varies with the Fermi level, thereby governing the subsequent reaction pathway.

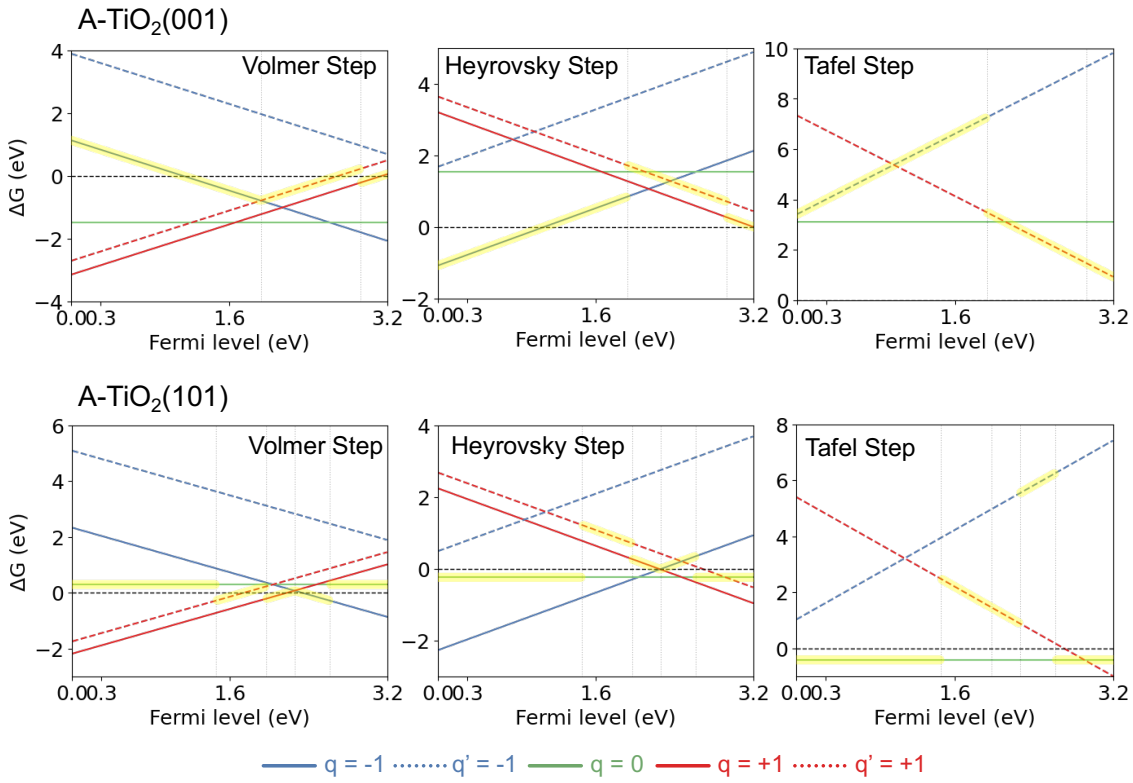

Figure 4.2.10 The adsorption energy graph of HER intermediates, total energy barrier as a function of Fermi level and the contour map of total energy barrier as a function of pH and Fermi level of A-TiO_2 (001) and A-TiO_2 (101). The solid and dashed lines represent ads^+-/ads^--mediated and ads'-mediated reaction pathways. The blue, green, and red solid lines are adsorption energies of the adsorbates charged with q = -1, 0, and +1, respectively. The blue and red dashed lines denote q' = -1 and +1 via ads'-mediated reaction pathways, respectively.

Figure 4.2.10 shows the Gibbs free energies of Volmer, Heyrovsky, and Tafel step as a function of the Fermi level of A-TiO_2 (001) and A-TiO_2 (101) at pH = 7 which were calculated using Eq (4.2.7) – (4.2.9). For HER on A-TiO_2 (001), *H adsorption is predicted to be weak when the Fermi level lies between 0 and approximately 1.11 eV, and strong between 1.1 and 2.3 eV. The optimal *H adsorption ($\Delta G_{H^*} \approx 0$ eV) occurs when the Fermi level is around 1.1, 2.71, and 2.94 eV. The Heyrovsky step is thermodynamically favorable when the Fermi level lies between 0 eV and 1.11 eV, while the Tafel step takes place spontaneously at the Fermi level between 1.91 eV and 3.2 eV. Hence, the dominant HER mechanism on A-TiO_2 (001) is expected to vary depending on the Fermi level; in particular, when the Fermi level ranges from 1.91 eV to 2.71 eV, a photogenerated electron is likely to neutralize the positively charged $*H^+$ via an ads'-mediated reaction pathway.

In the case of photocatalytic HER on A-TiO_2 (001), the Fermi level ranges from 1.46 eV to 1.97 eV, a photogenerated electron is likely to neutralize the positively charged $*H^+$ via an

ads'-mediated reaction pathway. The Heyrovsky and Tafel steps on A-TiO_2 (001) are predicted to proceed spontaneously when the Fermi level range lies in the ranges of 0 – 1.46 eV and 2.62 – 3.2 eV.

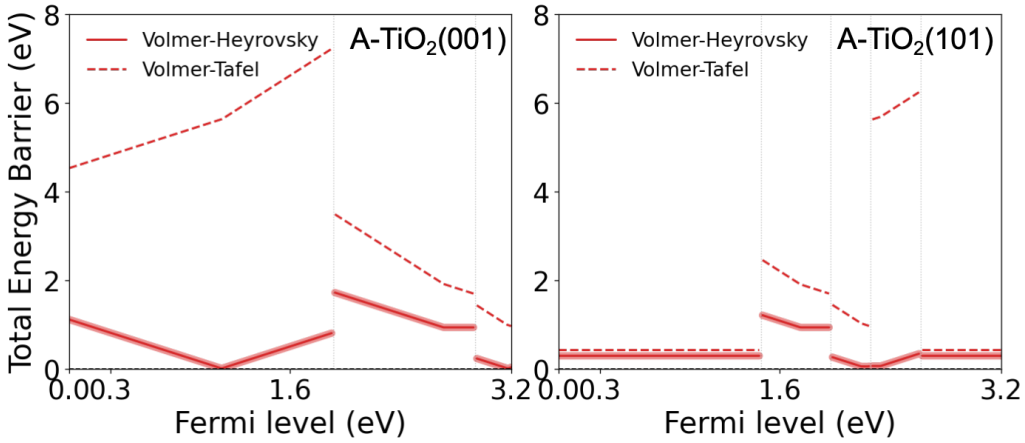

Figure 4.2.11 The graphs of the total energy barrier of HER on A-TiO_2 (001) and A-TiO_2 (101) as a function of the Fermi level at pH = 7. Solid line and dashed line represent the Volmer-Heyrovsky and the Volmer-Tafel mechanism, respectively. Highlighted red lines indicate the favored reaction pathway of HER.

Figure 4.2.11 shows the total energy barriers for the Volmer–Heyrovsky and Volmer–Tafel mechanisms on A-TiO_2 (001) and (101) as a function of the Fermi level at pH = 7. Solid and dashed lines represent the Volmer–Heyrovsky and Volmer–Tafel mechanisms, respectively, and the highlighted red lines indicate the most favorable reaction pathways. The total energy barriers for both mechanisms were calculated by considering the charge states stabilized during the Volmer step.

A comparison of the total energy barrier between the Volmer-Heyrovsky mechanism and the Volmer-Tafel mechanism on A-TiO_2 (001) and A-TiO_2 (101) showed that the Volmer–Tafel mechanism is thermodynamically not favored due to its high barrier, regardless of the Fermi level. For A-TiO_2 (001), spontaneous photocatalytic HER is expected when the Fermi level is tuned to around 1.46 eV. This level aligns well with the Fermi level of Pt (work function ≈ 5.6 eV),[177,178] suggesting efficient electron transfer across the interface and enhanced HER activity when Pt is used as a cocatalyst. The predicted favored reaction pathways on A-TiO_2 (001) depending on the Fermi level (E_F) are summarized as follows:

(i) 0 eV < E_F < 1.92 eV: the Volmer–Heyrovsky pathway with q = 0
(ii) 1.92 eV < E_F < 2.93 eV: the Volmer–Heyrovsky pathway with H'-mediated reaction step with q' = +1
(iii) 2.93 eV < E_F < 3.20 eV: the Volmer–Heyrovsky pathway with q = +1

For A-TiO_2 (101), it was predicted that *H was weakly adsorbed on A-TiO_2 (101) (ΔG_{H^*} < 0.5 eV), which facilitates H* desorption and promotes the H_2 evolution. The reaction is predicted to proceed spontaneously when the Fermi level is around 2.19 eV, indicating that Au, Rh or Pd—with its suitable work function (~5.01 eV) and weak hydrogen binding—could serve as a potential cocatalyst to improve HER activity.[179] The expected reaction mechanisms as a function of the Fermi level are as follows:

(i) 0 < E_F < 1.46 eV, 2.62 eV < E_F < 3.2 eV: the Volmer-Heyrovsky pathway with q = 0
(ii) 1.46 eV < E_F < 1.97 eV: the Volmer-Heyrovsky pathway with *H'-mediated reaction pathway q = +1
(iii) 1.97 eV < E_F < 2.26 eV: the Volmer-Heyrovsky pathway with q = +1
(iv) 2.26 eV < E_F < 2.62 eV: the Volmer-Heyrovsky pathway with q = -1

Overall, comparison of HER mechanisms on A-TiO_2 (001) and (101) at pH = 7 for photocatalytic water splitting suggests that the Volmer-Heyrovsky mechanism dominates on both TiO_2 facets. The appropriate H* adsorption strength on A-TiO_2 (101) (in the rate-determining step) is predicted to result in more stable HER performance than on A-TiO_2 (001). It is reasonable to assume that the surface of A-TiO_2 (001) is composed of undercoordinated Ti_{5C} (among Ti atoms in A-TiO_2 (001)), which enhances the interaction with charged H* their dangling bond-like nature, acting as Lewis acid centers (electron acceptors). However, when TiO_2 exhibits p-type properties, the electron concentration is extremely low, thereby requiring higher adsorption energy, while the bond strength increases with the increase of the Fermi level. Since the Volmer step is the rate-determining step, it is expected that A-TiO_2 (001) has lower photocatalytic activity for HER in comparison to A-TiO_2 (101), which arises from the intrinsic surface coordination.

4.2.4 Computational Method

DFT calculations were performed using the Vienna *Ab initio* Simulation Package (VASP). The interaction between valence and core electrons was treated using the projector augmented wave (PAW) method.[107–109] The general gradient approximation (GGA) with the Perdew, Burke, and Ernzerhof (PBE) exchange-correlation functional was employed for the plane-basis wave expansion.[71,72] The kinetic energy cut-off was set to 400 eV, and the energy convergence criteria in the self-consistent field were set to 10^{-6} eV. All geometric structures were fully relaxed until the Hellman-Feynman forces approximated 0.1 eV A^{-1}. In the optimization of the cell parameters, a Gamma-centered *k*-point grids of 2 x 2 x 1 was used for Brillouin zone sampling.[110] The Hubbard U approximation (U_{3d} = 5 eV) term was included for the 3d orbital of Ti.[111,180] The supercell structures of anatase TiO_2 (101) and rutile (110) contain 48 Ti atoms and 96 O atoms in lateral dimensions of 10.92 x 15.14 x 26.49 Å and 11.83 x 12.99 x 29.00 Å. A vacuum region of 20 Å was introduced along the surface normal to avoid interactions between periodic slabs.

4.2.5 Conclusion

This work systematically examined the role of charge carrier potential in the calculation of the adsorption energies during photocatalytic redox reactions. The significant role of charge carriers in the catalytic activity has been often overlooked in previous DFT studies, making it challenging to understand the surface reaction mechanisms. By incorporating the carrier-driven potential into the theoretical framework, the driving force of charge carriers was quantified, and a simple and general strategy was suggested to calculate the adsorption energy of photocatalytic activity. Consequently, this approach helps resolve discrepancies in the explanation of facet- and phase-dependent photocatalytic activity of TiO_2.

Nevertheless, the current theory model still has limitations. The effect of charge carrier recombination and the proper consideration of the quasi-Fermi level must be considered to evaluate the photocatalytic activity. Overcoming these limitations will be necessary for establishing an advanced model of photocatalytic activity, thereby helping the rational design of promising photocatalysts.

Chapter 5

Validation of Theoretical Predictions through Experimental Observations

Experimental verification is crucial to extend the applicability of newly proposed theoretical models for understanding the catalytic efficiency. The proposed frameworks focus on surface reaction kinetics in semiconductors by considering the chemical potential of charge carriers in relation to electro- and photocatalytic activity. In this chapter, the model developed in this thesis undergoes experimental validation to evaluate its reliability and relevance.

Advancements in semiconductor thin film fabrication technologies have driven the need for new insights to provide a better understanding of surface reactions in thin film applications. Many applied metal oxide photocatalysts are employed as thin films, for which current standard theoretical approaches are not readily applicable. In addition, the proposed surface reaction mechanisms remain debated because many variables, such as the composition of thin films and the grain size governing their mechanism, have not been adequately considered. In this context, this chapter aims to elucidate light-driven surface reaction mechanisms near the thin film surfaces by considering the behavior of charge carriers depending on the grain size using the theoretical model introduced in Chapter 4.

Photocatalytic Activity of Grain Size-controlled Anatase TiO_2 Thin film Photoanodes: A Microscale Perspective

5.1 Introduction

Chemical vapor deposition (CVD) is a powerful technique for producing high-quality solid thin films as thin film morphologies, crystallinity, and growth rates can be precisely controlled.[181,182] This capability enables the fabrication of uniform thin films that exhibit distinct surface characteristics and catalytic activities. Indeed, CVD has been widely used to produce thin films of various semiconducting materials, such as TiO_2,[181] SnO_2,[183] Fe_2O_3,[184], CeO_2,[185] UO_2,[186] and ThO_2,[187] which are extensively used as photoelectrochemical catalysts.

With the increasing deployment of thin-film technologies, interest in understanding their surface reactions has also grown substantially.

In recent years, surface reaction phenomena in photo-driven catalysis have been actively investigated for both fundamental understanding and practical applications. Nevertheless, it has been very challenging to predict the catalytic reaction on semiconductors, primarily because the current standard adsorption energy calculations often overlook the changeable Fermi level. This limitation has been addressed in our previous work (Chapter 4.1),[38] which proposed a new theoretical framework and incorporated the role of charge carriers (Chapter 4.2),[31] thereby overcoming critical limitations in the study of surface reaction mechanisms in wide-band-gap semiconductors.

Another major challenge in predictability arises from the diverse morphologies of thin films, which makes it difficult to generalize their catalytic behavior. Previous studies have largely focused on nanoscale features (e.g., grain boundaries or surface roughness), while systematic interpretations at larger length scales (>100 nm) are still lacking. Therefore, a comprehensive understanding of morphological effects across different scales is essential for elucidating their role in surface reactions.

In this work, the morphology of anatase TiO_2 thin films was kinetically controlled by varying the precursor flux during CVD growth and subsequently evaluated their catalytic activity toward the oxygen evolution reaction (OER). A new theoretical model introduced in Chapter 4 is modified to understand the surface reaction of PEC applications. Furthermore, by constructing a contour map of the rate constant ratio for OER using DFT-computed energy profiles, it is highlighted the significant influence of thin film morphology, particularly grain size, on catalytic performance.

5.2 Characterization of TiO_2 thin films

The anatase TiO_2 (A-TiO_2) thin films were fabricated using a thermal chemical vapor deposition (CVD) process with titanium isopropoxide ($Ti(O^iPr)_4$, $Ti(OC_3H_7)_4$, TTIP). The deposition was performed for 2 hours on a fluorine-doped tin oxide (F:SnO_2, FTO) substrate maintained at a growth temperature of 500 ℃. The temperature of the precursor reservoir was 35 ℃. The chemical reaction of transformation of $Ti(O^iPr)_4$ into TiO_2 can be written as:[188]

$$Ti(O^iPr)_4 \rightarrow TiO_2 + 4C_3H_6 + 2H_2O$$

To control the morphology of TiO_2 thin films, the CVD process was carried out under reduced pressure conditions at 10^{-2} mbar and 10^{-6} mbar.

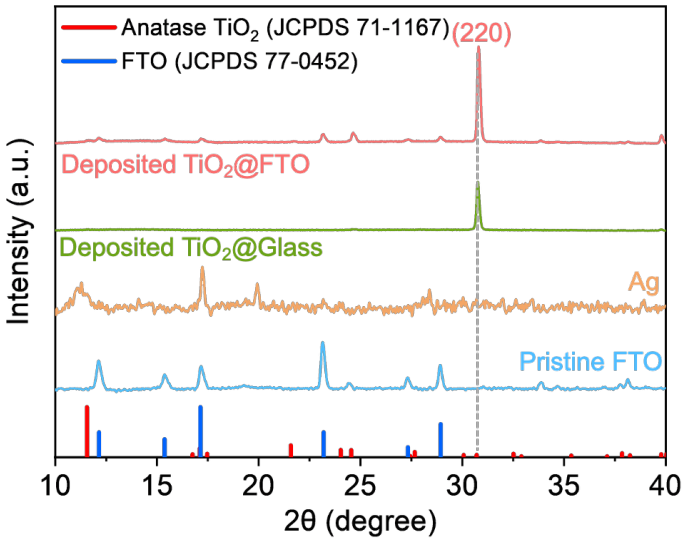

Figure 5.1 X-ray diffraction (XRD) measurements of deposited TiO_2 on FTO (under low pressure at 10^{-2} mbar), Ag paste on a glass, and pristine FTO substrate, respectively.

Thin film X-ray diffraction (XRD) measurements were conducted to determine the crystal structure of the prepared sample as shown in Figure 5.1. The diffraction pattern of A-TiO_2 thin film shows the A-TiO_2 crystal structure (JCPDS# 71-1167) and FTO (JCPDS# 77-0452). Following the literature data, the most intense peak at 30.7 º in the diffraction pattern of A-TiO_2 corresponds to the A-TiO_2 of (220) plane, showing a pronounced texturing in TiO_2 films.

Since the (220) plane of A-TiO_2 has been rarely reported as this facet is hardly formed due to high surface energy (~1.09 J m^{-2}), which is considerable higher than that of the most stable (101) facet (~0.44 J m^{-2}),[189,190] additional experiments were performed under identical conditions to rule out the possibility of experimental errors: (i) deposition of A-TiO_2 on a glass substrate under a low pressure of 10^{-2} mbar (ii) XRD measurement of silver (Ag) paste, applied on a glass substrate, considering that Ag paste was used beneath the FTO substrate during CVD process (iii) XRD measurement using another X-ray diffractometer with a Cu-Kα source. The comparisons of diffraction peaks from these trials, shown in Figure 5.1, confirm that the intense peak observed in the XRD pattern of the prepared sample (A-TiO_2 on FTO) originates from the deposited A-TiO_2 thin film. Due to the crystallinity of the samples, further experiments were performed with these samples produced by the CVD process.

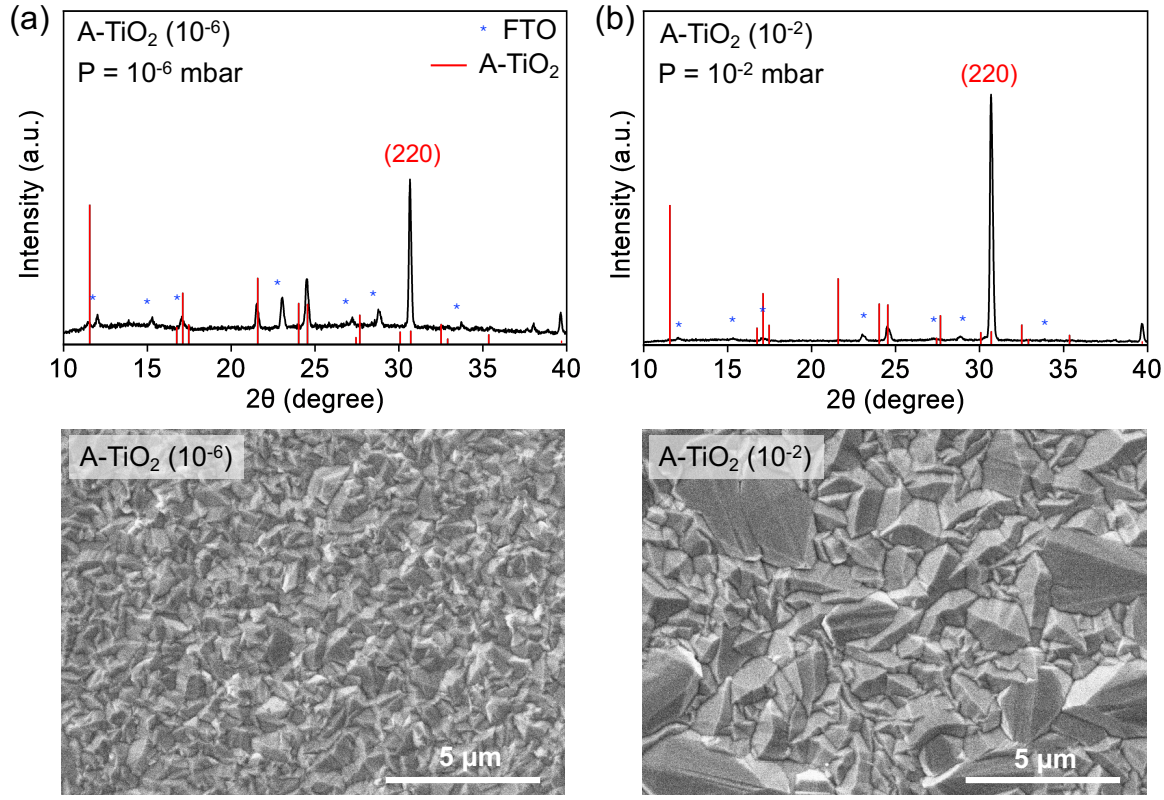

Figure 5.2 The XRD patterns, the images of top-view scanning electron microscopy (SEM) and energy-dispersive X-ray spectroscopy for (a) A-TiO_2 (10^{-6})) (b) A-TiO_2 (10^{-2}), respectively. P denotes the deposition pressure.

Thin film X-ray diffraction (XRD) patterns and the morphologies of A-TiO_2 (220) samples deposited under different pressures are shown in Figure 5.2. In this work, the prepared samples under low vacuum (10^{-2} mbar) and high vacuum (10^{-6} mbar) are denoted as A-TiO_2 (10^{-2}) and A-TiO_2 (10^{-6}), respectively. Figure 5.2 presents that both A-TiO_2 samples have the intense (220) diffraction peak at 30.7º, indicating that they have comparable crystallographic characteristics; therefore, the comparison of their surface morphologies is valid. The SEM images show that A-TiO_2 (10^{-6}) and A-TiO_2 (10^{-2}) have a microscale-grain size that is larger than 100 nm, especially A-TiO_2 (10^{-6}) fabricated under high vacuum (10^{-6} mbar) has much bigger average particle size than that of A-TiO_2 (10^{-2}). It can be predicted that the kinetic control of gas-phase precursor flows affects the grain size, resulting from the competing reaction between nucleation and coalescence. During the CVD process, the thin film is growing via nucleation, growth, and coalescence by heterogeneous reactions between the gas phase of reactants and the substrate surface.[182] Nucleation and coalescence are competing processes that depend on the flux of gas-phase precursors. Classical mean-field nucleation theory gives the

correlation between the saturated number density of stable islands (n_x) and the flux (F) as follows:[191]

$$n_x \propto \left(\frac{D}{F}\right)^{-\chi} \tag{5.1}$$

where the scaling exponent, $\chi = i/(i+2)$, in which i denotes the critical cluster size. D is the surface diffusion constant, and F is the flux of atoms. It means that when the flux of precursors increases under high vacuum, island density increases, thereby making nucleation kinetically preferred over coalescence. In contrast, the surface migration of single adatoms can occur faster, allowing adatoms to diffuse and form larger grain sizes, which then grow. The gas-phase precursor produces a seed on the substrate rather than coalescence.

5.3 PEC measurement

The photoelectrochemical (PEC) reaction was performed using the three-electrode system with a deposited TiO_2 thin film (A-TiO_2) on FTO, Ag/AgCl, and platinum (Pt) wire as the working, reference, and counter electrodes in 0.5 M Na_2SO_4 electrolytes (pH = 5.89), respectively. (Figure 5.3 (a))

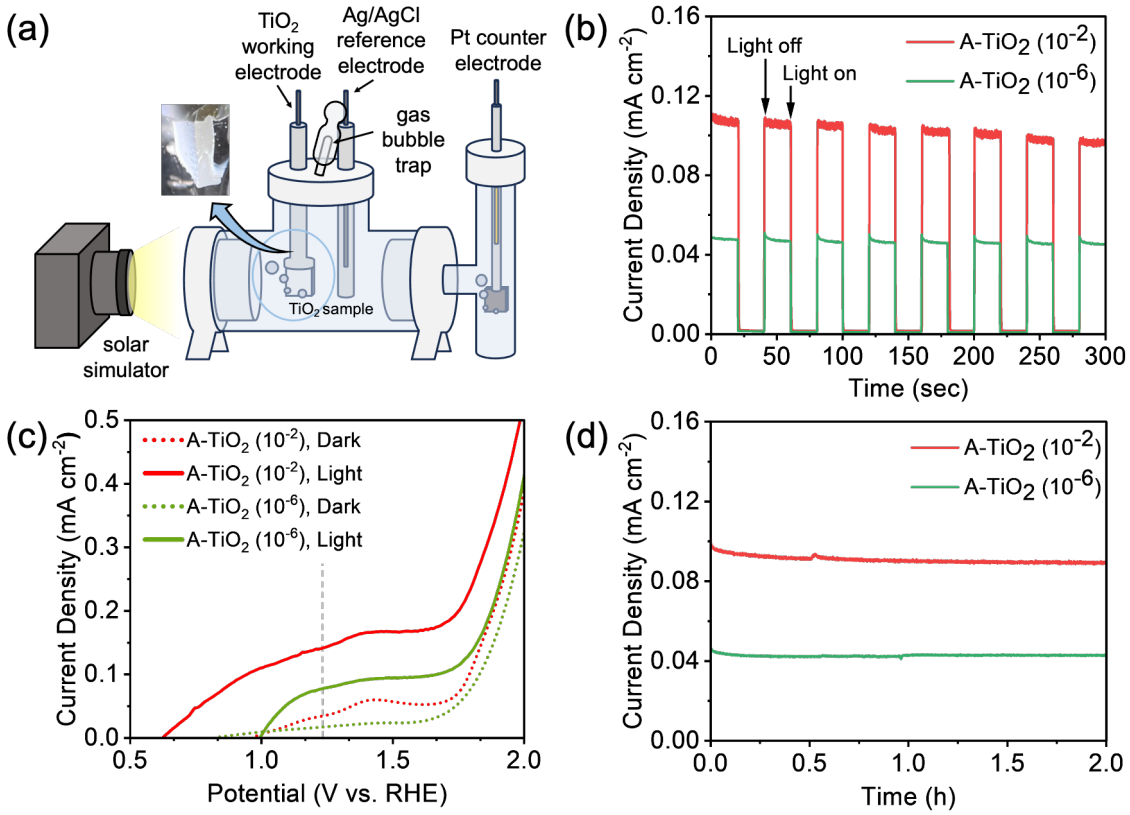

Figure 5.3 (a) Schematic illustration of three-electrode system and (b-d) are PEC performance of A-TiO_2 photoanode of A-TiO_2 (10^{-6}) and A-TiO_2 (10^{-2}) (b) Linear-Sweep Voltammograms (LSV) curves under AM 1.5 G irradiation in 0.5 M Na_2SO_4 solution with a scan rate of 10 mV s^{-1} (c) The transient photocurrent density responses of the photoanodes versus time at 1.23 V (vs. RHE) under chopped light illumination (d) Stability test: Long duration PEC measured *i*-t curves of A-TiO_2 (10^{-6}) and A-TiO_2 (10^{-2}) using the solar simulator at 1.23 V (vs. RHE) in a 0.5 M Na_2SO_4 electrolyte without an on/off switch with continuous measurement.

In Figure 5.3 (b), the photocurrent density of A-TiO_2 (10^{-6}) is 0.14 mA cm^{-2}, which is approximately 1.8 times higher than that of A-TiO_2 (10^{-2}) of 0.078 mA cm^{-2} at 1.23 V_{RHE}. Such low photocurrent densities of pristine TiO_2 are consistent with previous reports and are therefore regarded as reasonable in this work. Typically, pristine TiO_2 photoanodes exhibit photocurrent densities around 0.1–0.3 mA cm^{-2} at 1.23 V vs RHE under standard AM 1.5G illumination, as frequently reported in the literature.[192,193] Transient photocurrent response measurements were carried out under chopped light illumination at 1.23 V_{RHE}. (Figure 5.3 (c))

All photoanodes exhibit a fast, sensitive, and reproducible photocurrent response upon light illumination, indicating that the photogenerated holes can be efficiently extracted from A-TiO_2 (220) for rapid oxygen evolution. In addition, the steady tests indicate that all photoanodes provide good stability (Figure 5.3 (d)). The PEC measurements show that A-TiO_2 with a small grain size (A-TiO_2 (10^{-6})) has a higher PEC performance compared to A-TiO_2 with a big grain size (A-TiO_2 (10^{-2})), indicating a correlation between a grain size and photocatalytic reactivity.

5.4 Theoretical Model and DFT calculations

Photoelectrochemical water splitting combines aspects of both electrolysis and photocatalysis. A PEC cell consists of a semiconductor photoelectrode (either a photoanode or a photocathode) and a counter electrode immersed in an electrolyte. In the case of a photoanode, photoexcited holes migrate to the electrode surface, where they oxidize water to produce oxygen. The excited electrons travel through an external circuit to the photocathode, where they reduce protons to generate hydrogen.

In the photoelectrochemical reactions, an external circuit affects the transport and potential of charge carriers; Thus, the additional contribution of an applied bias to charge carrier migration should be accounted for. In Chapter 4.2, the equation of Gibbs free adsorption energy for the photocatalytic surface reaction in a semiconductor is introduced, which was given as:

$$\Delta G_{ads} = \Delta E_{ads} + \Delta ZPE + \int C_p dT - T\Delta S + \Delta G_{pH} + q(\varepsilon_F + E_{VBM}) + n\Delta V_{redox} + m(\Delta V_{h^+} - \Delta V_{e^-}) \quad (5.2)$$

where ΔE_{ads}, ΔZPE, $\int C_p dT$, and ΔS are the binding energy of OER intermediates, the change of zero-point energy, enthalpy, and entropy. ΔG_{pH} is the pH-dependent contribution to the reaction free energy, expressed as $-nk_BTln10pH$ (n is the number of transferred protons). q is the charge state of adsorbates, ε_F is the Fermi level that ranges over the band gap of a material (TiO_2 in this chapter), and E_{VBM} is the DFT-computed eigenvalue of the VBM energy level of the slab with adsorbates, respectively.

ΔV_{h^+} and ΔV_{e^-} in Eq (4.2.1) are the energies required for the hole carrier to oxidize the negatively charged adsorbates (q = -1) and that for the electron carrier to reduce the positively charged adsorbates (q = +1), respectively, and m is the number of required holes or electrons for neutralization. In addition, the terms neU and eU_{h^+,e^-} are added to consider the effect of an external bias on the surface reaction in Eq (5.2), therefore, the equation of Gibbs free adsorption energy of photoelectrochemical reactions is defined as,

$$\Delta G_{ads} = \Delta E_{ads} + \Delta ZPE + \int C_p dT - T\Delta S + \Delta G_{pH} + q(\varepsilon_F + E_{VBM}) + n\Delta V_{redox} + m(\Delta V_{h^+} - \Delta V_{e^-}) - neU + me(U_{h^+} - U_{e^-}) \quad (5.3)$$

The term neU is an applied potential, where U is the electrode potential. n in Eq (5.3) is the number of transferred protons and charge carriers. As mentioned above in Chapter 4.2, now two additional reaction steps should be considered: (i) *ads'-mediated step (ii) $*ads^-$ or $*ads^+$-mediated step. Especially, in the case of $*ads^-$ or $*ads^+$-mediated step, an external bias influences the charge carriers transport involved in the neutralization of the charged adsorbates. In this regard, mU_{h^+} and mU_{e^-} are considered to promote the neutralization, where m is the number of charge states of the charged adsorbate.

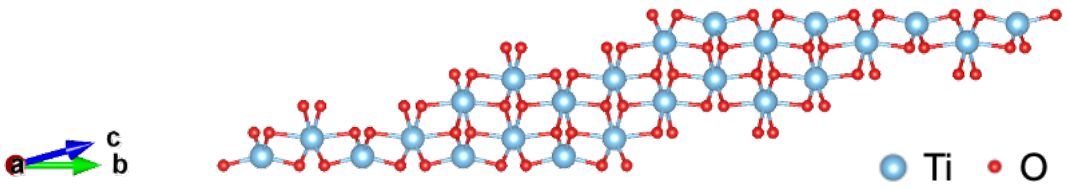

Figure 5.4 The supercell of A-TiO_2 (110) used for DFT calculations. Blue and red balls represent Ti and O atoms, respectively.

DFT calculations were performed to gain further insights into the photocatalytic phenomena on A-TiO_2 associated with grain size. In the DFT calculations, the A-TiO_2 (110) plane was employed, since it is crystallographically compatible with the (220) plane according to the geometric relation as follows:

$$d_{220} = \frac{1}{2} d_{110} \quad (5.4)$$

where d is the interplanar spacing. The supercell of A-TiO_2 (110) is shown in Figure 5.4.

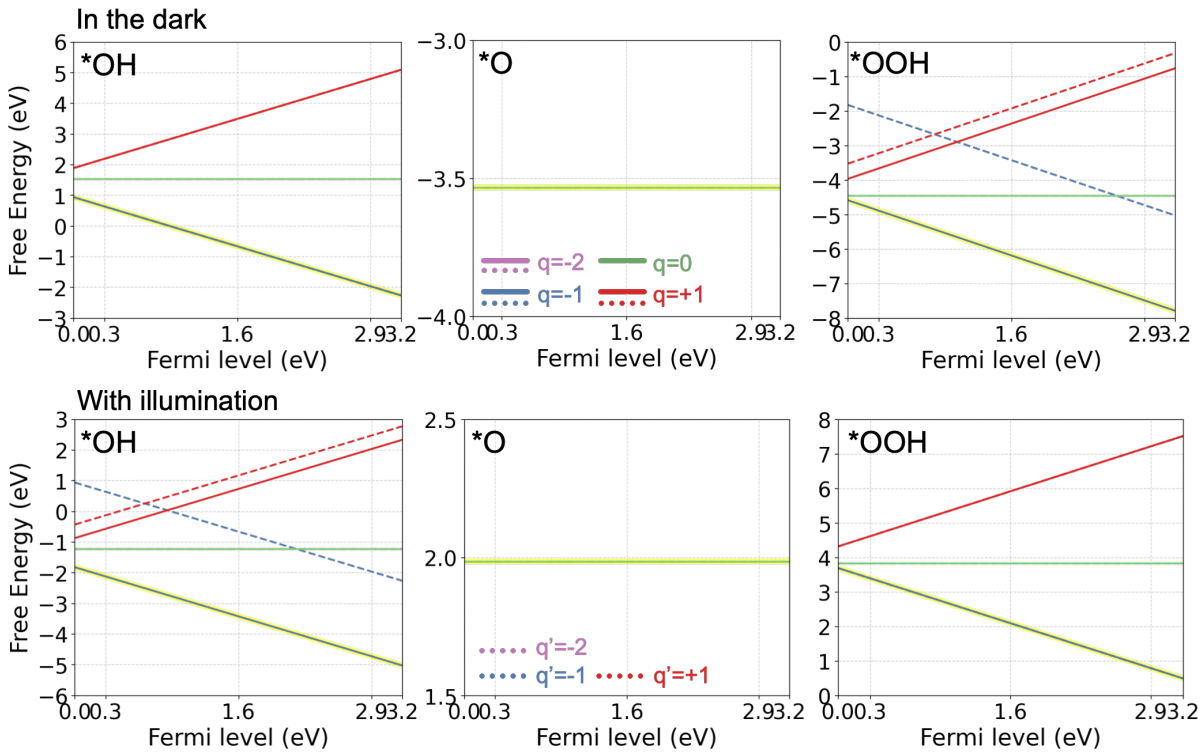

Figure 5.5 The graphs of the Gibbs free adsorption energy of OER intermediates (*OH, *O, and *OOH) under dark (in the dark) and illuminated (with illumination) condition. The solid line and dashed line are the charge states of adsorbates that are not involved (q)/involved (q') in the neutralization. The purple, blue, green, and red solid lines are the charge states q = -2, -1, 0, and +1, respectively. The purple, blue, and red dashed lines are the charge states of the adsorbates with charge neutralization q' = -2, -1, and +1, respectively. The highlighted lines indicate the thermodynamically more favorable energy pathways.

The adsorption energies of OER intermediates on A-TiO_2 (220) were calculated using Eq (5.3) with the consideration of charge carrier contributions to the photocatalytic redox reaction. Figure 5.5 shows the Gibbs free adsorption energies of OER intermediates as a function of the Fermi level of A-TiO_2 (220) under two conditions: (i) without illumination (dark condition, used as a reference) and (ii) under illumination. Here, q is the charge state of adsorbates (*OH: q = -1, 0, +1, *O: q = -2, -1, 0, +1, and *OOH: q = -1, 0, +1), and q' indicates the charge state of the adsorbates prior to neutralization. If the adsorption energy of q' is thermodynamically more favorable than that of q, an additional reaction step will be involved in the OER pathway. For *O adsorption, adsorption of *O charged with q = -2, -1, and +1 are not thermodynamically favored, therefore the adsorption energies of $*O^{2-}$, O^- and O^+ are not considered as a possible reaction pathway. In addition, negatively charged (q = -1) $*OH^-$ and $*OOH^-$ are thermodynamically preferred regardless of the Fermi level. Accordingly, the predicted reaction

pathway of photoelectrochemical OER on A-TiO_2 (220) at pH = 5.89 with an applied bias (U) of 1.23 V under illumination as a function of the Fermi level of A-TiO_2 (220), is summarized as follows:

$$(i)\ H_2O\ (l) \rightarrow *OH^- + H^+$$

$$(ii)\ *OH^- + 2h^+ \rightarrow *O + H^+$$

$$(iii)\ H_2O\ (l) + O* \rightarrow *OOH^- + H^+$$

$$(iv)\ *OOH^- + 2h^+ \rightarrow O_2\ (g) + H^+$$

The suggested reaction pathway of PEC OER on A-TiO_2 (220) indicates that the additional reaction steps associated with the neutralization of charged adsorbates by surface charge carriers are not involved in the overall PEC OER process.

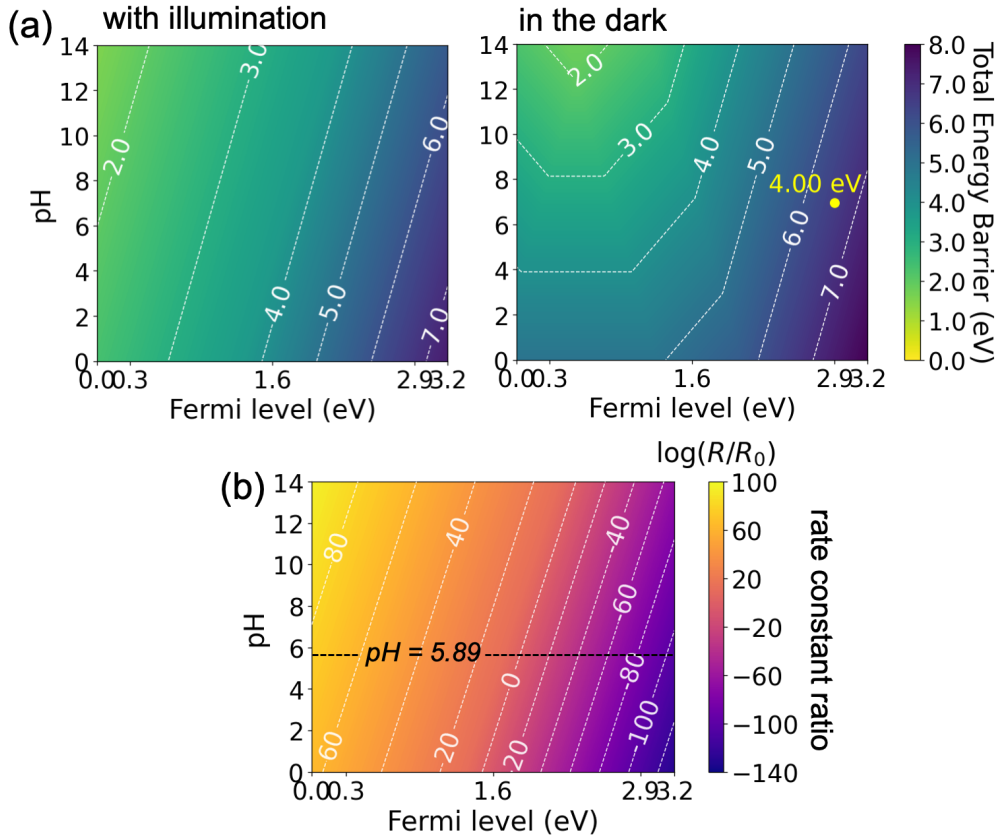

Figure 5.6 DFT-computed contour maps of (a) the total energy barrier and (b) the rate constant ratio (on a logarithmic scale) of photoelectrochemical OER relative to the dark condition, plotted as functions of Fermi level (eV) and pH. The yellow dot indicates the total energy barrier of OER under dark conditions (in the dark) at the flat-band condition of A-TiO_2 (220) (pH = 5.89, applied bias = 1.23 V). The contour lines and numbers in the graph denote (a) the magnitude of the total energy barrier and (b) the logarithmic value of the rate constant ratio, respectively.

The contour maps of PEC OER as functions of the Fermi level and pH, under illumination and in the dark, are shown in Figure 5.6 (a). The total energy barrier of PEC OER on A-TiO_2

(220) is lower under alkaline conditions than under acidic conditions. With illumination, the total energy barrier decreases as the Fermi level of A-TiO_2 (220) decreases, indicating that a high carrier concentration is beneficial for PEC OER. In contrast, under dark conditions (in Figure 5.6 (a) in the dark), it is predicted that the total energy barrier is the lowest when the Fermi level of A-TiO_2 (220) is positioned near the mid-gap.

To further understand the dependence of photocatalytic OER activity on the surface Fermi level and pH, the contour map of the rate constant ratio with and without illumination (in the dark) ($\frac{R}{R_0}$) is presented in Figure 5.6 (b). The ratio is obtained by comparing the total energy barrier with illumination ($\Delta E_{barrier}$) and without illumination ($\Delta E^0_{barrier}$) using Eq (5.5),

$$\frac{R}{R_0} = \exp\left(-\frac{\Delta E_{barrier} - \Delta E^0_{barrier}}{kT}\right) \quad (5.5)$$

Thus, $\frac{R}{R_0}$ quantifies the relative enhancement or suppression of PEC OER due to illumination and the favored reaction condition can be predicted.

In a contour map of the rate constant ratio ($\frac{R}{R_0}$), when the calculated logarithmic value is negative ($\log\left(\frac{R}{R_0}\right) < 0$), it implies that the PEC OER activity under illumination is lower compared to that in the dark. In addition, brighter areas correspond to higher PEC OER activity. The reaction conditions correspond to pH = 5.89 (0.5 M Na_2SO_4) with an applied bias of 1.23 V; therefore, the calculated reactivity is evaluated under these conditions. For reference, $\Delta E^0_{barrier}$ is the value of the total energy barrier at the flat-band condition of A-TiO_2 (220) at pH = 5.89 with an applied bias of 1.23 V, which is indicated by the yellow dot in Figure 5.6 (a) (in the dark).

It is predicted that the performance of PEC OER on A-TiO_2 (220) is higher when the Fermi level of A-TiO_2 (220) is low under alkaline conditions, whereas it is suppressed under acidic conditions. This trend can be explained by the fact that, at a low Fermi level of A-TiO_2 (220), a larger population of hole carriers is available. A similar effect is observed in p-n junctions such as TiO_2/Cu_2O heterojunction structures for PEC OER. In addition, at pH 5.89, it is observed that the PEC OER activity starts to decrease when the Fermi level of A-TiO_2 (220) approaches approximately 2.1 eV. Under these conditions, adjusting the Fermi level to this range, for example, through coupling with metallic cocatalysts such as NiFe may result in an electrochemical OER more favorable than the PEC OER process.[194]

For photocatalytic surface reactions, there are three determining factors: (i) charge-carrier transport efficiency, (ii) surface reaction rate, and (iii) ion transport efficiency.[195] In

photoelectrochemical OER, efficient hole carrier transport is crucial to initiate the reaction. At the nanoscale, which is the typical size range considered in many previous works, n-type TiO_2 nanoparticles are particularly suitable because band bending can occur within a short distance (a few nanometers), and a higher oxygen-vacancy concentration enhances OER activity. Conversely, when the oxygen-vacancy concentration is low, the depletion region width can exceed the particle radius, preventing sufficient band bending and thereby hindering hole-carrier transport.

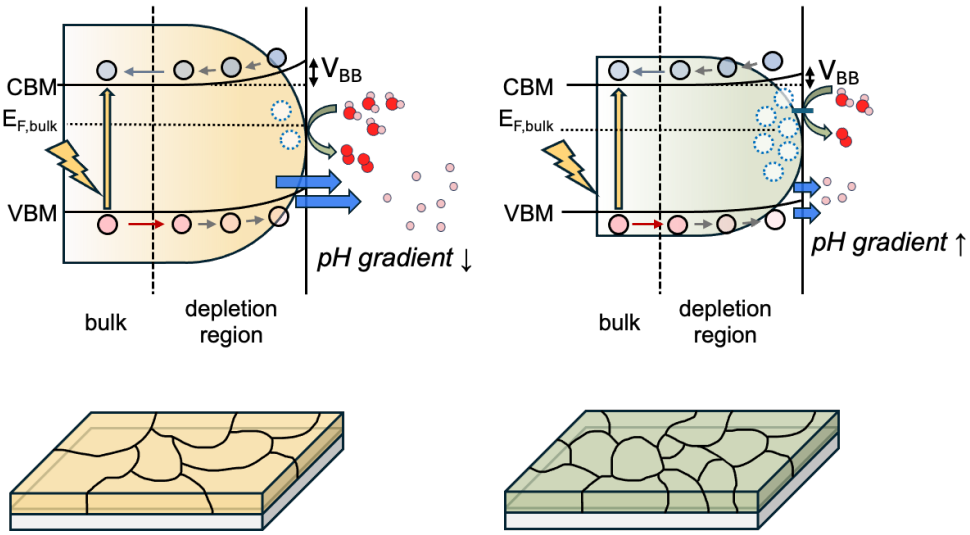

Figure 5.7 Schematic illustration showing the effect of grain size on interfacial band bending (V_{BB} is the magnitude of band bending), electric field, and local pH distribution in microscale n-type TiO_2. Larger grains (left), with reduced surface defects maintain uniform band bending and strong interfacial fields, facilitating efficient proton migration and lower pH gradients. In contrast, smaller grains (right), with defect-induced Fermi level pinning exhibit weakened electric fields, proton accumulation, and higher local pH gradients. Light blue and pink balls are photogenerated electrons and holes, respectively. The dashed circular line is surface defect, and blue arrows represent electric fields near the surface. Red and light pink balls denote oxygen and hydrogen atoms, respectively.

At the microscale, however, where the grain size is much larger (>100 nm), the situation differs fundamentally. The depletion region width becomes much smaller than the particle size, and the band bending becomes shallower but extends more deeply into the bulk. The broader depletion region and weakened built-in field hinder the drift of photogenerated holes toward the surface. Nevertheless, the overall OER rate is limited by sluggish surface reaction kinetics rather than by charge transport. Therefore, in this case, the nanoscale effect is substantially reduced, and the electronic behavior must be interpreted from a different perspective. Sing et

al. emphasized that in pelletized TiO_2 with microscale grains, charge transport and PEC performance should be interpreted differently from nanoscale system where surface effects dominate.[196]

The experimental observations show that (A-TiO_2 (10^{-6})) with smaller grains exhibited lower photocurrent and OER activity than (A-TiO_2 (10^{-2})), indicating that the surface reactivity trend is inverted compared with nanoscale systems. Because all samples lie at the microscale (grain radius >> depletion region width), the photocurrent is primarily governed by surface reaction kinetics rather than by hole carrier transport limitations.

The smaller-grained TiO_2 (A-TiO_2 (10^{-6})) exhibits a higher density of surface defects, which enhances adsorption strength but simultaneously induces surface potential pinning and weakens the interfacial electric field. Negatively charged intermediates (e.g., $*O^-$, $*OOH^-$), which are predicted to be thermodynamically preferred for the PEC OER process on A-TiO_2 (220), are energetically stabilized by the interfacial electric field of n-type TiO_2. However, excessive stabilization at defect-rich surfaces leads to overly strong adsorption, making desorption of $*O^-$ or $*OOH^-$ difficult. According to the Sabatier principle, such over-binding increases the kinetic barrier of the rate-determining step, resulting in a lower surface reaction rate constant.[197,198] In contrast, the larger-grained TiO_2 (A-TiO_2 (10^{-2})), which exhibits clearly faceted grains with reduced grain-boundary density compared to the smaller-grained film, maintains optimal adsorption strength and preserves a stronger interfacial electric field, thereby leading to superior OER activity even among micro-sized grains.

Furthermore, although band bending is no longer the primary factor determining hole transport at this microscale, the interfacial electric field associated with it can still impact ion transport efficiency near the surface.[199] During OER, the generated protons experience electrostatic repulsion from the positively charged surface due to surface band bending;[200,201] hence, a stronger interfacial field in large-grained TiO_2 promotes more efficient proton removal or migration, mitigating local charge accumulation and pH gradients, and thereby facilitating faster surface reaction kinetics.

This size-dependent inversion, opposite to the nanoscale expectation, is consistent with our theoretical prediction that n-type TiO_2 intrinsically displays a low surface reaction rate and that vacancy-rich surfaces are not necessarily beneficial when carrier transport is no longer rate-limiting. Moreover, this observation is consistent with the recent study by Kwon et al., showing that the optimal Fermi level shifts from higher to lower values as $BiVO_4$ transitions from nano- to microscale, indicating a reversed size-dependent trend.[202] This interpretation is further supported by the predicted trend shown in the contour map in Figure 5.6 (b), which clearly

demonstrates that the reactivity of heavily n-type TiO_2 is lower than that of lightly doped n-type TiO_2.

5.5 Conclusion

In this work, anatase TiO_2 thin films were fabricated as photoanodes for photoelectrochemical (PEC) water oxidation. The morphology of the thin film was kinetically controlled by deposition under different reduced pressures to investigate how grain size governs the PEC oxygen evolution reaction (OER) activity from a microscale perspective. The fabricated thin film has the (220) main plane of anatase TiO_2 with high crystallinity, and therefore, the samples were chosen for further PEC applications.

The results show that anatase TiO_2 (220) with smaller grains has approximately half the photocurrent density of larger grains, indicating that larger grain sizes lead to superior OER performance. According to the results of the proposed theoretical model, which accounts for the contribution of hole carriers to photocatalytic reactions for the calculation of adsorption energies, the PEC reactivity will be enhanced as the Fermi level of A-TiO_2 (220) shifts toward p-type.

All samples fabricated in this work are at the microscale; the reactivity of PEC OER is inverted compared to the nanoscale-sized samples due to the different determining factors. Due to the large depletion width, hole transport toward the surface is not efficient; therefore, the surface reaction rate is the main determining factor for the reactivity. In this case, the built-in electric field becomes weaker and extends more deeply into the bulk, reducing field-assisted charge separation but enhancing the role of surface adsorption and desorption kinetics in determining overall activity.

This elucidation of the surface reaction mechanisms in kinetically controlled thin film growth highlights a microscale-specific perspective that differs fundamentally from the conventional nanoscale interpretation. Such a framework provides new insights into clarifying the reaction mechanisms for future thin film applications. Nevertheless, experimental verification will be necessary to examine the behavior of surface intermediates, and quantitative theoretical studies should be performed in future work.

5.6 Experimental Section

5.6.1 Fabrication of anatase TiO_2 thin films

Anatase TiO_2 (A-TiO_2) thin films were grown on fluorine-doped tin oxide (F:SnO_2, FTO) coated glass substrates (3 mm thickness) by chemical vapor deposition (CVD) technique. The FTO substrates were cleaned by ultrasonic cleaning in soap water, deionized water, acetone, ethyl acetate, and isopropyl alcohol in sequence for 10 minutes each and dried using a nitrogen stream.

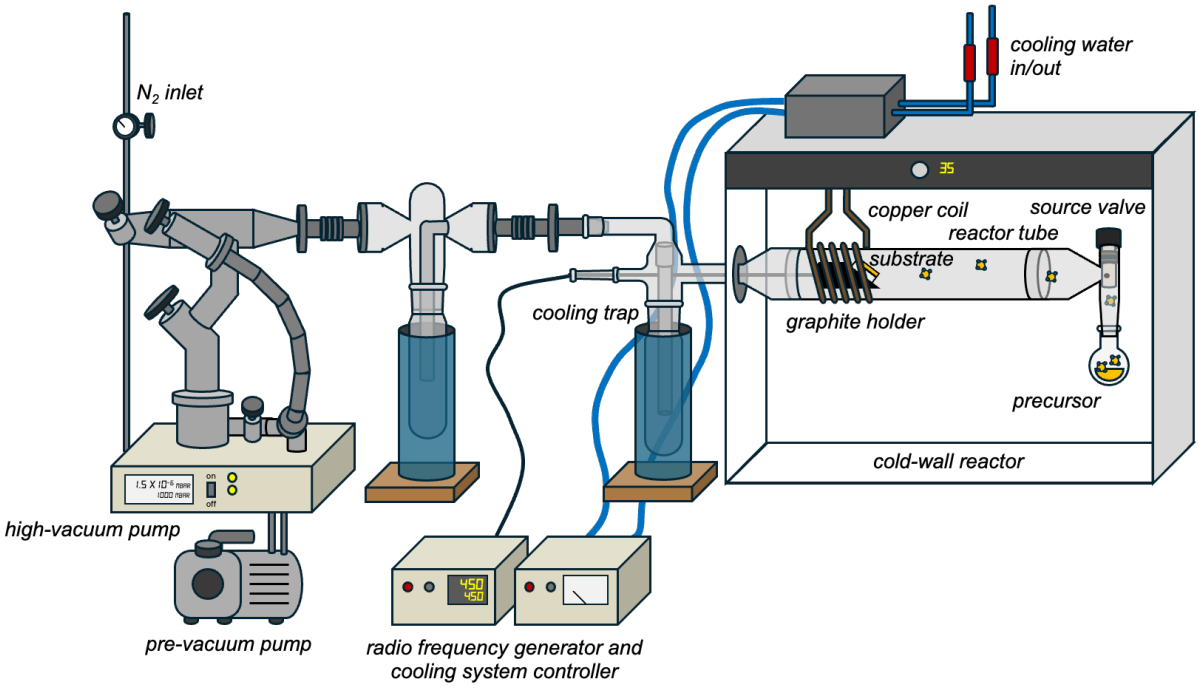

Figure 5.7 Schematic illustration of a horizontal cold-wall chemical vapor deposition (CVD) system.

Depositions of TiO_2 thin film were conducted in a horizontal cold-wall chemical vapor deposition (CVD) reactor equipped with an inductive heating system and cooling traps as shown in Figure 5.7. FTO substrate (10 mm x 15 mm) was placed on a graphite susceptor and heated inductively. The deposition temperature is 500 °C. Titanium isopropoxide ($Ti(O^iPr)_4$, $Ti(OC_3H_7)_4$, TTIP, TCI chemicals, ≥ 80%) was introduced into the CVD reactor equipped with a glass tube at 35 °C in a 25 mL flask and deposited under pressure at 10^{-2} mbar (low-vacuum condition) and 10^{-6} mbar (high-vacuum condition) for 2 hours. Calcination was subsequently done in an oven (atmospheric conditions) at 500 °C for 2 hours.

5.6.2 PEC measurements

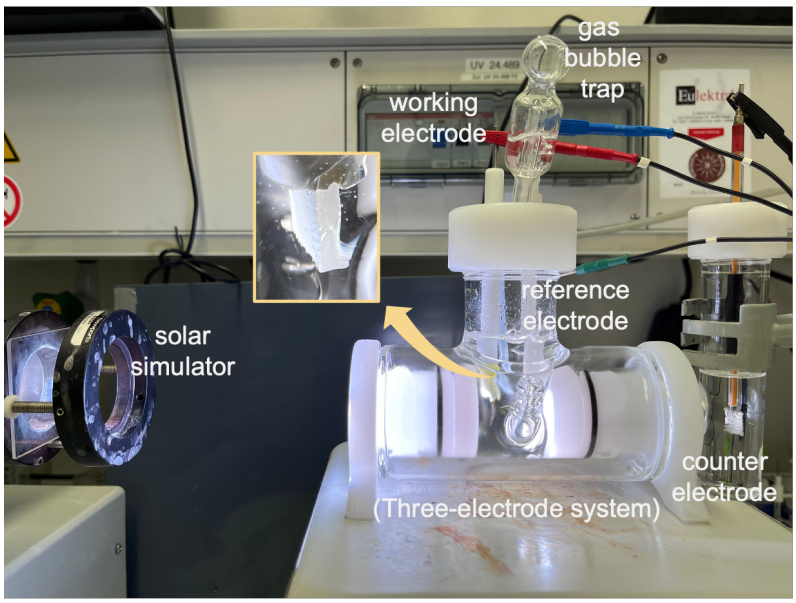

Figure 5.8 Photograph of a three-electrode system and A-TiO_2 (220) sample during OER, highlighted by the yellow box.

PEC measurements were conducted using a potentiostat (Palm Sens) with a three-electrode system including the photoanode as the working electrode, an Ag/AgCl (KCl sat.) electrode as the reference electrode, and a platinum wire as the counter electrode. Simulated light with 1 Sun intensity (AM 1.5, 100mW cm^{-2}) was irradiated on the front side of the photoanode by a solar simulator during the measurement, where the photoanode was mounted on a homemade quartz reactor. (Figure 5.8) Neutral electrolytes were prepared by using 0.5 M Na_2SO_4 in deionized water. (pH = 5.89). Linear sweep voltammetry (LSV) was measured within the potential range of 0.5 – 2.0 V vs. RHE at a scan rate of 10 mV s^{-1}. The transient photocurrent responses (*i*-t curves) were measured under chopped-light irradiation with light on/off cycles of 20 s for a total duration of 300 s at a fixed electrode potential of 1.23 V vs. RHE. Stability tests of the photoanode were conducted for 2 hours using the bulk electrolysis method with a constant potential of 1.23 V vs. RHE. The electrode potentials vs. Ag/AgCl were converted to the reversible hydrogen electrode (RHE) scale according to the Nernst equation:

$$E_{RHE} = E_{Ag/AgCl} + 0.059pH + E^{\circ}_{Ag/AgCl} \quad (5.6)$$

where $E^{\circ}_{Ag/AgCl}$ was 0.197 V at 25 °C.

5.6.3 Characterization

X-ray Diffractometry (XRD)

The X-ray diffraction (XRD) analysis of polycrystalline thin films was performed using a STOE-STADI MP diffractometer operated in reflection mode with Bragg-Brentano geometry, using a Mo Kα excitation source (λ = 0.7093 Å) equipped with a Mythen 1K detector.

Scanning Electron Microscopy (SEM)

The morphology and bulk elemental distribution were analysed using a Nova Nano SEM 430 field emission scanning electron microscope (FESEM).

5.6.4 Computational Methods

DFT calculations were carried out using the Vienna *Ab initio* Simulation Package (VASP). The interaction between valence and core electrons was treated using the projector augmented wave (PAW) method.[107–109] The general gradient approximation (GGA) with the Perdew, Burke, and Ernzerhof (PBE) exchange-correlation functional was employed for the plane-basis wave expansion.[71,72] The kinetic energy cut-off was set to 400 eV, and the energy convergence criteria in the self-consistent field were set to 10^{-6} eV. All geometric structures were fully relaxed until the Hellman-Feynman forces approximated 0.1 eV A^{-1}. In the optimization of the cell parameters, a Gamma-centered *k*-point grids of 2 x 2 x 1 was used for Brillouin zone sampling.[110] The Hubbard U approximation (U_{3d} = 5 eV) term to modify the self-interaction error and enhance the description of the on-site Coulomb interactions was included for the 3d orbital of Ti.[111,180] The supercell structures of anatase TiO_2 (110) contain 48 Ti atoms and 96 O atoms in lateral dimensions of 10.86 x 19.37 x 54.26 Å. A vacuum region of 20 Å was added perpendicular to the substrate surface to avoid interactions between periodic slabs. The contour maps were generated using a self-written Python code.

Chapter 6

Summary and Outlook

Thermodynamics combined with computational methods provides new insights into catalytic reactions and mechanisms, thereby contributing to the advancement of materials. Especially, the current standard computational hydrogen electrode (CHE) approach contributes to the design of metallic materials.

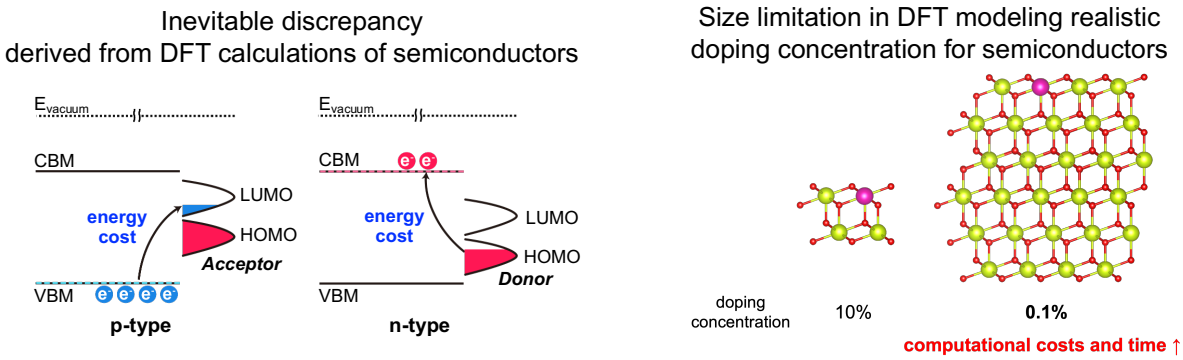

Scheme 6.1 Schematic illustration of the limitation of the current CHE approach.

However, using the CHE approach, modelling the catalytic reactions in wide band gap semiconductors has been limited because of: i) large discrepancies between experimental observations and theoretical predictions of semiconducting materials, ii) strong dependence of catalytic activities of wide band gap semiconductors on several factors such as defect concentration, cocatalyst particle size, work function of cocatalysts, surface coverage, geometry, and so on, iii) most importantly, the size limitation for DFT calculations. When modeling low doping concentrations, which is a common defect engineering strategy for semiconductors, we need a large supercell. However, it is not feasible to optimize such a large supercell because it is both computationally expensive and time-consuming.

$$\Delta G = \sum_{products,i} n_i \mu_i - \sum_{reactants,j} n_j \mu_j \pm n_e \mu_e - T\left(\sum_{products,k} \Delta S_k - \sum_{reactants,m} \Delta S_m\right)$$

chemical potential of products and reactants — *chemical potential of electrons* — *vibrational entropy (thermal effect)*

Scheme 6.2 The Gibbs free energy equation with the newly considered chemical potential of electrons and vibrational entropy contribution.

To address this issue, in this work, the chemical potential of electrons ($n_e\mu_e$ in Scheme 6.2) was explicitly considered through the Fermi level position, as the surface reaction kinetics are governed by charge transfer. This approach helps reduce discrepancies in the calculation of adsorption energies. In addition, the vibrational entropy contribution ($T\sum_{products,k}\Delta S_k$ for products and $T\sum_{reactants,m}\Delta S_m$ for reactants at a finite temperature T) was included to elucidate the temperature-dependent reaction selectivity of CeO_2 (used here as a prototype material) within a specific thermal window, relevant to fuel cells operating across a wide temperature range.

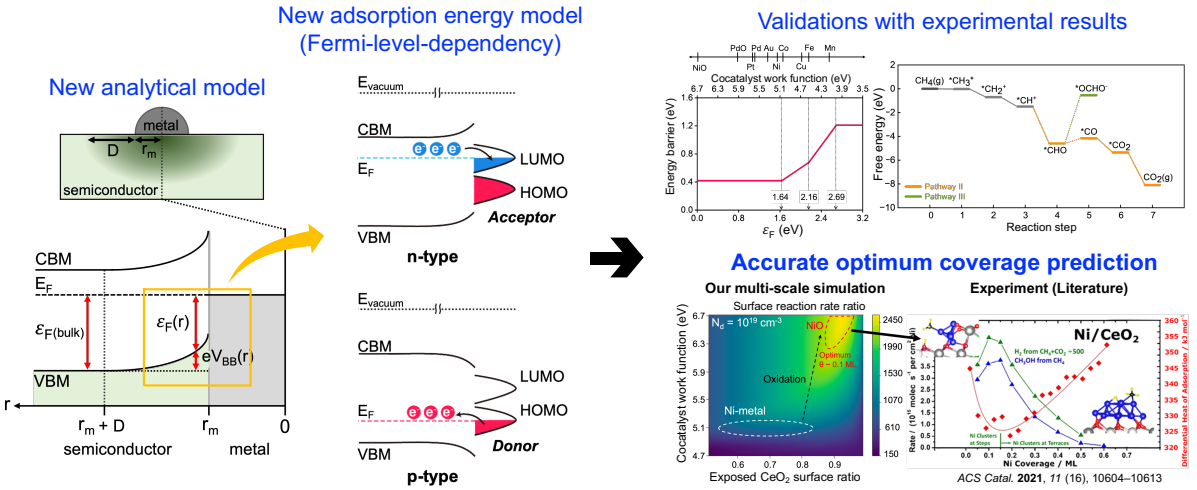

Scheme 6.3 Schematic explanation of the analytical model introducing the Fermi level dependency of the adsorption energy theoretical model and its validation with experimental observations.

Furthermore, by systematically considering the governing factors of catalytic activity, the newly established analytical model generates a contour map capable of predicting various doping concentrations, oxygen vacancy concentrations, cocatalyst particle sizes, and cocatalyst species. The results are consistent with experimental data reported in the literature, thereby supporting the reliability of the analytical model, thereby supporting not only the reliability but also the applicability of the analytical model to other semiconductor-based catalytic systems.

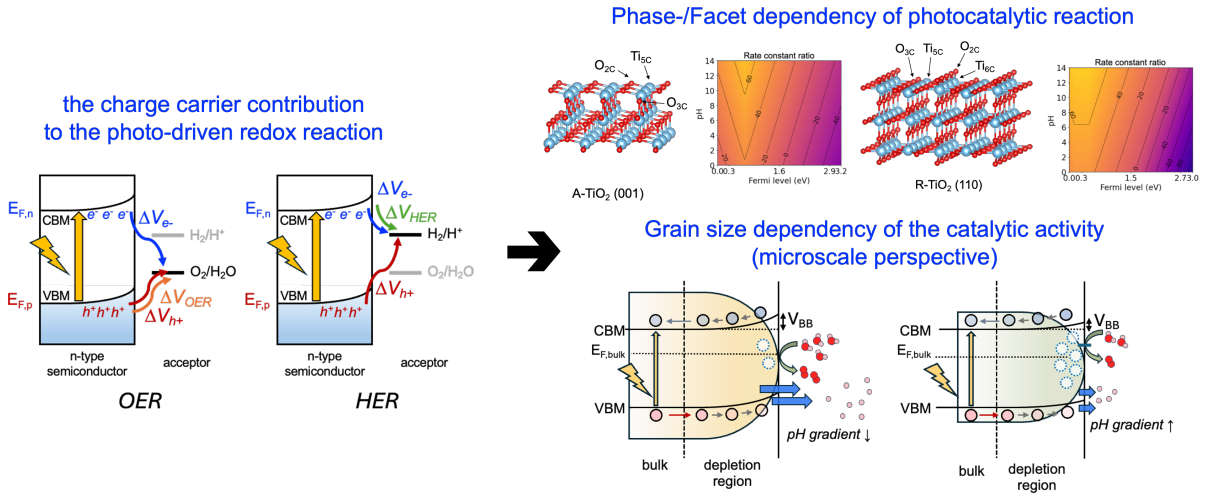

Scheme 6.4 Applicability of the theory model for surface and morphology-controlled materials for complex photocatalytic reactions.

Further, this theoretical model can be expanded to photocatalysis as most of photocatalysts are semiconducting materials. However, the inherent complexity of photocatalytic processes makes it difficult to predict the photocatalytic activity. The reasons can be summarized as follows: i) limitations in elucidating the surface reactions or catalytic phenomena of semiconductors, and ii) the fact that most theoretical frameworks neglect the important contribution of charge carriers to photocatalytic reactions. In this context, the new theoretical model introduced in Chapter 4.1 was further modified to account for the contribution of charge carrier to the activity.

In this study, a new theoretical method to consider the charge carrier contributions to the photocatalytic activity in the adsorption energy calculation is suggested, therefore simplifying and advancing the conventional method to evaluate the photocatalytic activity by the adsorption energy. Furthermore, by using this theoretical framework, the dependency of the photocatalytic activity on grain size has been elucidated. This study clearly demonstrated that the photocatalytic activity of anatase TiO_2 strongly depends on grain size: thin films with larger grains exhibit superior oxygen evolution performance compared to those with smaller grains. When the grain size of anatase TiO_2 is sufficiently large, hole transport by the band bending does not cause deterioration of overall water splitting. This behavior can be rationalized by considering that a lower Fermi level reduces the OER energy barrier. These findings suggest that the underlying photocatalytic mechanism should be interpreted from the perspective of both the micro- and nanoscale.

From this work, I proposed a theoretical framework that highlights the complementary roles of surface reaction activity and charge carrier transport. Although simplified, this model offers a useful perspective for understanding the grain-size-dependent reactivity of semiconductor photocatalysts and can serve as a basis for future refinements in the theoretical description of heterogeneous catalysis.

Outlook

Despite the progress achieved in this work, several crucial factors in catalytic reactions on wide band gap semiconductors remain that we have not discussed yet, including, for example, the interfacial properties between electrolytes and substrates, the size-dependent charge transfer capability of cocatalyst nanoparticles, and the quantitative correlation between grain boundaries and catalytic activity. In addition, the theoretical model for photocatalytic reactions (in Chapters 4.2 and 5) has two major assumptions: that recombination is negligible and that the photocatalytic reaction occurs under full photoexcitation. Although the theoretical results in these works were able to elucidate and support the experimental observations, more sophisticated theoretical work will be required in parallel with advancements in material fabrication techniques. In future studies, these assumptions may be considered thoroughly as well. Overall, I believe that this theoretical framework will help address the existing limitations and contribute to a better understanding of heterogeneous catalytic reaction mechanisms on wide band gap semiconductors.

References

(1) Heveling, J. Heterogeneous Catalytic Chemistry by Example of Industrial Applications. *J. Chem. Educ.* **2012**, *89* (12), 1530–1536. https://doi.org/10.1021/ed200816g.

(2) Humphreys, J.; Lan, R.; Tao, S. Development and Recent Progress on Ammonia Synthesis Catalysts for Haber–Bosch Process. *Adv. Energy Sustain. Res.* **2021**, *2* (1), 2000043. https://doi.org/10.1002/aesr.202000043.

(3) Corma, A. Application of Zeolites in Fluid Catalytic Cracking and Related Processes. In *Studies in Surface Science and Catalysis*; Jacobs, P. A., van Santen, R. A., Eds.; Zeolites: Facts, Figures, Future Part A - Proceedings of the 8th International Zeolite Conference; Elsevier, 1989; Vol. 49, pp 49–67. https://doi.org/10.1016/S0167-2991(08)61708-5.

(4) Rayadurgam, J.; Sana, S.; Sasikumar, M.; Gu, Q. Palladium Catalyzed C–C and C–N Bond Forming Reactions: An Update on the Synthesis of Pharmaceuticals from 2015–2020. *Org. Chem. Front.* **2021**, *8* (2), 384–414. https://doi.org/10.1039/D0QO01146K.

(5) Lin, J.; Zhang, Y.; Xu, P.; Chen, L. CO_2 Electrolysis: Advances and Challenges in Electrocatalyst Engineering and Reactor Design. *Mater. Rep. Energy* **2023**, *3* (2), 100194. https://doi.org/10.1016/j.matre.2023.100194.

(6) Roberts, M. W. Birth of the Catalytic Concept (1800-1900). *Catal. Lett.* **2000**, *67* (1), 1–4. https://doi.org/10.1023/A:1016622806065.

(7) Ertl, G. Wilhelm Ostwald: Founder of Physical Chemistry and Nobel Laureate 1909. *Angew. Chem. Int. Ed.* **2009**, *48* (36), 6600–6606. https://doi.org/10.1002/anie.200901193.

(8) Laidler, K. J. A Glossary of Terms Used in Chemical Kinetics, Including Reaction Dynamics (IUPAC Recommendations 1996). *Pure Appl. Chem.* **1996**, *68* (1), 149–192. https://doi.org/10.1351/pac199668010149.

(9) Atkins, P.; De Paula, J.; Keeler, J. *Atkins' Physical Chemistry*, 11th ed.; Oxford University Press, 2017.

(10) Roduner, E. Understanding Catalysis. *Chem. Soc. Rev.* **2014**, *43* (24), 8226–8239. https://doi.org/10.1039/C4CS00210E.

(11) Ward, T. R.; Copéret, C. Introduction: Bridging the Gaps: Learning from Catalysis across Boundaries. *Chem. Rev.* **2023**, *123* (9), 5221–5224. https://doi.org/10.1021/acs.chemrev.3c00029.

(12) Osborn, J. A.; Jardine, F. H.; Young, J. F.; Wilkinson, G. The Preparation and Properties of Tris(Triphenylphosphine)Halogenorhodium(I) and Some Reactions Thereof Including Catalytic Homogeneous Hydrogenation of Olefins and Acetylenes and Their Derivatives. *J. Chem. Soc. Inorg. Phys. Theor.* **1966**, 1711. https://doi.org/10.1039/j19660001711.

(13) List, B.; Lerner, R. A.; Barbas, C. F. Proline-Catalyzed Direct Asymmetric Aldol Reactions. *J. Am. Chem. Soc.* **2000**, *122* (10), 2395–2396. https://doi.org/10.1021/ja994280y.

(14) Schlögl, R. Heterogeneous Catalysis. *Angew. Chem. Int. Ed.* **2015**, *54* (11), 3465–3520. https://doi.org/10.1002/anie.201410738.

(15) Wang, H.; Blaylock, D. W.; Dam, A. H.; Liland, S. E.; Rout, K. R.; Zhu, Y.-A.; Green, W. H.; Holmen, A.; Chen, D. Steam Methane Reforming on a Ni-Based Bimetallic Catalyst: Density Functional Theory and Experimental Studies of the Catalytic Consequence of Surface Alloying of Ni with Ag. *Catal. Sci. Technol.* **2017**, *7* (8), 1713–1725. https://doi.org/10.1039/C7CY00101K.

(16) Wu, S.; Snajdrova, R.; Moore, J. C.; Baldenius, K.; Bornscheuer, U. T. Biocatalysis: Enzymatic Synthesis for Industrial Applications. *Angew. Chem. Int. Ed.* **2021**, *60* (1), 88–119. https://doi.org/10.1002/anie.202006648.

(17) Gandhi, N. N.; Patil, N. S.; Sawant, S. B.; Joshi, J. B.; Wangikar, P. P.; Mukesh, D. Lipase-Catalyzed Esterification. *Catal. Rev.* **2000**, *42* (4), 439–480. https://doi.org/10.1081/CR-100101953.

(18) Keinan, Ehud.; Hafeli, E. K.; Seth, K. K.; Lamed, Raphael. Thermostable Enzymes in Organic Synthesis. 2. Asymmetric Reduction of Ketones with Alcohol Dehydrogenase from Thermoanaerobium Brockii. *J. Am. Chem. Soc.* **1986**, *108* (1), 162–169. https://doi.org/10.1021/ja00261a026.

(19) Dumesic, J. A.; Huber, G. W.; Boudart, M. Principles of Heterogeneous Catalysis. In *Handbook of Heterogeneous Catalysis*; Ertl, G., Knözinger, H., Schüth, F., Weitkamp, J., Eds.; Wiley, 1996. https://doi.org/10.1002/9783527610044.hetcat0001.

(20) Wisniak, J. The History of Catalysis. From the Beginning to Nobel Prizes. *Educ. Quím.* **2010**, *21* (1), 60–69. https://doi.org/10.1016/S0187-893X(18)30074-0.

(21) Dry, M. E. The Fischer–Tropsch Process: 1950–2000. *Catal. Today* **2002**, *71* (3), 227–241. https://doi.org/10.1016/S0920-5861(01)00453-9.

(22) Jiang, C.; Moniz, S. J. A.; Wang, A.; Zhang, T.; Tang, J. Photoelectrochemical Devices for Solar Water Splitting – Materials and Challenges. *Chem. Soc. Rev.* **2017**, *46* (15), 4645–4660. https://doi.org/10.1039/c6cs00306k.

(23) Altmayer, J.; Barth, S.; Mathur, S. Influence of Precursor Chemistry on CVD Grown TiO_2 Coatings: Differential Cell Growth and Biocompatibility. *RSC Adv.* **2013**, *3* (28), 11234–11239. https://doi.org/10.1039/C3RA00050H.

(24) Möllmann, A.; Gedamu, D.; Vivo, P.; Frohnhoven, R.; Stadler, D.; Fischer, T.; Ka, I.; Steinhorst, M.; Nechache, R.; Rosei, F.; Cloutier, S. G.; Kirchartz, T.; Mathur, S. Highly Compact TiO_2 Films by Spray Pyrolysis and Application in Perovskite Solar Cells. *Adv. Eng. Mater.* **2019**, *21* (4), 1801196. https://doi.org/10.1002/adem.201801196.

(25) Pan, J.; Shen, H.; Mathur, S. One-Dimensional SnO_2 Nanostructures: Synthesis and Applications. *J. Nanotechnol.* **2012**, *2012* (1), 917320. https://doi.org/10.1155/2012/917320.

(26) Warwick, M. E. A.; Carraro, G.; Gasparotto, A.; Maccato, C.; Barreca, D.; Sada, C.; Bontempi, E.; Gönüllü, Y.; Mathur, S. Interplay of Thickness and Photoelectrochemical Properties in Nanostructured α-Fe_2O_3 Thin Films. *Phys. Status Solidi A* **2015**, *212* (7), 1501–1507. https://doi.org/10.1002/pssa.201532366.

(27) Han, N.; Zhang, W.; Guo, W.; Pan, H.; Jiang, B.; Xing, L.; Tian, H.; Wang, G.; Zhang, X.; Fransaer, J. Designing Oxide Catalysts for Oxygen Electrocatalysis: Insights from Mechanism to Application. *Nano-Micro Lett.* **2023**, *15* (1), 185. https://doi.org/10.1007/s40820-023-01152-z.

(28) Sahoo, S.; Wickramathilaka, K. Y.; Njeri, E.; Silva, D.; Suib, S. L. A Review on Transition Metal Oxides in Catalysis. *Front. Chem.* **2024**, *12*, 1374878. https://doi.org/10.3389/fchem.2024.1374878.

(29) De Luna, P.; Hahn, C.; Higgins, D.; Jaffer, S. A.; Jaramillo, T. F.; Sargent, E. H. What Would It Take for Renewably Powered Electrosynthesis to Displace Petrochemical Processes? *Science* **2019**, *364* (6438), eaav3506. https://doi.org/10.1126/science.aav3506.

(30) Aguirre, M. E.; Zhou, R.; Eugene, A. J.; Guzman, M. I.; Grela, M. A. Cu_2O/TiO_2 Heterostructures for CO_2 Reduction through a Direct Z-Scheme: Protecting Cu_2O from Photocorrosion. *Appl. Catal. B Environ.* **2017**, *217*, 485–493. https://doi.org/10.1016/j.apcatb.2017.05.058.

(31) Cherif, Y.; Azzi, H.; Sridharan, K.; Ji, S.; Choi, H.; Allan, M. G.; Benaissa, S.; Saidi-Bendahou, K.; Damptey, L.; Ribeiro, C. S.; Krishnamurthy, S.; Nagarajan, S.; Maroto-

Valer, M. M.; Kuehnel, M. F.; Pitchaimuthu, S. Facile Synthesis of Gram-Scale Mesoporous Ag/TiO_2 Photocatalysts for Pharmaceutical Water Pollutant Removal and Green Hydrogen Generation. *ACS Omega* **2023**, *8* (1), 1249–1261. https://doi.org/10.1021/acsomega.2c06657.

(32) Liu, Z.; Ji, S.; Zhao, S.; Hu, X.; An, X.; Liu, T.; Cheng, X.; Choi, H.; Dawson, G. Fermi Level Pinning Strategy to Boost the Photocatalytic Water Splitting Reaction of g-C_3N_4 with One-Step Multi-Phase Fe_2O_3 Self-Assembly. *J. Alloys Compd.* **2025**, *1019*, 179318. https://doi.org/10.1016/j.jallcom.2025.179318.

(33) Leduc, J.; Goenuellue, Y.; Ghamgosar, P.; You, S.; Mouzon, J.; Choi, H.; Vomiero, A.; Grosch, M.; Mathur, S. Electronically-Coupled Phase Boundaries in α-Fe_2O_3/Fe_3O_4 Nanocomposite Photoanodes for Enhanced Water Oxidation. *ACS Appl. Nano Mater.* **2019**, *2* (1), 334–342. https://doi.org/10.1021/acsanm.8b01936.

(34) Zhang, C.; Chen, B.; Mei, D.; Liang, X. The OH − -Driven Synthesis of Pt–Ni Nanocatalysts with Atomic Segregation for Alkaline Hydrogen Evolution Reaction. *J. Mater. Chem. A* **2019**, *7* (10), 5475–5481. https://doi.org/10.1039/C8TA12250D.

(35) Xia, C.; Qiu, Y.; Xia, Y.; Zhu, P.; King, G.; Zhang, X.; Wu, Z.; Kim, J. Y.; Cullen, D. A.; Zheng, D.; Li, P.; Shakouri, M.; Heredia, E.; Cui, P.; Alshareef, H. N.; Hu, Y.; Wang, H. General Synthesis of Single-Atom Catalysts with High Metal Loading Using Graphene Quantum Dots. *Nat. Chem.* **2021**, *13* (9), 887–894. https://doi.org/10.1038/s41557-021-00734-x.

(36) Zhang, J.; Lima, F. H. B.; Shao, M. H.; Sasaki, K.; Wang, J. X.; Hanson, J.; Adzic, R. R. Platinum Monolayer on Nonnoble Metal−Noble Metal Core−Shell Nanoparticle Electrocatalysts for O2 Reduction. *J. Phys. Chem. B* **2005**, *109* (48), 22701–22704. https://doi.org/10.1021/jp055634c.

(37) Wang, H.; Zhang, L.; Chen, Z.; Hu, J.; Li, S.; Wang, Z.; Liu, J.; Wang, X. Semiconductor Heterojunction Photocatalysts: Design, Construction, and Photocatalytic Performances. *Chem. Soc. Rev.* **2014**, *43* (15), 5234–5244. https://doi.org/10.1039/C4CS00126E.

(38) Ji, S.; Won Jeon, D.; Choi, J.; Cho, H.; Park, B.-I.; Roh, I.; Choi, H.; Kim, C.; Kyu Kim, J.; Sim, U.; Li, D.; Ko, H.; Beom Cho, S.; Choi, H. Overcoming the Limitations of Atomic-Scale Simulations on Semiconductor Catalysis with Changing Fermi Level and Surface Treatment. *J. Mater. Chem. A* **2024**, *12* (48), 33537–33545. https://doi.org/10.1039/D4TA03595J.

(39) Zhang, Z.; Yates, J. T. Band Bending in Semiconductors: Chemical and Physical Consequences at Surfaces and Interfaces. *Chem. Rev.* **2012**, *112* (10), 5520–5551. https://doi.org/10.1021/cr3000626.

(40) Nakaya, Y.; Furukawa, S. Catalysis of Alloys: Classification, Principles, and Design for a Variety of Materials and Reactions. *Chem. Rev.* **2023**, *123* (9), 5859–5947. https://doi.org/10.1021/acs.chemrev.2c00356.

(41) Zhang, Q.; Lee, I.; Joo, J. B.; Zaera, F.; Yin, Y. Core–Shell Nanostructured Catalysts. *Acc. Chem. Res.* **2013**, *46* (8), 1816–1824. https://doi.org/10.1021/ar300230s.

(42) Xue, Z.-H.; Luan, D.; Zhang, H.; (David) Lou, X. W. Single-Atom Catalysts for Photocatalytic Energy Conversion. *Joule* **2022**, *6* (1), 92–133. https://doi.org/10.1016/j.joule.2021.12.011.

(43) Nørskov, J. K.; Rossmeisl, J.; Logadottir, A.; Lindqvist, L.; Kitchin, J. R.; Bligaard, T.; Jónsson, H. Origin of the Overpotential for Oxygen Reduction at a Fuel-Cell Cathode. *J. Phys. Chem. B* **2004**, *108* (46), 17886–17892. https://doi.org/10.1021/jp047349j.

(44) Kim, S.; Ji, S.; Kim, K. H.; Roh, S. H.; Cho, Y.; Lee, C.-L.; Lee, K.-S.; Choi, D.-G.; Choi, H.; Kim, J. K.; Park, J. H. Revisiting Surface Chemistry in TiO_2: A Critical Role of Ionic Passivation for pH-Independent and Anti-Corrosive Photoelectrochemical Water Oxidation. *Chem. Eng. J.* **2021**, *407*, 126929. https://doi.org/10.1016/j.cej.2020.126929.

(45) Sabatier, P. *La catalyse en chimie organique*; C. Béranger, 1920; Vol. 3.

(46) Medford, A. J.; Vojvodic, A.; Hummelshøj, J. S.; Voss, J.; Abild-Pedersen, F.; Studt, F.; Bligaard, T.; Nilsson, A.; Nørskov, J. K. From the Sabatier Principle to a Predictive Theory of Transition-Metal Heterogeneous Catalysis. *J. Catal.* **2015**, *328*, 36–42. https://doi.org/10.1016/j.jcat.2014.12.033.

(47) Langmuir, I. THE ADSORPTION OF GASES ON PLANE SURFACES OF GLASS, MICA AND PLATINUM. *J. Am. Chem. Soc.* **1918**, *40* (9), 1361–1403. https://doi.org/10.1021/ja02242a004.

(48) Swenson, H.; Stadie, N. P. Langmuir's Theory of Adsorption: A Centennial Review. *Langmuir* **2019**, *35* (16), 5409–5426. https://doi.org/10.1021/acs.langmuir.9b00154.

(49) Silverstein, T. P. Marcus Theory: Thermodynamics CAN Control the Kinetics of Electron Transfer Reactions. *J. Chem. Educ.* **2012**, *89* (9), 1159–1167. https://doi.org/10.1021/ed1007712.

(50) Marcus, R. A. On the Theory of Oxidation-Reduction Reactions Involving Electron Transfer. I. *J. Chem. Phys.* **1956**, *24* (5), 966–978. https://doi.org/10.1063/1.1742723.

(51) Marcus, R. A.; Sutin, N. Electron Transfers in Chemistry and Biology. *Biochim. Biophys. Acta BBA - Rev. Bioenerg.* **1985**, *811* (3), 265–322. https://doi.org/10.1016/0304-4173(85)90014-x.

(52) Zhu, X.-Q.; Yang, J.-D. Direct Conflict of Marcus Theory with the Law of Conservation of Energy. *J. Phys. Org. Chem.* **2013**, *26* (3), 271–273. https://doi.org/10.1002/poc.3078.

(53) Nørskov, J. K.; Bligaard, T.; Logadottir, A.; Kitchin, J. R.; Chen, J. G.; Pandelov, S.; Stimming, U. Trends in the Exchange Current for Hydrogen Evolution. *J. Electrochem. Soc.* **2005**, *152* (3), J23. https://doi.org/10.1149/1.1856988.

(54) Man, I. C.; Su, H.-Y.; Calle-Vallejo, F.; Hansen, H. A.; Martínez, J. I.; Inoglu, N. G.; Kitchin, J.; Jaramillo, T. F.; Nørskov, J. K.; Rossmeisl, J. Universality in Oxygen Evolution Electrocatalysis on Oxide Surfaces. *ChemCatChem* **2011**, *3* (7), 1159–1165. https://doi.org/10.1002/cctc.201000397.

(55) Liu, X.; Xiao, J.; Peng, H.; Hong, X.; Chan, K.; Nørskov, J. K. Understanding Trends in Electrochemical Carbon Dioxide Reduction Rates. *Nat. Commun.* **2017**, *8* (1), 15438. https://doi.org/10.1038/ncomms15438.

(56) Hammes-Schiffer, S. Proton-Coupled Electron Transfer: Moving Together and Charging Forward. *J. Am. Chem. Soc.* **2015**, *137* (28), 8860–8871. https://doi.org/10.1021/jacs.5b04087.

(57) Nørskov, J. K.; Studt, F.; Abild-Pedersen, F.; Bligaard, T. *Fundamental Concepts in Heterogeneous Catalysis*; Wiley: Hoboken, New Jersey, 2014.

(58) Kolasinski, K. W. *Surface Science: Foundations of Catalysis and Nanoscience*, 1st ed.; Wiley, 2012. https://doi.org/10.1002/9781119941798.

(59) Kleis, J.; Jones, G.; Abild-Pedersen, F.; Tripkovic, V.; Bligaard, T.; Rossmeisl, J. Trends for Methane Oxidation at Solid Oxide Fuel Cell Conditions. *J. Electrochem. Soc.* **2009**, *156* (12), B1447. https://doi.org/10.1149/1.3230622.

(60) Ringe, S.; Hörmann, N. G.; Oberhofer, H.; Reuter, K. Implicit Solvation Methods for Catalysis at Electrified Interfaces. *Chem. Rev.* **2022**, *122* (12), 10777–10820. https://doi.org/10.1021/acs.chemrev.1c00675.

(61) Sze, S. M.; Ng, K. K. *Physics of Semiconductor Devices*, 3. ed.; Wiley-Interscience online books; Wiley-Interscience: Hoboken, N.J, 2007. https://doi.org/10.1002/0470068329.

(62) Pacchioni, G.; Freund, H.-J. Controlling the Charge State of Supported Nanoparticles in Catalysis: Lessons from Model Systems. **2018**. https://doi.org/10.1039/C8CS00152A.

(63) Neamen, D. A. *Semiconductor Physics and Devices: Basic Principles*, 4th ed.; McGraw-Hill: New York, NY, 2012.

(64) Pan, J. Scaling up System Size in Materials Simulation. *Nat. Comput. Sci.* **2021**, *1* (2), 95–95. https://doi.org/10.1038/s43588-021-00034-x.

(65) Van Houten, J. A Century of Chemical Dynamics Traced through the Nobel Prizes. 1998: Walter Kohn and John Pople. *J. Chem. Educ.* **2002**, *79* (11), 1297. https://doi.org/10.1021/ed079p1297.

(66) Martin, R. M. *Electronic Structure: Basic Theory and Practical Methods*, 1st ed.; Cambridge University Press, 2004. https://doi.org/10.1017/CBO9780511805769.

(67) Griffiths, D. J.; Schroeter, D. F. *Introduction to Quantum Mechanics*, 3rd ed.; Cambridge University Press, 2018. https://doi.org/10.1017/9781316995433.

(68) Born, M.; Oppenheimer, R. Zur Quantentheorie Der Molekeln. *Ann. Phys.* **1927**, *389* (20), 457–484. https://doi.org/10.1002/andp.19273892002.

(69) Kohn, W.; Sham, L. J. Self-Consistent Equations Including Exchange and Correlation Effects. *Phys. Rev.* **1965**, *140* (4A), A1133–A1138. https://doi.org/10.1103/physrev.140.a1133.

(70) Ceperley, D. M.; Alder, B. J. Ground State of the Electron Gas by a Stochastic Method. *Phys. Rev. Lett.* **1980**, *45* (7), 566–569. https://doi.org/10.1103/PhysRevLett.45.566.

(71) Perdew, J. P.; Burke, K.; Ernzerhof, M. Generalized Gradient Approximation Made Simple. *Phys. Rev. Lett.* **1996**, *77* (18), 3865–3868. https://doi.org/10.1103/PhysRevLett.77.3865.

(72) Perdew, J. P.; Chevary, J. A.; Vosko, S. H.; Jackson, K. A.; Pederson, M. R.; Singh, D. J.; Fiolhais, C. Atoms, Molecules, Solids, and Surfaces: Applications of the Generalized Gradient Approximation for Exchange and Correlation. *Phys. Rev. B* **1992**, *46* (11), 6671–6687. https://doi.org/10.1103/PhysRevB.46.6671.

(73) Becke, A. D. Density-Functional Exchange-Energy Approximation with Correct Asymptotic Behavior. *Phys. Rev. A* **1988**, *38* (6), 3098–3100. https://doi.org/10.1103/PhysRevA.38.3098.

(74) Hamann, D. R.; Schlüter, M.; Chiang, C. Norm-Conserving Pseudopotentials. *Phys. Rev. Lett.* **1979**, *43* (20), 1494–1497. https://doi.org/10.1103/physrevlett.43.1494.

(75) Hubbard, J. Electron Correlations in Narrow Energy Bands. II. The Degenerate Band Case. *Proc. R. Soc. Lond. Ser. Math. Phys. Sci.* **1964**, *277* (1369), 237–259. https://doi.org/10.1098/rspa.1964.0019.

(76) Himmetoglu, B.; Floris, A.; de Gironcoli, S.; Cococcioni, M. Hubbard-Corrected DFT Energy Functionals: The LDA+U Description of Correlated Systems. *Int. J. Quantum Chem.* **2014**, *114* (1), 14–49. https://doi.org/10.1002/qua.24521.

(77) Montini, T.; Melchionna, M.; Monai, M.; Fornasiero, P. Fundamentals and Catalytic Applications of CeO_2-Based Materials. *Chem. Rev.* **2016**, *116* (10), 5987–6041. https://doi.org/10.1021/acs.chemrev.5b00603.

(78) Graciani, J.; Márquez, A. M.; Plata, J. J.; Ortega, Y.; Hernández, N. C.; Meyer, A.; Zicovich-Wilson, C. M.; Sanz, J. Fdez. Comparative Study on the Performance of Hybrid DFT Functionals in Highly Correlated Oxides: The Case of CeO_2 and Ce_2O_3. *J. Chem. Theory Comput.* **2011**, *7* (1), 56–65. https://doi.org/10.1021/ct100430q.

(79) Lee, J.; Lim, T. H.; Lee, E.; Kim, D. H. Promoting the Methane Oxidation on Pd/CeO_2 Catalyst by Increasing the Surface Oxygen Mobility via Defect Engineering. *ChemCatChem* **2021**, *13* (16), 3706–3712. https://doi.org/10.1002/cctc.202100653.

(80) Lykhach, Y.; Kozlov, S. M.; Skála, T.; Tovt, A.; Stetsovych, V.; Tsud, N.; Dvořák, F.; Johánek, V.; Neitzel, A.; Mysliveček, J.; Fabris, S.; Matolín, V.; Neyman, K. M.; Libuda, J. Counting Electrons on Supported Nanoparticles. *Nat. Mater.* **2016**, *15* (3), 284–288. https://doi.org/10.1038/nmat4500.

(81) Dou, J.; Tang, Y.; Nie, L.; Andolina, C. M.; Zhang, X.; House, S.; Li, Y.; Yang, J.; Tao, F. (Feng). Complete Oxidation of Methane on Co_3O_4/CeO_2 Nanocomposite: A Synergic Effect. *Catal. Today* **2018**, *311*, 48–55. https://doi.org/10.1016/j.cattod.2017.12.027.

(82) Chen, J.; Carlson, B. D.; Toops, T. J.; Li, Z.; Lance, M. J.; Karakalos, S. G.; Choi, J.-S.; Kyriakidou, E. A. Methane Combustion Over Ni/$Ce_xZr_{1-x}O_2$ Catalysts: Impact of Ceria/Zirconia Ratio. *ChemCatChem* **2020**, *12* (21), 5558–5568. https://doi.org/10.1002/cctc.202000947.

(83) Toscani, L. M.; Bellora, M. S.; Huck-Iriart, C.; Soldati, A. L.; Sacanell, J.; Martins, T. S.; Craievich, A. F.; Fantini, M. C. A.; Larrondo, S. A.; Lamas, D. G. NiO/CeO_2-Sm_2O_3 Nanocomposites for Partial Oxidation of Methane: In-Situ Experiments by Dispersive X-Ray Absorption Spectroscopy. *Appl. Catal. Gen.* **2021**, *626*, 118357. https://doi.org/10.1016/j.apcata.2021.118357.

(84) Lustemberg, P. G.; Mao, Z.; Salcedo, A.; Irigoyen, B.; Ganduglia-Pirovano, M. V.; Campbell, C. T. Nature of the Active Sites on Ni/CeO_2 Catalysts for Methane Conversions. *ACS Catal.* **2021**, *11* (16), 10604–10613. https://doi.org/10.1021/acscatal.1c02154.

(85) Zhang, Z.; Yu, Z.; Feng, K.; Yan, B. Eu^{3+} Doping-Promoted Ni-CeO_2 Interaction for Efficient Low-Temperature CO_2 Methanation. *Appl. Catal. B Environ.* **2022**, *317*, 121800. https://doi.org/10.1016/j.apcatb.2022.121800.

(86) Ruiz Puigdollers, A.; Schlexer, P.; Tosoni, S.; Pacchioni, G. Increasing Oxide Reducibility: The Role of Metal/Oxide Interfaces in the Formation of Oxygen Vacancies. *ACS Catal.* **2017**, *7* (10), 6493–6513. https://doi.org/10.1021/acscatal.7b01913.

(87) Sterrer, M.; Yulikov, M.; Fischbach, E.; Heyde, M.; Rust, H.-P.; Pacchioni, G.; Risse, T.; Freund, H.-J. Interaction of Gold Clusters with Color Centers on MgO(001) Films. *Angew. Chem. Int. Ed.* **2006**, *45* (16), 2630–2632. https://doi.org/10.1002/anie.200504443.

(88) Abbet, S.; Sanchez, A.; Heiz, U.; Schneider, W.-D.; Ferrari, A. M.; Pacchioni, G.; Rösch, N. Acetylene Cyclotrimerization on Supported Size-Selected Pd_n Clusters ($1 \leq n \leq 30$): One Atom Is Enough! *J. Am. Chem. Soc.* **2000**, *122* (14), 3453–3457. https://doi.org/10.1021/ja9922476.

(89) Wang, H.; Gu, X.-K.; Zheng, X.; Pan, H.; Zhu, J.; Chen, S.; Cao, L.; Li, W.-X.; Lu, J. Disentangling the Size-Dependent Geometric and Electronic Effects of Palladium Nanocatalysts beyond Selectivity. *Sci. Adv.* **2019**, *5* (1), eaat6413. https://doi.org/10.1126/sciadv.aat6413.

(90) Chen, S.; Li, S.; You, R.; Guo, Z.; Wang, F.; Li, G.; Yuan, W.; Zhu, B.; Gao, Y.; Zhang, Z.; Yang, H.; Wang, Y. Elucidation of Active Sites for CH_4 Catalytic Oxidation over Pd/CeO_2 Via Tailoring Metal–Support Interactions. *ACS Catal.* **2021**, *11* (9), 5666–5677. https://doi.org/10.1021/acscatal.1c00839.

(91) Mahara, Y.; Ohyama, J.; Tojo, T.; Murata, K.; Ishikawa, H.; Satsuma, A. Enhanced Activity for Methane Combustion over a $Pd/Co/Al_2O_3$ Catalyst Prepared by a Galvanic Deposition Method. *Catal. Sci. Technol.* **2016**, *6* (13), 4773–4776. https://doi.org/10.1039/C6CY00650G.

(92) Hornés, A.; Bera, P.; Fernández-García, M.; Guerrero-Ruiz, A.; Martínez-Arias, A. Catalytic and Redox Properties of Bimetallic Cu–Ni Systems Combined with CeO_2 or Gd-Doped CeO_2 for Methane Oxidation and Decomposition. *Appl. Catal. B Environ.* **2012**, *111–112*, 96–105. https://doi.org/10.1016/j.apcatb.2011.09.022.

(93) Arshad, M.; Iqbal, A.; Ahamad, T.; Gupta, J.; Arshad, M.; Ahmed, A. S. Biogenic Synthesis of Pure and Ag-Doped CeO_2 Nanoparticles and Analysis of Their Dielectric Properties. *J. Electron. Mater.* **2023**, *52* (8), 5690–5706. https://doi.org/10.1007/s11664-023-10461-3.

(94) Knauth, P.; Tuller, H. L. Solute Segregation, Electrical Properties and Defect Thermodynamics of Nanocrystalline TiO_2 and CeO_2. *Solid State Ion.* **2000**, *136–137*, 1215–1224. https://doi.org/10.1016/S0167-2738(00)00588-9.

(95) Righi, G.; Magri, R.; Selloni, A. Methane Activation on Metal-Doped (111) and (100) Ceria Surfaces with Charge-Compensating Oxygen Vacancies. *J. Phys. Chem. C* **2020**, *124* (32), 17578–17585. https://doi.org/10.1021/acs.jpcc.0c03320.

(96) Polychronopoulou, K.; AlKhoori, A. A.; Efstathiou, A. M.; Jaoude, M. A.; Damaskinos, C. M.; Baker, M. A.; Almutawa, A.; Anjum, D. H.; Vasiliades, M. A.; Belabbes, A.; Vega, L. F.; Zedan, A. F.; Hinder, S. J. Design Aspects of Doped CeO_2 for Low-Temperature Catalytic CO Oxidation: Transient Kinetics and DFT Approach. *ACS Appl. Mater. Interfaces* **2021**, *13* (19), 22391–22415. https://doi.org/10.1021/acsami.1c02934.

(97) Khojasteh, F.; Mersagh, M. R.; Hashemipour, H. The Influences of Ni, Ag-Doped TiO_2 and SnO_2, Ag-Doped SnO_2/TiO_2 Nanocomposites on Recombination Reduction in Dye Synthesized Solar Cells. *J. Alloys Compd.* **2022**, *890*, 161709. https://doi.org/10.1016/j.jallcom.2021.161709.

(98) Kwak, N. W.; Jeong, S. J.; Seo, H. G.; Lee, S.; Kim, Y.; Kim, J. K.; Byeon, P.; Chung, S.-Y.; Jung, W. In Situ Synthesis of Supported Metal Nanocatalysts through Heterogeneous Doping. *Nat. Commun.* **2018**, *9* (1), 4829. https://doi.org/10.1038/s41467-018-07050-y.

(99) Chen, J.; Buchanan, T.; Walker, E. A.; Toops, T. J.; Li, Z.; Kunal, P.; Kyriakidou, E. A. Mechanistic Understanding of Methane Combustion over Ni/CeO_2 : A Combined Experimental and Theoretical Approach. *ACS Catal.* **2021**, *11* (15), 9345–9354. https://doi.org/10.1021/acscatal.1c01088.

(100) Ha, H.; Yoon, S.; An, K.; Kim, H. Y. Catalytic CO Oxidation over Au Nanoparticles Supported on CeO_2 Nanocrystals: Effect of the Au–CeO_2 Interface. *ACS Catal.* **2018**, *8* (12), 11491–11501. https://doi.org/10.1021/acscatal.8b03539.

(101) Rahman, Md. S.; Paudyal, N.; Hill, L. D.; Zhou, J.; Xu, Y. The Structure, Oxidation States, and Energetics of Co Nanoparticles on CeO_2(111): An STM and DFT Study. *J. Phys. Chem. C* **2024**, *128* (43), 18430–18441. https://doi.org/10.1021/acs.jpcc.4c03911.

(102) Muravev, V.; Parastaev, A.; van den Bosch, Y.; Ligt, B.; Claes, N.; Bals, S.; Kosinov, N.; Hensen, E. J. M. Size of Cerium Dioxide Support Nanocrystals Dictates Reactivity of Highly Dispersed Palladium Catalysts. *Science* **2023**, *380* (6650), 1174–1179. https://doi.org/10.1126/science.adf9082.

(103) Bohigues, B.; Rojas-Buzo, S.; Salusso, D.; Xia, Y.; Corma, A.; Bordiga, S.; Boronat, M.; Willhammar, T.; Moliner, M.; Serna, P. Overcoming Activity/Stability Tradeoffs in CO Oxidation Catalysis by Pt/CeO_2. *Nat. Commun.* **2025**, *16* (1), 7451. https://doi.org/10.1038/s41467-025-62726-6.

(104) Li, Y.; Je, M.; Kim, J.; Xia, C.; Roh, S. H.; So, W.; Lee, H.; Kim, D.-H.; Cho, S. M.; Bae, J. W.; Choi, H.; Kim, J. K. Rational Nanopositioning of Homogeneous Amorphous Phase on Crystalline Tungsten Oxide for Boosting Solar Water Oxidation. *Chem. Eng. J.* **2022**, *438*, 135532. https://doi.org/10.1016/j.cej.2022.135532.

(105) Krukowski, S.; Kempisty, P.; Strąk, P. Fermi Level Influence on the Adsorption at Semiconductor Surfaces— *Ab Initio* Simulations. *J. Appl. Phys.* **2013**, *114* (6), 063507. https://doi.org/10.1063/1.4817903.

(106) Jiang, C.; Moniz, S. J. A.; Wang, A.; Zhang, T.; Tang, J. Photoelectrochemical Devices for Solar Water Splitting – Materials and Challenges. *Chem. Soc. Rev.* **2017**, *46* (15), 4645–4660. https://doi.org/10.1039/C6CS00306K.

(107) Kresse, G.; Furthmüller, J. Efficiency of Ab-Initio Total Energy Calculations for Metals and Semiconductors Using a Plane-Wave Basis Set. *Comput. Mater. Sci.* **1996**, *6* (1), 15–50. https://doi.org/10.1016/0927-0256(96)00008-0.

(108) Kresse, G.; Joubert, D. From Ultrasoft Pseudopotentials to the Projector Augmented-Wave Method. *Phys. Rev. B* **1999**, *59* (3), 1758–1775. https://doi.org/10.1103/PhysRevB.59.1758.

(109) Kresse, G.; Furthmüller, J. Efficient Iterative Schemes for *Ab Initio* Total-Energy Calculations Using a Plane-Wave Basis Set. *Phys. Rev. B* **1996**, *54* (16), 11169–11186. https://doi.org/10.1103/PhysRevB.54.11169.

(110) Monkhorst, H. J.; Pack, J. D. Special Points for Brillouin-Zone Integrations. *Phys. Rev. B* **1976**, *13* (12), 5188–5192. https://doi.org/10.1103/PhysRevB.13.5188.

(111) Dudarev, S. L.; Botton, G. A.; Savrasov, S. Y.; Humphreys, C. J.; Sutton, A. P. Electron-Energy-Loss Spectra and the Structural Stability of Nickel Oxide: An LSDA+U Study. *Phys. Rev. B* **1998**, *57* (3), 1505–1509. https://doi.org/10.1103/PhysRevB.57.1505.

(112) Yu, S.-W.; Carpenter, M. H.; Ponce, F.; Friedrich, S.; Lee, J.-S.; Olalde-Velasco, P.; Yang, W. L.; Åberg, D. Energy Levels of the Ce Activator Relative to the YAP(Ce) Scintillator Host. *J. Phys. Condens. Matter* **2015**, *27* (18), 185501. https://doi.org/10.1088/0953-8984/27/18/185501.

(113) Chase, M. W.; Curnutt, J. L.; Downey, J. R.; McDonald, R. A.; Syverud, A. N.; Valenzuela, E. A. JANAF Thermochemical Tables, 1982 Supplement. *J. Phys. Chem. Ref. Data* **1982**, *11* (3), 695–940. https://doi.org/10.1063/1.555666.

(114) Komsa, H.-P.; Rantala, T.; Pasquarello, A. Comparison between Various Finite-Size Supercell Correction Schemes for Charged Defect Calculations. *Phys. B Condens. Matter* **2012**, *407* (15), 3063–3067. https://doi.org/10.1016/j.physb.2011.08.028.

(115) Komsa, H.-P.; Pasquarello, A. Finite-Size Supercell Correction for Charged Defects at Surfaces and Interfaces. *Phys. Rev. Lett.* **2013**, *110* (9), 095505. https://doi.org/10.1103/PhysRevLett.110.095505.

(116) Farzalipour Tabriz, M.; Aradi, B.; Frauenheim, T.; Deák, P. SLABCC: Total Energy Correction Code for Charged Periodic Slab Models. *Comput. Phys. Commun.* **2019**, *240*, 101–105. https://doi.org/10.1016/j.cpc.2019.02.018.

(117) Ren, H.; Lee, Y. H.; Wu, E. A.; Chung, H.; Meng, Y. S.; Fullerton, E. E.; Minh, N. Q. Nano-Ceramic Cathodes via Co-Sputtering of Gd–Ce Alloy and Lanthanum Strontium Cobaltite for Low-Temperature Thin-Film Solid Oxide Fuel Cells. *ACS Appl. Energy Mater.* **2020**, *3* (9), 8135–8142. https://doi.org/10.1021/acsaem.0c01147.

(118) Yee, A.; Morrison, S. J.; Idriss, H. A Study of the Reactions of Ethanol on CeO_2 and Pd/CeO2 by Steady State Reactions, Temperature Programmed Desorption, and In Situ FT-IR. *J. Catal.* **1999**, *186* (2), 279–295. https://doi.org/10.1006/jcat.1999.2563.

(119) Chirila, M. M.; Sarkisian, K.; Andrew, M. E.; Kwon, C.-W.; Rando, R. J.; Harper, M. A Comparison of Two Laboratories for the Measurement of Wood Dust Using Button Sampler and Diffuse Reflection Infrared Fourier-Transform Spectroscopy (DRIFTS). *Ann. Occup. Hyg.* **2015**, *59* (3), 336–346. https://doi.org/10.1093/annhyg/meu096.

(120) Celik, E.; Ma, Y.; Brezesinski, T.; Elm, M. T. Ordered Mesoporous Metal Oxides for Electrochemical Applications: Correlation between Structure, Electrical Properties and Device Performance. *Phys. Chem. Chem. Phys.* **2021**, *23* (18), 10706–10735. https://doi.org/10.1039/D1CP00834J.

(121) Albery, W. J.; Bartlett, P. N. The Transport and Kinetics of Photogenerated Carriers in Colloidal Semiconductor Electrode Particles. *J. Electrochem. Soc.* **1984**, *131* (2), 315. https://doi.org/10.1149/1.2115568.

(122) Ioannides, T.; Verykios, X. E. Charge Transfer in Metal Catalysts Supported on Doped TiO2: A Theoretical Approach Based on Metal–Semiconductor Contact Theory. *J. Catal.* **1996**, *161* (2), 560–569. https://doi.org/10.1006/jcat.1996.0218.

(123) Singha, R. K.; Shukla, A.; Yadav, A.; Sivakumar Konathala, L. N.; Bal, R. Effect of Metal-Support Interaction on Activity and Stability of Ni-CeO_2 Catalyst for Partial Oxidation of Methane. *Appl. Catal. B Environ.* **2017**, *202*, 473–488. https://doi.org/10.1016/j.apcatb.2016.09.060.

(124) Chen, J.; Pham, H. N.; Mon, T.; Toops, T. J.; Datye, A. K.; Li, Z.; Kyriakidou, E. A. Ni/CeO2 Nanocatalysts with Optimized CeO_2 Support Morphologies for CH_4 Oxidation.

ACS Appl. Nano Mater. **2023**, *6* (6), 4544–4553. https://doi.org/10.1021/acsanm.2c05496.

(125) Pantu, P.; Gavalas, G. R. Methane Partial Oxidation on Pt/CeO_2 and Pt/Al_2O_3 Catalysts. *Appl. Catal. Gen.* **2002**, *223* (1–2), 253–260. https://doi.org/10.1016/S0926-860X(01)00761-X.

(126) Kumar Singha, R.; Shukla, A.; Yadav, A.; Sain, S.; Pendem, C.; Kumar Konathala, L. N. S.; Bal, R. Synthesis Effects on Activity and Stability of $Pt\text{-}CeO_2$ Catalysts for Partial Oxidation of Methane. *Mol. Catal.* **2017**, *432*, 131–143. https://doi.org/10.1016/j.mcat.2017.01.006.

(127) Danielis, M.; Colussi, S.; Leitenburg, C. de; Soler, L.; Llorca, J.; Trovarelli, A. The Effect of Milling Parameters on the Mechanochemical Synthesis of $Pd–CeO_2$ Methane Oxidation Catalysts. *Catal. Sci. Technol.* **2019**, *9* (16), 4232–4238. https://doi.org/10.1039/C9CY01098J.

(128) Resasco, J.; DeRita, L.; Dai, S.; Chada, J. P.; Xu, M.; Yan, X.; Finzel, J.; Hanukovich, S.; Hoffman, A. S.; Graham, G. W.; Bare, S. R.; Pan, X.; Christopher, P. Uniformity Is Key in Defining Structure–Function Relationships for Atomically Dispersed Metal Catalysts: The Case of Pt/CeO_2. *J. Am. Chem. Soc.* **2020**, *142* (1), 169–184. https://doi.org/10.1021/jacs.9b09156.

(129) Xie, S.; Liu, L.; Lu, Y.; Wang, C.; Cao, S.; Diao, W.; Deng, J.; Tan, W.; Ma, L.; Ehrlich, S. N.; Li, Y.; Zhang, Y.; Ye, K.; Xin, H.; Flytzani-Stephanopoulos, M.; Liu, F. Pt Atomic Single-Layer Catalyst Embedded in Defect-Enriched Ceria for Efficient CO Oxidation. *J. Am. Chem. Soc.* **2022**, *144* (46), 21255–21266. https://doi.org/10.1021/jacs.2c08902.

(130) Pal, P.; Singha, R. K.; Saha, A.; Bal, R.; Panda, A. B. Defect-Induced Efficient Partial Oxidation of Methane over Nonstoichiometric Ni/CeO_2 Nanocrystals. *J. Phys. Chem. C* **2015**, *119* (24), 13610–13618. https://doi.org/10.1021/acs.jpcc.5b01724.

(131) Li, M.; van Veen, A. C. Tuning the Catalytic Performance of Ni-Catalysed Dry Reforming of Methane and Carbon Deposition via $Ni\text{-}CeO_{2-x}$ Interaction. *Appl. Catal. B Environ.* **2018**, *237*, 641–648. https://doi.org/10.1016/j.apcatb.2018.06.032.

(132) Divins, Núria. J.; Braga, A.; Vendrell, X.; Serrano, I.; Garcia, X.; Soler, L.; Lucentini, I.; Danielis, M.; Mussio, A.; Colussi, S.; Villar-Garcia, I. J.; Escudero, C.; Trovarelli, A.; Llorca, J. Investigation of the Evolution of Pd-Pt Supported on Ceria for Dry and Wet Methane Oxidation. *Nat. Commun.* **2022**, *13* (1), 5080. https://doi.org/10.1038/s41467-022-32765-4.

(133) Mussio, A.; Danielis, M.; Divins, N. J.; Llorca, J.; Colussi, S.; Trovarelli, A. Structural Evolution of Bimetallic PtPd/CeO_2 Methane Oxidation Catalysts Prepared by Dry Milling. *ACS Appl. Mater. Interfaces* **2021**, *13* (27), 31614–31623. https://doi.org/10.1021/acsami.1c05050.

(134) Ismail, A. M.; Csapó, E.; Janáky, C. Correlation between the Work Function of Au–Ag Nanoalloys and Their Electrocatalytic Activity in Carbon Dioxide Reduction. *Electrochimica Acta* **2019**, *313*, 171–178. https://doi.org/10.1016/j.electacta.2019.05.016.

(135) Araiza, D. G.; Arcos, D. G.; Gómez-Cortés, A.; Díaz, G. Dry Reforming of Methane over Pt-Ni/CeO_2 Catalysts: Effect of the Metal Composition on the Stability. *Catal. Today* **2021**, *360*, 46–54. https://doi.org/10.1016/j.cattod.2019.06.018.

(136) Roy, S.; Hariharan, S.; Tiwari, A. K. Pt–Ni Subsurface Alloy Catalysts: An Improved Performance toward CH_4 Dissociation. *J. Phys. Chem. C* **2018**, *122* (20), 10857–10870. https://doi.org/10.1021/acs.jpcc.8b01705.

(137) Yang, L.; Li, L.; Xia, P.; Li, H.; Yang, J.; Li, X.; Zeng, X.; Zhang, X.; Xiao, C.; Xie, Y. Enhanced Syngas Production from CO_2 Photoreduction over CoPd Alloy Modified NiAl-LDH under Visible Light. *Chem. Commun.* **2021**, *57* (88), 11629–11632. https://doi.org/10.1039/D1CC04863E.

(138) Lu, S.; Weng, B.; Chen, A.; Li, X.; Huang, H.; Sun, X.; Feng, W.; Lei, Y.; Qian, Q.; Yang, M.-Q. Facet Engineering of Pd Nanocrystals for Enhancing Photocatalytic Hydrogenation: Modulation of the Schottky Barrier Height and Enrichment of Surface Reactants. *ACS Appl. Mater. Interfaces* **2021**, *13* (11), 13044–13054. https://doi.org/10.1021/acsami.0c19260.

(139) Yoon, S.; Ha, H.; Kim, J.; Nam, E.; Yoo, M.; Jeong, B.; Kim, H. Y.; An, K. Influence of the Pt Size and CeO_2 Morphology at the Pt–CeO_2 Interface in CO Oxidation. *J. Mater. Chem. A* **2021**, *9* (46), 26381–26390. https://doi.org/10.1039/D1TA06850D.

(140) Liu, J.-X.; Su, Y.; Filot, I. A. W.; Hensen, E. J. M. A Linear Scaling Relation for CO Oxidation on CeO_2-Supported Pd. *J. Am. Chem. Soc.* **2018**, *140* (13), 4580–4587. https://doi.org/10.1021/jacs.7b13624.

(141) Zhang, X.; Zhu, L.; Hou, Q.; Guan, J.; Lu, Y.; Keal, T. W.; Buckeridge, J.; Catlow, C. R. A.; Sokol, A. A. Toward a Consistent Prediction of Defect Chemistry in CeO_2. *Chem. Mater.* **2023**, *35* (1), 207–227. https://doi.org/10.1021/acs.chemmater.2c03019.

(142) Jiang, Y.; Adams, J. B.; van Schilfgaarde, M.; Sharma, R.; Crozier, P. A. Theoretical Study of Environmental Dependence of Oxygen Vacancy Formation in CeO_2. *Appl. Phys. Lett.* **2005**, *87* (14), 141917. https://doi.org/10.1063/1.2084324.

(143) You, P.; Chen, D.; Liu, X.; Zhang, C.; Selloni, A.; Meng, S. Correlated Electron–Nuclear Dynamics of Photoinduced Water Dissociation on Rutile TiO_2. *Nat. Mater.* **2024**, *23* (8), 1100–1106. https://doi.org/10.1038/s41563-024-01900-5.

(144) Wang, D.; Sheng, T.; Chen, J.; Wang, H.-F.; Hu, P. Identifying the Key Obstacle in Photocatalytic Oxygen Evolution on Rutile TiO_2. *Nat. Catal.* **2018**, *1* (4), 291–299. https://doi.org/10.1038/s41929-018-0055-z.

(145) Afroz, K.; Moniruddin, M.; Bakranov, N.; Kudaibergenov, S.; Nuraje, N. A Heterojunction Strategy to Improve the Visible Light Sensitive Water Splitting Performance of Photocatalytic Materials. *J. Mater. Chem. A* **2018**, *6* (44), 21696–21718. https://doi.org/10.1039/C8TA04165B.

(146) Raveendran, A.; Chandran, M.; Dhanusuraman, R. A Comprehensive Review on the Electrochemical Parameters and Recent Material Development of Electrochemical Water Splitting Electrocatalysts. *RSC Adv.* **2023**, *13* (6), 3843–3876. https://doi.org/10.1039/D2RA07642J.

(147) Hisatomi, T.; Yamada, T.; Nishiyama, H.; Takata, T.; Domen, K. Materials and Systems for Large-Scale Photocatalytic Water Splitting. *Nat. Rev. Mater.* **2025**. https://doi.org/10.1038/s41578-025-00823-0.

(148) Tee, S. Y.; Win, K. Y.; Teo, W. S.; Koh, L.; Liu, S.; Teng, C. P.; Han, M. Recent Progress in Energy-Driven Water Splitting. *Adv. Sci.* **2017**, *4* (5), 1600337. https://doi.org/10.1002/advs.201600337.

(149) Jiao, X.; Zheng, K.; Hu, Z.; Sun, Y.; Xie, Y. Broad-Spectral-Response Photocatalysts for CO_2 Reduction. *ACS Cent. Sci.* **2020**, *6* (5), 653–660. https://doi.org/10.1021/acscentsci.0c00325.

(150) Nishioka, S.; Osterloh, F. E.; Wang, X.; Mallouk, T. E.; Maeda, K. Photocatalytic Water Splitting. *Nat. Rev. Methods Primer* **2023**, *3* (1), 42. https://doi.org/10.1038/s43586-023-00226-x.

(151) Etacheri, V.; Di Valentin, C.; Schneider, J.; Bahnemann, D.; Pillai, S. C. Visible-Light Activation of TiO_2 Photocatalysts: Advances in Theory and Experiments. *J. Photochem. Photobiol. C Photochem. Rev.* **2015**, *25*, 1–29. https://doi.org/10.1016/j.jphotochemrev.2015.08.003.

(152) Fujishima, A.; Rao, T. N.; Tryk, D. A. Titanium Dioxide Photocatalysis. *J. Photochem. Photobiol. C Photochem. Rev.* **2000**, *1* (1), 1–21. https://doi.org/10.1016/S1389-5567(00)00002-2.

(153) Wang, P.; Benitez, G.; Houle, F. A. Influence of Hole Transport and Thermal Reactions in Photo-Driven Water Oxidation Kinetics on Crystalline TiO_2. *ACS Catal.* **2025**, *15* (9), 7653–7665. https://doi.org/10.1021/acscatal.5c00945.

(154) Chen, Y.; Soler, L.; Cazorla, C.; Oliveras, J.; Bastús, N. G.; Puntes, V. F.; Llorca, J. Facet-Engineered TiO_2 Drives Photocatalytic Activity and Stability of Supported Noble Metal Clusters during H_2 Evolution. *Nat. Commun.* **2023**, *14* (1), 6165. https://doi.org/10.1038/s41467-023-41976-2.

(155) Harb, M.; Jeantelot, G.; Basset, J.-M. Insights into the Most Suitable TiO_2 Surfaces for Photocatalytic O_2 and H_2 Evolution Reactions from DFT Calculations. *J. Phys. Chem. C* **2019**, *123* (46), 28210–28218. https://doi.org/10.1021/acs.jpcc.9b08145.

(156) Wolkenstein, Th. The Electron Theory of Catalysis on Semiconductors. In *Advances in Catalysis*; Elsevier, 1960; Vol. 12, pp 189–264. https://doi.org/10.1016/S0360-0564(08)60603-3.

(157) Fujishima, A.; Honda, K. Electrochemical Photolysis of Water at a Semiconductor Electrode. *Nature* **1972**, *238* (5358), 37–38. https://doi.org/10.1038/238037a0.

(158) Hanaor, D. A. H.; Sorrell, C. C. Review of the Anatase to Rutile Phase Transformation. *J. Mater. Sci.* **2011**, *46* (4), 855–874. https://doi.org/10.1007/s10853-010-5113-0.

(159) Manzoli, M.; Freyria, F. S.; Blangetti, N.; Bonelli, B. Brookite, a Sometimes under Evaluated TiO_2 Polymorph. *RSC Adv.* **2022**, *12* (6), 3322–3334. https://doi.org/10.1039/D1RA09057G.

(160) Ali, I.; Suhail, M.; Alothman, Z. A.; Alwarthan, A. Recent Advances in Syntheses, Properties and Applications of TiO_2 Nanostructures. *RSC Adv.* **2018**, *8* (53), 30125–30147. https://doi.org/10.1039/C8RA06517A.

(161) Wen, B.; Hao, Q.; Yin, W.-J.; Zhang, L.; Wang, Z.; Wang, T.; Zhou, C.; Selloni, A.; Yang, X.; Liu, L.-M. Electronic Structure and Photoabsorption of Ti^{3+} Ions in Reduced Anatase and Rutile TiO_2. *Phys. Chem. Chem. Phys.* **2018**, *20* (26), 17658–17665. https://doi.org/10.1039/C8CP02648C.

(162) Choi, H.; Khan, S.; Choi, J.; Dinh, D. T. T.; Lee, S. Y.; Paik, U.; Cho, S.-H.; Kim, S. Synergetic Control of Band Gap and Structural Transformation for Optimizing TiO_2 Photocatalysts. *Appl. Catal. B Environ.* **2017**, *210*, 513–521. https://doi.org/10.1016/j.apcatb.2017.04.020.

(163) Choi, H.; Khan, S.; Choi, J.; Dinh, D. T. T.; Lee, S. Y.; Paik, U.; Cho, S.-H.; Kim, S. Synergetic Control of Band Gap and Structural Transformation for Optimizing TiO_2 Photocatalysts. *Appl. Catal. B Environ.* **2017**, *210*, 513–521. https://doi.org/10.1016/j.apcatb.2017.04.020.

(164) Luttrell, T.; Halpegamage, S.; Tao, J.; Kramer, A.; Sutter, E.; Batzill, M. Why Is Anatase a Better Photocatalyst than Rutile? - Model Studies on Epitaxial TiO_2 Films. *Sci. Rep.* **2014**, *4* (1), 4043. https://doi.org/10.1038/srep04043.

(165) Yang, H. G.; Sun, C. H.; Qiao, S. Z.; Zou, J.; Liu, G.; Smith, S. C.; Cheng, H. M.; Lu, G. Q. Anatase TiO_2 Single Crystals with a Large Percentage of Reactive Facets. *Nature* **2008**, *453* (7195), 638–641. https://doi.org/10.1038/nature06964.

(166) Landmann, M.; Rauls, E.; Schmidt, W. G. The Electronic Structure and Optical Response of Rutile, Anatase and Brookite TiO2. *J. Phys. Condens. Matter* **2012**, *24* (19), 195503. https://doi.org/10.1088/0953-8984/24/19/195503.

(167) Kakuma, Y.; Nosaka, A. Y.; Nosaka, Y. Difference in TiO_2 Photocatalytic Mechanism between Rutile and Anatase Studied by the Detection of Active Oxygen and Surface Species in Water. *Phys. Chem. Chem. Phys.* **2015**, *17* (28), 18691–18698. https://doi.org/10.1039/C5CP02004B.

(168) Li, R.; Weng, Y.; Zhou, X.; Wang, X.; Mi, Y.; Chong, R.; Han, H.; Li, C. Achieving Overall Water Splitting Using Titanium Dioxide-Based Photocatalysts of Different Phases. *Energy Environ. Sci.* **2015**, *8* (8), 2377–2382. https://doi.org/10.1039/C5EE01398D.

(169) Zhang, R.; Liu, Z.; Ling, L.; Wang, B. The Effect of Anatase TiO_2 Surface Structure on the Behavior of Ethanol Adsorption and Its Initial Dissociation Step: A DFT Study. *Appl. Surf. Sci.* **2015**, *353*, 150–157. https://doi.org/10.1016/j.apsusc.2015.06.059.

(170) Bouzidi, F.; Tadjine, M.; Berbri, A.; Bouhekka, A. Water Adsorption on Rutile Titanium Dioxide (110): Theoretical Study of the Effect of Surface Oxygen Vacancies and Water Flux in the Steady State Case. *Rev. Mex. Física* **2023**, *69* (3 May-Jun). https://doi.org/10.31349/RevMexFis.69.031004.

(171) Zeng, W.; Liu, T.; Wang, Z.; Tsukimoto, S.; Saito, M.; Ikuhara, Y. Oxygen Adsorption on Anatase TiO_2 (101) and (001) Surfaces from First Principles. *Mater. Trans.* **2010**, *51* (1), 171–175. https://doi.org/10.2320/matertrans.M2009317.

(172) Diebold, U. The Surface Science of Titanium Dioxide. *Surf. Sci. Rep.* **2003**, *48* (5), 53–229. https://doi.org/10.1016/S0167-5729(02)00100-0.

(173) Rozman, N.; Nadrah, P.; Cornut, R.; Jousselme, B.; Bele, M.; Dražić, G.; Gaberšček, M.; Kunej, Š.; Škapin, A. S. TiO_2 Photocatalyst with Single and Dual Noble Metal Co-Catalysts for Efficient Water Splitting and Organic Compound Removal. *Int. J. Hydrog. Energy* **2021**, *46* (65), 32871–32881. https://doi.org/10.1016/j.ijhydene.2021.07.129.

(174) Liu, C.; Wang, F.; Zhang, J.; Wang, K.; Qiu, Y.; Liang, Q.; Chen, Z. Efficient Photoelectrochemical Water Splitting by g-C_3N_4/TiO_2 Nanotube Array Heterostructures. *Nano-Micro Lett.* **2018**, *10* (2), 37. https://doi.org/10.1007/s40820-018-0192-6.

(175) Meng, L.; Yan, L.-K.; Viñes, F.; Illas, F. Effect of Terminations on the Hydrogen Evolution Reaction Mechanism on Ti_3C_2 MXene. *J. Mater. Chem. A* **2023**, *11* (13), 6886–6900. https://doi.org/10.1039/D3TA00261F.

(176) Lasia, A. Mechanism and Kinetics of the Hydrogen Evolution Reaction. *Int. J. Hydrog. Energy* **2019**, *44* (36), 19484–19518. https://doi.org/10.1016/j.ijhydene.2019.05.183.

(177) Hejazi, S.; Mohajernia, S.; Osuagwu, B.; Zoppellaro, G.; Andryskova, P.; Tomanec, O.; Kment, S.; Zbořil, R.; Schmuki, P. On the Controlled Loading of Single Platinum Atoms as a Co-Catalyst on TiO_2 Anatase for Optimized Photocatalytic H_2 Generation. *Adv. Mater.* **2020**, *32* (16), 1908505. https://doi.org/10.1002/adma.201908505.

(178) Zang, W.; Lee, J.; Tieu, P.; Yan, X.; Graham, G. W.; Tran, I. C.; Wang, P.; Christopher, P.; Pan, X. Distribution of Pt Single Atom Coordination Environments on Anatase TiO_2 Supports Controls Reactivity. *Nat. Commun.* **2024**, *15* (1), 998. https://doi.org/10.1038/s41467-024-45367-z.

(179) Puntscher, L.; Daninger, K.; Schmid, M.; Diebold, U.; Parkinson, G. S. A Study of Pt, Rh, Ni and Ir Dispersion on Anatase TiO_2 (101) and the Role of Water. *Electrochimica Acta* **2023**, *449*, 142190. https://doi.org/10.1016/j.electacta.2023.142190.

(180) Arroyo-de Dompablo, M. E.; Morales-García, A.; Taravillo, M. DFT+U Calculations of Crystal Lattice, Electronic Structure, and Phase Stability under Pressure of TiO_2 Polymorphs. *J. Chem. Phys.* **2011**, *135* (5), 054503. https://doi.org/10.1063/1.3617244.

(181) Mathur, S.; Kuhn, P. CVD of Titanium Oxide Coatings: Comparative Evaluation of Thermal and Plasma Assisted Processes. *Surf. Coat. Technol.* **2006**, *201* (3), 807–814. https://doi.org/10.1016/j.surfcoat.2005.12.039.

(182) Sun, L.; Yuan, G.; Gao, L.; Yang, J.; Chhowalla, M.; Gharahcheshmeh, M. H.; Gleason, K. K.; Choi, Y. S.; Hong, B. H.; Liu, Z. Chemical Vapour Deposition. *Nat. Rev. Methods Primer* **2021**, *1* (1), 5. https://doi.org/10.1038/s43586-020-00005-y.

(183) Mathur, S.; Barth, S. Molecule-Based Chemical Vapor Growth of Aligned SnO_2 Nanowires and Branched SnO_2/V_2O_5 Heterostructures. *Small* **2007**, *3* (12), 2070–2075. https://doi.org/10.1002/smll.200700213.

(184) Mathur, S.; Barth, S.; Werner, U.; Hernandez-Ramirez, F.; Romano-Rodriguez, A. Chemical Vapor Growth of One-Dimensional Magnetite Nanostructures. *Adv. Mater.* **2008**, *20* (8), 1550–1554. https://doi.org/10.1002/adma.200701448.

(185) Schläfer, J.; Graf, D.; Fornalczyk, G.; Mettenbörger, A.; Mathur, S. Fluorinated Cerium(IV) Enaminolates: Alternative Precursors for Chemical Vapor Deposition of CeO_2 Thin Films. *Inorg. Chem.* **2016**, *55* (11), 5422–5429. https://doi.org/10.1021/acs.inorgchem.6b00348.

(186) Straub, M. D.; Leduc, J.; Frank, M.; Raauf, A.; Lohrey, T. D.; Minasian, S. G.; Mathur, S.; Arnold, J. Chemical Vapor Deposition of Phase-Pure Uranium Dioxide Thin Films from Uranium(IV) Amidate Precursors. *Angew. Chem. Int. Ed.* **2019**, *58* (17), 5749–5753. https://doi.org/10.1002/anie.201901924.

(187) Lichtenberg, A.; Altuntas, K.; Fischer, T.; Karimpour, T.; Diel, S.; Aytuna, Z.; Amadi, C. K.; Mathur, S. Molecular Transformations for Direct Synthesis of Thorium Dioxide Films. *Z. Für Anorg. Allg. Chem.* **2024**, *650* (23), e202400126. https://doi.org/10.1002/zaac.202400126.

(188) Mathur, S.; Kuhn, P. CVD of Titanium Oxide Coatings: Comparative Evaluation of Thermal and Plasma Assisted Processes. *Surf. Coat. Technol.* **2006**, *201* (3), 807–814. https://doi.org/10.1016/j.surfcoat.2005.12.039.

(189) Martsinovich, N.; Troisi, A. How TiO_2 Crystallographic Surfaces Influence Charge Injection Rates from a Chemisorbed Dye Sensitiser. *Phys. Chem. Chem. Phys.* **2012**, *14* (38), 13392–13401. https://doi.org/10.1039/C2CP42055D.

(190) Liu, M.; Piao, L.; Zhao, L.; Ju, S.; Yan, Z.; He, T.; Zhou, C.; Wang, W. Anatase TiO_2 Single Crystals with Exposed {001} and {110} Facets: Facile Synthesis and Enhanced Photocatalysis. *Chem. Commun.* **2010**, *46* (10), 1664–1666. https://doi.org/10.1039/B924172H.

(191) Brune, H.; Bales, G. S.; Jacobsen, J.; Boragno, C.; Kern, K. Measuring Surface Diffusion from Nucleation Island Densities. *Phys. Rev. B* **1999**, *60* (8), 5991–6006. https://doi.org/10.1103/PhysRevB.60.5991.

(192) Mohamed, S. K.; Bashat, A. M. A.; Hassan, H. M. A.; Ismail, N.; El Rouby, W. M. A. Optimizing the Performance of $Au_y/Ni_x/TiO_2$ NTs Photoanodes for

Photoelectrochemical Water Splitting. *RSC Adv.* **2023**, *13* (20), 14018–14032. https://doi.org/10.1039/D3RA02011H.

(193) Hou, X.; Li, Z.; Fan, L.; Yuan, J.; Lund, P. D.; Li, Y. Effect of Ti Foil Size on the Micro Sizes of Anodic TiO_2 Nanotube Array and Photoelectrochemical Water Splitting Performance. *Chem. Eng. J.* **2021**, *425*, 131415. https://doi.org/10.1016/j.cej.2021.131415.

(194) Gong, M.; Dai, H. A Mini Review of NiFe-Based Materials as Highly Active Oxygen Evolution Reaction Electrocatalysts. *Nano Res.* **2015**, *8* (1), 23–39. https://doi.org/10.1007/s12274-014-0591-z.

(195) Singh, A. K.; Ji, S.; Singh, B.; Das, C.; Choi, H.; Menezes, P. W.; Indra, A. Alkaline Oxygen Evolution: Exploring Synergy between Fcc and Hcp Cobalt Nanoparticles Entrapped in N-Doped Graphene. *Mater. Today Chem.* **2022**, *23*, 100668. https://doi.org/10.1016/j.mtchem.2021.100668.

(196) Singh, S. P.; Surya, R. M.; Matsushima, K.; Beppu, K.; Amano, F. Pelletized TiO_2 : Effect of Grain Size and Electrical Conductivity on Photoelectrochemical Water Splitting. *J. Phys. Chem. C* **2025**, acs.jpcc.5c04261. https://doi.org/10.1021/acs.jpcc.5c04261.

(197) Zhao, H.; Pan, F.; Li, Y. A Review on the Effects of TiO2 Surface Point Defects on CO_2 Photoreduction with H_2O. *J. Materiomics* **2017**, *3* (1), 17–32. https://doi.org/10.1016/j.jmat.2016.12.001.

(198) Ren, L.; Ma, S.; Shi, Y.; Zhao, C.; Wang, X.; Gao, Z.; Xie, H. Insights into the Pivotal Role of Surface Defects on Anatase TiO_2 Nanosheets with Exposed {001} Facets for Enhanced Photocatalytic Activity. *Mater. Res. Bull.* **2023**, *164*, 112255. https://doi.org/10.1016/j.materresbull.2023.112255.

(199) Long, Z.; Meng, J.; Weddle, L. R.; Videla, P. E.; Menzel, J. P.; Cabral, D. G. A.; Liu, J.; Qiu, T.; Palasz, J. M.; Bhattacharyya, D.; Kubiak, C. P.; Batista, V. S.; Lian, T. The Impact of Electric Fields on Processes at Electrode Interfaces. *Chem. Rev.* **2025**, *125* (3), 1604–1628. https://doi.org/10.1021/acs.chemrev.4c00487.

(200) Kim, S.; Ji, S.; Jeong, S.; Yang, H.; Lee, S.; Choi, H.; Li, O. L. Switching Electric Double Layer Potential by Phase Structure Control for Advanced Oxygen Reduction Reaction of Cobalt@Nitrogen Doped Carbon Core–Shell. *Small* **2024**, *20* (16), 2307483. https://doi.org/10.1002/smll.202307483.

(201) Kim, S.; Ji, S.; Yang, H.; Son, H.; Choi, H.; Kang, J.; Li, O. L. Near Surface Electric Field Enhancement: Pyridinic-N Rich Few-Layer Graphene Encapsulating Cobalt

Catalysts as Highly Active and Stable Bifunctional ORR/OER Catalyst for Seawater Batteries. *Appl. Catal. B Environ.* **2022**, *310*, 121361. https://doi.org/10.1016/j.apcatb.2022.121361.

(202) Kwon, J.; Choi, H.; Choi, S.; Sun, J.; Han, H.; Paik, U.; Choi, J.; Song, T. Improved Charge Carrier Dynamics by Unconventional Doping Strategy for $BiVO_4$ Photoanode. *Small Sci.* **2025**, *5* (7), 2500051. https://doi.org/10.1002/smsc.202500051.

Teilpublikationen:

1. Seulgi Ji, Dong Won Jeon, Junghyun Choi, Haneol Cho, Bo-In, Park, Ilpyo Roh, Hyungil Choi, Chansoo Kim, Jung Kyu Kim, Uk Sim, Danlei Li, Hyunseok Ko*, Sung Beom Cho*, Heechae Choi*, *"Overcoming the Limitation of Atomic-scale Simulations on Semiconductor-Catalysis with Changing Fermi Level and Surface Treatment"*, Journal of Materials Chemistry A, 2024, 12, 33537-33545